# Exploring Quantum Phenomena in 2D Materials: From Valley Topology and Exciton Selection Rules to Tuning Magnetic Correlations

Tharindu Fernando

A dissertation
submitted in partial fulfillment of the
requirements for the degree of

Doctor of Philosophy

University of Washington

2025

Reading Committee:

Ting Cao, Chair

Di Xiao

Marcel den Nijs

Program Authorized to Offer Degree:
Physics

University of Washington

**Abstract**

Exploring Quantum Phenomena in 2D Materials: From Valley Topology and Exciton Selection Rules to Tuning Magnetic Correlations

Tharindu Fernando

Chair of the Supervisory Committee:
Ting Cao
Department of Materials Science & Engineering

This thesis presents two independent parts under the common theme of quantum phenomena in 2D materials: **Part I** introduces a gauge-invariant, quantized interband index for multiband 2D systems and uses it in two applications: **A)** to analyze valley topology, and **B)** to derive gauge-invariant exciton selection rules. **Part II** investigates monolayer $Nb_3Cl_8$, quantifies magnetic anisotropy, and shows that biaxial strain tunes antiferromagnetic, paramagnetic, and ferromagnetic behavior.

**Part I, Application A: Interband index and valley topology.** We introduce a novel gauge-invariant, quantized interband index in two-dimensional (2D) multiband systems. It provides a bulk topological classification of a submanifold of parameter space (e.g., an electron valley in a Brillouin zone), and therefore overcomes difficulties in characterizing topology of submanifolds. We confirm its topological nature by numerically demonstrating a one-to-one correspondence to the valley Chern number in $k \cdot p$ models (e.g., gapped Dirac fermion model), and the first Chern number in lattice models (e.g., Haldane model). Furthermore, we derive a band-resolved topological charge and demonstrate that it can be used to investigate the nature of edge states due to band inversion in valley systems like multilayer graphene.

**Part I, Application B: Gauge-invariant optical selection rules for excitons.** Excitons are central to the photophysics of 2D semiconductors and photonic devices. Prior circular selection rules for excitons in 2D are successful but gauge-dependent due to assumptions that exclude singular gauge behavior at band edges. By developing a chiral form of the interband index from

Application A above, we obtain selection rules that are manifestly gauge-invariant. This framework is directly compatible with numerical workflows used in device modeling, and strengthens the theory of quantum materials, especially two-dimensional semiconductor photophysics.

**Part II. Strain-tunable magnetism in $Nb_3Cl_8$.** Recent research suggests the possibility of the two-dimensional breathing-Kagome magnet $Nb_3Cl_8$ hosting a quantum spin liquid state, warranting further study into its magnetic properties. Using *ab initio* calculations, we show that monolayer $Nb_3Cl_8$ has short-range antiferromagnetic correlations among $Nb_3$ trimers with $S = 1/2$, and becomes magnetically frustrated due to the underlying effective triangular lattice geometry, and is evidenced by a frustration index of $f > 1$. The high-temperature susceptibility shows a negative Weiss temperature from Monte Carlo calculations. Considering spin-orbit coupling, we investigate the magnetic anisotropy, including anisotropic exchange, single-ion anisotropy and the Dzyaloshinskii–Moriya interaction using the four-state energy mapping formalism. Although the elements have relatively small atomic numbers, the Dzyaloshinskii–Moriya interaction is comparable in magnitude to the anisotropic exchange. Additionally, we show that biaxial strain tunes the short-range correlations between antiferromagnetic, paramagnetic and ferromagnetic. These findings strengthen our understanding of $Nb_3Cl_8$ and advance its applications in current condensed matter physics and materials science research, including nanoscale mechanical and spintronics applications.

**Summary.** Part I supplies a valley-focused topological index and a gauge-invariant theory of exciton selection rules. Part II elucidates the magnetic anisotropy and tunability of magnetism in monolayer $Nb_3Cl_8$. Collectively, these findings fulfill the thesis aim of exploring quantum phenomena in 2D materials.

## TABLE OF CONTENTS

## LIST OF FIGURES

Figure Number Page

## LIST OF TABLES

## ACKNOWLEDGMENTS

This dissertation exists because many people shared their time, patience, and care. I am deeply grateful to everyone who helped me make this PhD a reality, in academia and beyond it.

First, my sincere thanks to Dr. Cao for extraordinary mentorship. He made time for me, looked out for me, and guided me with humility and patience. Much of my growth as a researcher comes from his example and encouragement. I am also thankful to Drs. Xiaowei Zhang and Kaichen Xie for technical guidance over the years, and to Drs. Di Xiao, Yafei Ren, and Chong Wang for insightful discussions. I appreciate the companionship of the Quantum Theory Group, especially Shivesh Sivakumar, Jimin Qian, Lingnan Shen, Yusen Ye, Wenqin Chen, and Yueyao Fan. From my time at UC San Diego, I owe thanks to Drs. Congjun Wu, Yi-Zhuang You, and Chao Xu, who set me on this path in condensed matter. Special thanks has to be given to my collaborators from other research groups, including Sabin Regmi, Dylan Jeff, and Drs. Yuzhou Zhao, Saiful Khondaker, Xiaodong Xu, and Madhab Neupane.

I am grateful to my PhD committee for their involvement: Drs. Cao, Di Xiao, Marcel den Nijs, Mark Rudner, David Cobden, and M. P. Anantram. I also thank Catherine Provost for helping me settle into the department and for support along the way.

My work outside research mattered to me, and many people made it possible. For outreach, thank you to Steve Sharpe, Danica Hendricson, Xiaosong Li, and Nikolai Tolich. You helped me become a more effective leader in the department and through STEM Pals. I am also grateful to everyone I served with on departmental committees, including the Climate and Diversity Committee, the Colloquium Committee, the Physics Graduate Student Committee, the DEI working group, Undergraduate Women+ in Physics, and the Undergraduate Mentoring program.

To the STEM Pals team, thank you. When I founded STEM Pals I did not anticipate how passionately the UW community would embrace it. So many people poured in energy to build something lasting. Sam Tetef, your work was instrumental in laying the foundation. I am also

grateful to Al Snow, Ariana Frey, Ian Campbell, and Dr. Nicole Gregorio for keeping the program strong after I stepped back.

To everyone I have not named here, please accept my heartfelt thanks; your guidance, encouragement, and everyday kindness sustained me and shaped this work.

To my friends at UW who kept me grounded and laughing: Jessica Birky, Sam Tetef, Robert Pecoraro, Maleen Wijeratna, David Sharp, Abdul Moeez, Will Marshall, and Chaman Gupta, thank you for your support and company. Love also to Laura, Alora, Monique, Ashok, Ellie, and Kurt, and Josh, and to Yamen, Ben, Gavin, Akshit, Vitaly, and Sirish. A special thank you to Kim for being there during a very hard time.

I am extremely fortunate to have a loving family. I am grateful to my cousins Randika and Sahan, to Neelaka mama, Nonamma, Pappa, and Achchiamma, and to all my cousins, aunties, and uncles. To my partner, Jada, thank you for your care and strength through every rough stretch. Finally, to my parents, Felix and Manjula, and to my sister and best friend, Veena (a.k.a. Beet, Nanga), I owe more than I can say. These years were not easy, and I would not have reached this day without you.

## DEDICATION

To my dear family: Dady, Mama, and Nanga,
who held me steady when the night was heavy
and stayed until the sun rose again.
Every. Single. Time.

Part I

# APPLICATIONS OF NOVEL QUANTIZED INTERBAND TOPOLOGICAL INDEX IN 2-DIMENSIONAL QUANTUM SYSTEMS

Chapter 1

# BACKGROUND AND MOTIVATION

In the first part of this dissertation, we explore the gauge-invariant quantized topological index for submanifolds in 2-dimensional quantum systems that was introduced in Ref. [173, 180]. Consequences of this index in quantum physics were not apparent at first glance. So, following theoretical and computational investigations carried out over several years, we found two new applications of this index: one in valley topology (Chapter 2), and the other in optical selection rules for excitons (Chapter 3). In this chapter, we present background concepts to set the stage for discussions on our findings.

This work began during my undergraduate years at UC San Diego under the guidance of Chao Xu and Professor Congjun Wu, before I started my graduate studies at the University of Washington under Professor Ting Cao. I am grateful for all of them for their patience and guidance, and also thank Professors Yi-Zhuang You, Yafei Ren and Di Xiao for helpful discussions.

## *1.1 Geometry and Topology in Condensed Matter in 2-Dimensional Systems*

In this section, we present a concise, high-level overview of basic concepts in condensed matter theory that are most relevant for our work on the novel interband index. We highlight the adiabatic theorem, Bloch bands, Berry phase and curvature, and connection to topological invariants. These concepts form the foundation needed to introduce and motivate the interband index developed in sections that follow. This is not intended to be a comprehensive review, as there's a substantial amount of literature covering these topics (e.g., Ref. [43, 176]).

### *1.1.1 Adiabatic Theorem and Time-Independent Schrodinger Equation*

A physical system may be modeled by a Hamiltonian $H$ that is dependent on time via parameters $\mathbf{R} = \mathbf{R}(t) = (R_1, R_2, ...) \equiv R_\mu$:

$$H = H(\mathbf{R}). \tag{1.1}$$

In condensed matter systems, external perturbations typically vary much more slowly than electronic timescales. So, we consider the system's adiabatic evolution, where $\mathbf{R}(t)$ traverses slowly in the parameter space $\mathcal{M}$ along a path $\partial\mathcal{M}$. The quantum adiabatic theorem [73, 119] states that a system starting in an eigenstate $|m(\mathbf{R}(0))\rangle$ will remain an instantaneous eigenstate of $H(\mathbf{R}(t))$ throughout an adiabatic evolution, up to an arbitrary $\mathbf{R}$-dependent phase factor (or *gauge*) of $|m(\mathbf{R})\rangle$. This gauge has to be smooth and single-valued along $\partial\mathcal{M}$, but could be chosen in a way to overcome the arbitrariness. This situation can be modeled by the time-independent Schrödinger equation, which could be represented using an instantaneous orthonormal basis of the eigenvectors of $H(\mathbf{R})$:

$$H(\mathbf{R})\,|m(\mathbf{R})\rangle = E_m(\mathbf{R})\,|m(\mathbf{R})\rangle\,. \tag{1.2}$$

Solving the above eigenvalue equation at each value of $\mathbf{R}$ yields the instantaneous eigenstates $|m(\mathbf{R})\rangle$ and instantaneous energy eigenvalues $E_m(\mathbf{R})$.

When studying crystals, it is beneficial to Fourier transform real-space coordinates $\mathbf{r}$ to reciprocal (momentum) $\mathbf{k}$ coordinates. By Bloch's theorem, the instantaneous eigenstate $|m(\mathbf{R})\rangle$ (where $\mathbf{R}$ is the arbitrary parameter) satisfies

$$\langle \mathbf{r} \mid m(\mathbf{R})\rangle \;=\; e^{\,i\,\mathbf{R}\cdot\mathbf{r}}\; u_m\big(\mathbf{r};\mathbf{R}\big), \tag{1.3}$$

where we have periodicity $u_m(\mathbf{r}+\mathbf{r}_\ell;\mathbf{R}) = u_m(\mathbf{r};\mathbf{R})$ for any lattice vector $\mathbf{r}_\ell$. If we choose $\mathbf{k}$-space as the parameter space $\mathbf{R} \equiv \mathbf{k} = (k_x, k_y, k_z)$, then

$$\langle \mathbf{r} \mid m(\mathbf{k})\rangle \;=\; e^{\,i\,\mathbf{k}\cdot\mathbf{r}}\; u_m\big(\mathbf{r};\mathbf{k}\big) \quad\Longleftrightarrow\quad |m(\mathbf{k})\rangle \;=\; e^{\,i\,\mathbf{k}\cdot\mathbf{r}}\; |u_m(\mathbf{k})\rangle\,, \tag{1.4}$$

with $\mathbf{k}$ restricted to the Brillouin zone (a region of $\mathbf{k}$-space with periodic boundaries). If we have a non-degenerate $N$-level system, we may determine an $N \times N$ Hamiltonian matrix $H(\mathbf{k})$ using the

time-independent Schrödinger equation

$$H(\mathbf{k})\ |m(\mathbf{k})\rangle\ =\ E_m(\mathbf{k})\ |m(\mathbf{k})\rangle\,, \quad (m = 1, 2, ..., N) \tag{1.5}$$

to calculate $E_m(\mathbf{k})$ and $|m(\mathbf{k})\rangle$. When $E_m(\mathbf{k})$ is plotted over the Brillouin zone as a band diagram, the electronic structure of the solid is revealed. Band diagrams help determine a solid's electronic phase (e.g., metallic, semiconducting, or insulating) by revealing gap sizes, dispersions, and band connectivity that signal phase transitions through gap closings or band reorderings, while also underpinning optical transitions, transport properties, and topological phenomena. Since this work focuses on 2-dimensional crystals, we work with $\mathbf{R} \equiv \mathbf{k} = (k_x, k_y)$ parameters going forward. For generality, we also relabel time $t$ with parameter $\lambda$, which allows $\mathbf{k}$ to be parameterized as $\mathbf{k} = (k_x(\lambda), k_y(\lambda)) \equiv k_\mu$.

Following from Eq. (1.2), the quantum state at a time $\lambda$ is:

$$|\psi_m(\lambda)\rangle = \exp^{i\gamma_m(\lambda)} \exp\Big[-\tfrac{i}{\hbar}\int_0^\lambda d\lambda'\, E_m\big(\mathbf{k}(\lambda')\big)\Big]\ |m\big(\mathbf{k}(\lambda)\big)\rangle\,. \tag{1.6}$$

Above, the second exponential is the dynamical phase factor determined completely by $E_m(\mathbf{k})$, and $\gamma_m(\lambda)$ is a so-called *geometric phase*, since it depends on the path taken through parameter space.

### *1.1.2 Berry Phase*

When Eq. (1.6) is inserted into the time-dependent Schrödinger equation

$$i\hbar\frac{\partial}{\partial\lambda}\,|\psi_m(\lambda)\rangle\ =\ H\big(\mathbf{k}(\lambda)\big)\ |\psi_m(\lambda)\rangle \tag{1.7}$$

and the product with $\langle m(\mathbf{k}(\lambda))|$ is taken from the left, we can express the geometric phase $\gamma_m$ appearing in Eq. (1.6) as:

$$\gamma_m(\mathbf{k})\ =\ \int_{\partial\mathcal{M}} \mathcal{A}_m^\mu(\mathbf{k})\,\mathrm{d}\lambda_\mu, \tag{1.8}$$

where the *Berry connection* $\mathcal{A}_m(\mathbf{k})$ is

$$\mathcal{A}_m^\mu(\mathbf{k}) = i\,\langle m(\mathbf{k})|\frac{\partial}{\partial\lambda_\mu} m(\mathbf{k})\rangle \tag{1.9}$$

It should be noted that $\mathcal{A}_m^\mu(\mathbf{k})$ is a gauge-dependent quantity, since a gauge transformation with an arbitrary single-valued smooth function $\theta(\mathbf{k})$

$$|m(\mathbf{k})\rangle \;\longrightarrow\; e^{\,i\theta(\mathbf{k})}\;|m(\mathbf{k})\rangle \tag{1.10}$$

will lead to the transformation

$$A_m^\mu(\mathbf{k}) \;\longrightarrow\; A_m^\mu(\mathbf{k}) \;-\; \frac{\partial}{\partial \mathbf{k}}\,\theta(\mathbf{k}). \tag{1.11}$$

It was originally believed that one could always choose $\theta(\mathbf{k})$ such that $\gamma_m = 0$, leaving only the dynamical phase to contribute to the overall phase. However, Berry considered the case of a closed path $\partial\mathcal{M}$, with the initial and final points being the same: $\mathbf{k}(0) = \mathbf{k}(T)$ [7]. Since $\theta(\mathbf{k})$ has to be single-valued,

$$\theta(\mathbf{k}(0)) - \theta(\mathbf{k}(T)) = 2\pi \times \text{integer}. \tag{1.12}$$

Therefore, $\gamma_m$ cannot be removed, and can only change by an integer multiple of $2\pi$ under gauge transformations. This makes $\gamma_m$ a U(1) gauge-invariant, and therefore a physically observable, quantity, and is called the *Berry phase* $\gamma_m^B$:

$$\gamma_m^B(\mathbf{k}) \;=\; \oint_{\partial\mathcal{M}} \mathcal{A}_m^\mu(\mathbf{k})\,\mathrm{d}\lambda_\mu, \tag{1.13}$$

The discovery of the Berry phase revealed that quantum states acquire a path-dependent phase determined solely by the geometry of parameter space. This opened up the the field of topological physics and inspired work that led to the Nobel prize in 2016.

### *1.1.3 Stokes' Theorem and Berry Curvature*

Because the Berry phase is a line integral over a closed curve, Stokes' theorem lets us write it as a surface integral of a 2-form (using language from differential geometry). In this notation, the Berry connection 1-form $\omega$ is

$$\omega = \mathcal{A}_m \;=\; \mathcal{A}_m^\mu(\mathbf{k})\,\mathrm{d}\lambda_\mu, \tag{1.14}$$

and its exterior derivative defines the Berry curvature 2-form $\mathrm{d}\omega$:

$$\mathrm{d}\omega = \mathcal{F}_m \;=\; \mathrm{d}\mathcal{A}_m \;=\; \frac{1}{2}\, F_m^{\mu\nu}(\mathbf{k})\, \mathrm{d}\lambda_\mu \wedge \mathrm{d}\lambda_\nu, \quad \text{where} \quad F_m^{\mu\nu}(\mathbf{k}) \;=\; \frac{\partial}{\partial \lambda_\mu}\mathcal{A}_m^\nu \;-\; \frac{\partial}{\partial \lambda_\nu}\mathcal{A}_m^\mu. \tag{1.15}$$

Above, $F_m^{\mu\nu}(\mathbf{k})$ is the *Berry curvature*, and $d\lambda_\mu \wedge d\lambda_\nu$ denotes the antisymmetric wedge product, satisfying $d\lambda_\mu \wedge d\lambda_\nu = -\, d\lambda_\nu \wedge d\lambda_\mu$. Finally, Stokes' theorem gives

$$\gamma_m \;=\; \int_{\partial\mathcal{M}} \mathcal{A}_m^\mu \, \mathrm{d}\lambda_\mu = \iint_{\mathcal{M}} F_m^{\mu\nu} \, \mathrm{d}\lambda_\mu \, \mathrm{d}\lambda_\nu. \tag{1.16}$$

Note that Stokes' theorem applies when the parameter space manifold is smooth and oriented with a well-defined, piecewise-smooth boundary, and the differential form being integrated is smooth (i.e., no singularities, which are points where the derivative of $\mathcal{A}_m$ fails to exist) throughout the region and its closure. If singularities do exist, the number of singularities $\Phi_m$ (i.e., the quantized 'amount' by which Stokes' theorem fails) is given by:

$$\Phi_m = \int_{\partial\mathcal{M}} \mathcal{A}_m^\mu \, \mathrm{d}\lambda_\mu - \iint_{\mathcal{M}} F_m \, \mathrm{d}\lambda_\mu \, \mathrm{d}\lambda_\nu. \tag{1.17}$$

$\Phi_m$ could be interpreted as the signed number of Dirac strings in a condensed matter context. In this work, we refer to $\Phi_m$ as *Berry singularities*, and it will be used subsequently in the definition of the novel interband index in Eq. (1.33). Note that $\Phi_m$ can be positive, negative, or 0 depending on the values of the integrals.

A brief discussion of the Berry curvature is in order. For completeness, we note that we could use the Hellmann–Feynman-like expression

$$\left\langle m \left| \frac{\partial H}{\partial \mathbf{k}} \right| n \right\rangle = (E_m - E_n) \left\langle \frac{\partial m}{\partial \mathbf{k}} \middle| n \right\rangle, \text{ for } m \neq n. \tag{1.18}$$

to rewrite the Berry curvature as:

$$F_m^{\mu\nu}(\mathbf{k}) = i \sum_{m \neq n} \frac{\langle m|\partial H/\partial k^\mu|n\rangle\langle n|\partial H/\partial k^\nu|m\rangle - (\nu \leftrightarrow \mu)}{(E_m - E_n)^2}. \tag{1.19}$$

The expression Eq. (1.19) is beneficial because it can be calculated for any gauge, since it does not require taking derivatives of wave functions. This is important because the wavefunction phase is not guaranteed to be smooth in standard numerical diagonalization algorithms.

The Berry curvature also has a sum rule, which states that the total Berry curvature of all levels of the system vanishes:

$$\sum_m F_m^{\mu\nu}(\mathbf{k}) = 0. \tag{1.20}$$

The Berry phase has important consequences in condensed matter physics, of which topology is an important example.

### *1.1.4 Topology and First Chern number*

In two dimensions, due to the periodicity in both directions $k_x$ and $k_y$, the Brillouin zone (BZ) is topologically a torus $T^2$. Therefore, using language from differential geometry, the collection of eigenstates $|m(\mathbf{k})\rangle$ form a U(1) line bundle over $T^2$. Analogous to how the *Gaussian curvature* $K$ characterizes the geometry of a 2-dimensional surface, the Berry curvature characterizes this line bundle (for each point in parameter space of a quantum system, we have an associated Hilbert space, i.e., the line bundle). In other words, one can define a topological invariant by integrating curvature over the base manifold. Such a topological invariant remains unchanged under any smooth deformation of the bundle that does not involve eigenvalue degeneracies, thereby distinguishing inequivalent global properties. Just as the Gauss-Bonnet theorem on a closed 2-dimensional manifold $\mathcal{M}$ relates the topological Euler characteristic index $\chi(\mathcal{M})$ to the area integral (with area element $\mathrm{d}A$) of Gaussian curvature

$$\chi(\mathcal{M}) \;=\; \frac{1}{2\pi}\iint_{\mathcal{M}} K\,\mathrm{d}A, \tag{1.21}$$

the *first Chern number* of band $m$ is defined as:

$$C_m \;=\; \frac{1}{2\pi}\iint_{\mathbf{k}\in\mathrm{BZ}} F_m^{\mu\nu}(\mathbf{k})\,\mathrm{d}\lambda_\mu\,\mathrm{d}\lambda_\nu, \tag{1.22}$$

where the integration of the Berry curvature $F_m^{\mu\nu}(\mathbf{k})$ is over the entire Brillouin zone. Remarkably, $C_m$ is generally an integer. Because $T^2$ is not simply connected, nonzero $C_m$ implies there is no way to choose a single, smooth gauge for $|m(\mathbf{k})\rangle$ globally on the torus. Instead, we cover the Brillouin

zone by overlapping patches that each allow a smooth local gauge. The overlaps of the patches differ by a phase $e^{i\theta(\mathbf{k})}$ as in Eq. (1.10), and the winding of these phases around noncontractible loops in the manifold accounts for the integer flux $2\pi C_m$.

Notice in Eq. (1.19) that $F_m^{\mu\nu}(\mathbf{k})$ becomes singular if $E_m = E_n$ at any $\mathbf{k}$. Such points in parameter space correspond to monopoles of Berry curvature. Integrating $F_m^{\mu\nu}(\mathbf{k})$ over a small region around these monopoles yields a quantized flux that contributes to $C_m$. Therefore, nonzero $C_m$ indicates a global obstruction in the eigenstate bundle. Following from the Berry curvature sum rule Eq. (1.20), $\sum_m C_m = 0$. But when the occupied bands carry net Chern number $C = \sum_{m\in\text{occupied}} C_m \neq 0$, the crystal is a Chern insulator.

Since $C$ is a topological invariant, it is does not change under any smooth deformation of the Hamiltonian that does not close its gap (i.e., when the eigenvalues remain nondegenerate). Indeed, the phase classification here is beyond that from symmetry or local order parameters. $C$ cannot be changed by small impurities, lattice distortions, or other interactions that do not close the energy gap. This makes the phase resistant to many types of disorder. In practice, this robustness forms the foundation of topologically protected edge states that appear at the Chern insulator boundary. Even if the sample has defects or rough edges, these one-way conducting channels remain gapless and immune to backscattering. Another manifestation of $C$ is in the quantized Hall conductivity $\sigma_{xy} = (e^2/h)C$: imperfections in the crystal do not spoil the exact integer value of $\sigma_{xy}$. In the integer quantum Hall effect, $C$ is the number of filled Landau levels. In the quantum Hall literature $C$ is known as the TKNN invariant [164, 165]. Beyond the quantum (anomalous) Hall effect, similar topological arguments explain protected surface states in 3-dimensional topological insulators, chiral edge modes in Chern-simulating photonic crystals, and even unidirectional magnon transport in magnetic skyrmion lattices. In each case, the first Chern number (or its higher-dimensional analogues) guarantees that certain physical observables remain quantized and that boundary modes cannot be moved unless the bulk gap closes. This ensures stability against real-world imperfections.

### 1.1.5 *The Haldane Model for the Quantum Anomalous Hall Effect*

To illustrate the first Chern number $C$ using a concrete example, we look at the Haldane model for the quantum anomalous Hall effect [56]. Using this model, Haldane showed how one could realize a nonzero first Chern number (and hence a Hall conductance) on a lattice without any net magnetic field. The model, presented in Section 4.2.1, can give topologically nontrivial first Chern numbers that may yield topologically-protected edge states [56]. The Chern number changes when the band gap closes and reopens at the high-symmetry points ($K$ or $K'$), as shown in Fig. 1.1. The physics at these high-symmetry valleys is therefore significant, because their gap closings can change the topology, and therefore edge state physics. This observation is important and will be used in subsequent discussions of the interband index.

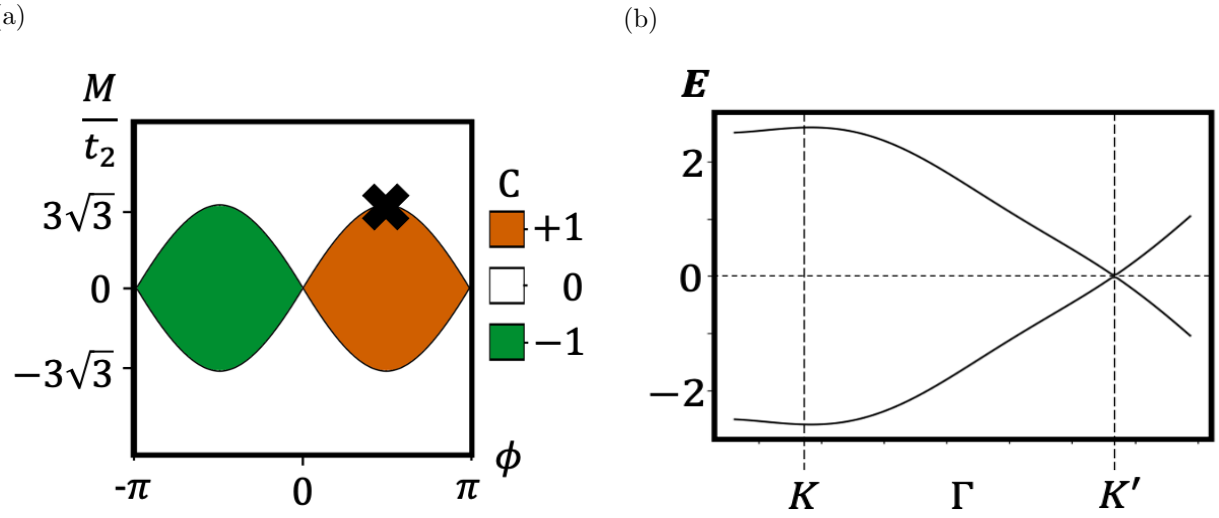


Figure 1.1: (a) A phase diagram of the first Chern number $C$ for the Haldane model as a function of $(M, \phi)$. The topological phase transitions occur by gap closures at K or K'. (b) Conduction and valence bands of the Haldane model for $M/t_2 = 3\sqrt{3}$, $\phi = \pi/2$, and $t_1 = 4t_2 = 1$. The gap closure at K' corresponds to the phase boundary marked with a cross $\times$ in (a).

## *1.2 Novel Quantized Interband Index*

With the context provided in the previous section, we are now ready to introduce the interlevel index introduced in Ref. [173,180] that makes the focus of the first part of this dissertation. We first introduce the quantum geometric potential from Ref. [173], then the novel gauge-invariant quantum interlevel index from Ref. [180], with insight from a differential geometric perspective. We then use the interlevel index Eq. (1.29) to derive a new interband index Eq. (1.33) which allows for direct application in condensed matter momentum $\boldsymbol{k}$-space. We also define a new *interband frequency* Eq. (1.34) which provides insight into the behavior of the interband index before presenting intuition from a Hilbert space standpoint. We then share some observations from preliminary investigations of the interband index, which motivate the application of the index in valley systems in the following chapter.

### *1.2.1 Quantum Geometric Potential and Quantum Adiabatic Condition*

A key ingredient for the novel interband index studied in this work is the *quantum geometric potential* $\Delta_{mn}$ that was introduced in Ref. [173]. For this setup, as we did in the previous section in Eqs. (1.1)-(1.17), we consider an $N$-level Hamiltonian $H(\lambda(t))$ controlled by real vector $\lambda = (\lambda_1(t), \lambda_2(t), ..., \lambda_l(t))$ of length $l$ as a function of time $t$. At each $t$, we have instantaneous orthogonal eigenstates $|m(\lambda)\rangle$ and eigenvalues $E_m(\lambda)$ determined by the time-independent Schrödinger equation $H(\lambda)\,|m(\lambda)\rangle = E_m(\lambda)\,|m(\lambda)\rangle$ $(m = 1, 2, ..., N)$. In this notation, the Berry connection is $\mathcal{A}_m^\mu = i\,\langle m(\lambda)\,|\,\partial_{\lambda_\mu}\,|\,m(\lambda)\rangle$ $(\mu = 1, 2, ..., l)$. Then we define:

$$\Delta_{mn} = \mathcal{A}_n - \mathcal{A}_m + \frac{\mathrm{d}}{\mathrm{d}t}\arg\langle m|\dot{n}\rangle\,, \tag{1.23}$$

where $\mathcal{A}_m = \mathcal{A}_m^\mu \dot{\lambda}_\mu$, the overhead "." is the time-derivative, and arg is the complex argument of the interlevel matrix element $\langle m|\dot{n}\rangle$. This gives the adiabatic solution to the time-dependent Schrödinger equation $i\partial_t\,|\psi_m(\lambda(t))\rangle = H(\lambda(t))\,|\psi_m(\lambda(t))\rangle$ as

$$|\psi_m(t)\rangle = \exp\left[-\frac{i}{\hbar}\int_0^t E_m(\tau)\,\mathrm{d}\tau\right]|\widetilde{m}(t)\rangle\,, \tag{1.24}$$

where $|\widetilde{m}(t)\rangle = \exp[\int i\mathcal{A}_m \, \mathrm{d}t] \, |m(t)\rangle$, if the initial state is $|\psi_m(0)\rangle = |m(0)\rangle$. Then, $\Delta_{mn}$ can be rewritten as:

$$\Delta_{mn} = \frac{\mathrm{d}}{\mathrm{d}t} \arg \left\langle \widetilde{m} \,\middle|\, \dot{\widetilde{n}} \right\rangle . \tag{1.25}$$

We see that $\Delta_{mn}$ is gauge-invariant under U(1)⊗U(1) local gauge transformations (see Eq. (1.10)). The authors of Ref. [173] showed that when $\Delta_{mn}$ is applied to time-dependent systems, the quantum adiabatic condition for nondegenerate systems can be improved to describe the instantaneous energy gaps more appropriately. This improved condition states that if we have adiabaticity, for nondegenerate systems with $m \neq n$:

$$\frac{|\langle m \,|\, \dot{n} \rangle|}{|E_m(t) - E_n(t) + \Delta_{mn}(t)|} \ll 1. \tag{1.26}$$

What is remarkable and most relevant to our discussion is that $\Delta_{mn}$ was shown to be equivalent to the *geodesic curvature* $k_g$ of the path of the magnetic field orientation on the Bloch sphere.

### *1.2.2 Novel Gauge-Invariant Quantum Interlevel Index*

Xu et al. [180] used the equivalence between $\Delta_{mn}$ Eq. (1.23) and the geodesic curvature in differential geometry to derive a quantum mechanical analog of the Gauss-Bonnet theorem Eq. (1.21) generalized to the case of a manifold with boundary. This theorem states that for a 2-dimensional compact Riemannian manifold $\mathcal{M}$ with smooth boundary $\partial\mathcal{M}$,

$$2\pi\chi(\mathcal{M}) \;=\; \iint_{\mathcal{M}} K \; \mathrm{d}A + \int_{\partial\mathcal{M}} k_g \, \mathrm{d}s, \tag{1.27}$$

where $\mathrm{d}A$ is the area element of the surface $\mathcal{M}$ and $\mathrm{d}s$ is the line element of the boundary $\partial\mathcal{M}$. It should be noted that the line integral of $k_g$ along a closed loop (the boundary) is the *total geodesic curvature* of the closed curve, i.e., the *total rotation* (holonomy) of the curve's tangent vector relative to geodesic (parallel) transport. By convention, a counterclockwise loop indicates that the area of integration is the region inside the loop. On the other hand, the area integral above is the *total Gaussian curvature* of the region enclosed by the loop, i.e., the accumulated intrinsic curvature of that patch of surface. Together, they give the Euler characteristic of the region enclosed by the loop which characterizes the topology of the manifold with boundary. Note

that the full version of the Gauss-Bonnet theorem includes a term that sums any corner angles if the boundary is piecewise-smooth with sharp corners. This term does not exist in our case since we consider an adiabatic loop that is smooth across the entire loop.

With the above setup in mind, the authors defined a new differential 1-form $\omega$ and 2-form $\mathrm{d}\omega$ (c.f. the conventional forms we saw in Section 1.1.3):

$$\omega = (\mathcal{A}_n^\mu - \mathcal{A}_m^\mu)\,\mathrm{d}\lambda^\mu, \quad \mathcal{F} = \mathrm{d}\omega = \mathcal{F}_n - \mathcal{F}_m, \tag{1.28}$$

where d is the exterior derivative, and $\mathcal{F}_m$ is as defined in Eq. (1.15). Then, using $\mathcal{F}$ as the quantum mechanical analog of the Gaussian curvature $K$, the authors defined the quantum mechanical analog of the Gauss-Bonnet theorem with boundary for an $N$-level quantum system Eq. (1.2), introducing a novel gauge-invariant topological interlevel quantized character $\Theta_{mn}$ analogous to the Euler characteristic $\chi$:

$$\begin{aligned} 2\pi\Theta_{mn} &= \iint_{\mathcal{M}} \mathcal{F} - \int_{\partial\mathcal{M}} \Delta_{mn}\,\mathrm{d}t \\ &= \Phi_m - \Phi_n - \int_{\partial\mathcal{M}} \mathrm{darg}\,\langle m|\dot{n}\rangle \\ &= \Delta\Phi - \int_{\partial\mathcal{M}} \mathrm{darg}\,\langle m|\dot{n}\rangle\,, \end{aligned} \tag{1.29}$$

where the *net number of Berry singularities* is $\Delta\Phi = \Phi_m - \Phi_n$, and the number of Berry singularities $\Phi_m$ is as defined in Eq. (1.17). A key observation is that $\Theta_{mn}$ is manifestly gauge-invariant, since a gauge transformation of the form in Eq. (1.10) will leave $\Theta_{mn}$ unchanged. This gauge invariance is indicative of physical manifestations of $\Theta_{mn}$. Indeed, Part I of this dissertation presents two new applications of this interlevel index. Another crucial observation is that $\Theta_{mn}$ is manifestly quantized as an integer, since $\Delta\Phi$ in Eq. (1.29) counts the number of Berry singularities (an integer). And because the line integral $W[z] = \int_{\partial\mathcal{M}} \mathrm{darg}\,\langle m|\dot{n}\rangle$, which we shall refer to as the *winding integral* in this work, counts the number of times (an integer) the complex-valued $z(t) = \langle m|\dot{n}\rangle$ winds around the origin of the complex plane. For completeness, we mention that in Ref. [180], the authors also introduced a version of $\Theta_{mn}$ for degenerate systems. We also note that the *interlevel index* Eq. (1.29) above is slightly different from the *interband index* we focus on in this work, both notationally

and contextually. The interband index will be introduced in the next section.

A brief discussion on the differential geometric picture is due. This picture is contextualized by a curve $\mathbf{X}(s)$ (parameterized by arc length $s$) on a 2-dimensional manifold in 3-dimensional real space $\mathbb{R}^3$. $\mathbf{X}(s)$ is the displacement vector for a point on the curve. The geodesic curvature $k_g$ is the deviation of the curve from the local *geodesics* (locally distance-minimizing curves). The tangent vectors $\mathbf{V}(s)$ along the curve $\mathbf{X}(s)$ live in the tangent space at position $\mathbf{X}(s)$. If $\mathbf{V}(s)$ is parallel transported along $\mathbf{X}(s)$, $k_g = \mathrm{d}\theta/\,\mathrm{d}s$, where $\theta$ is the angle between $\mathbf{V}(s)$ and the velocity vector $\mathbf{T}(s) = \mathrm{d}\mathbf{X}(s)/\,\mathrm{d}s$. We can draw analogies between this picture and the quantum mechanical one represented by Eq. (1.29). For a 2-dimensional parameter space that lives in Hilbert space, we consider the 'curve' $|\widetilde{n}(t)\rangle$ (recall from Section 1.2.1 that the overhead tilde implies inclusion of the Berry phase: $|\widetilde{n}(t)\rangle = \exp[\int i\mathcal{A}_n\,\mathrm{d}t]\,|n(t)\rangle$). This curve is parameterized by time $t$ in the Hilbert space. $|\dot{\widetilde{n}}(t)\rangle$ is the analogy of the 'tangent' vector, and $|\widetilde{m}(t)\rangle$ corresponds to the parallel-transported vector field along the curve. Then, $\Delta_{mn} = \mathrm{d}\theta/\,\mathrm{d}t$ is the time-derivative of the angle $\theta = \arg\left\langle \widetilde{m} \middle| \dot{\widetilde{n}} \right\rangle$. This setup is illustrated in Fig. 1.2.

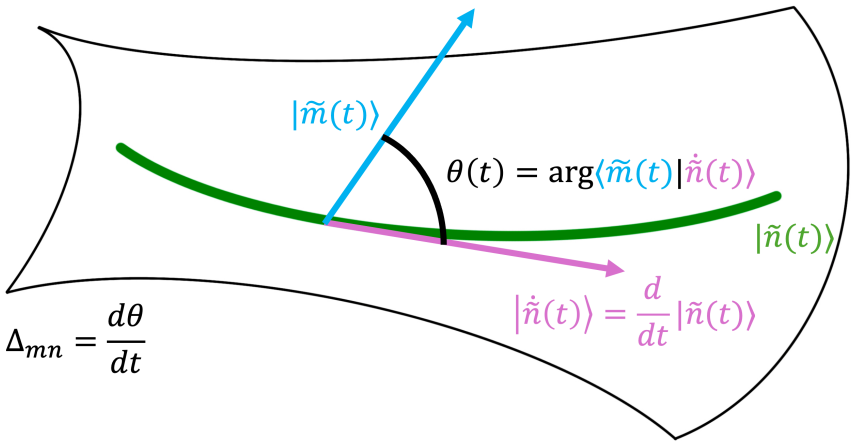


Figure 1.2: Context underlying the interlevel index Eq. (1.29) in a 2-dimensional parameter space manifold living in Hilbert space. The quantum mechanical notation in the figure is analogous to notation from differential geometry: $|\widetilde{n}(t)\rangle \leftrightarrow \mathbf{X}(s)$, $|\dot{\widetilde{n}}(t)\rangle \leftrightarrow \mathbf{T}(s)$, $|\widetilde{m}(t)\rangle \leftrightarrow \mathbf{V}(s)$, $\theta(t) \leftrightarrow \theta(s) = \angle(\mathbf{V}(s), \mathbf{T}(s))$, and $\Delta_{mn} \leftrightarrow k_g$.

The authors of Ref. [180] illustrate the quantization and gauge invariance of $\Theta$ using the simple 2-level Hamiltonian given in Section 4.2.2. To calculate $\Theta$ in this example, we could consider the

gauge in Eq. (4.18). In that gauge, $\Phi_m = 2\pi$ if $\partial\mathcal{M}$ encloses the north pole, $\Phi_n = -2\pi$ if it encloses the south pole, and $\Phi_m = \Phi_n = 0$ otherwise. On the other hand $\arg z(t) = \arg\langle m|\dot{n}\rangle = \arg[(\dot{\theta} - i\sin\theta\dot{\phi})/2]$. For a closed loop $\partial\mathcal{M}$, $z(t)$ is a closed loop in the complex plane. The winding number of $z(t)$ relative to the complex origin is the winding integral $W[z]$ defined earlier. If $\partial\mathcal{M}$ does not enclose the north/south pole, $W[z] = -2\pi$. Similar analyses reveal that $\Theta = 1$ for any $\mathcal{M}$ on the sphere.

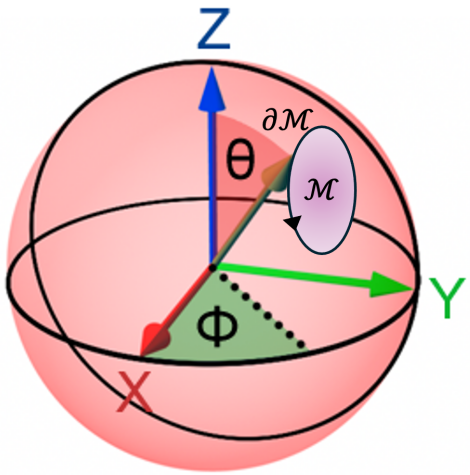


Figure 1.3: Bloch sphere parameter space parameterized by $(\theta, \phi)$ for the 2-level Hamiltonian in Section 4.2.2. The loop $\partial\mathcal{M}$ defines the boundary of the submanifold $\mathcal{M}$ of the sphere for which the interlevel index $\Theta$ may be calculated. $X, Y, Z$ are Cartesian axes, and the dark green arrow indicates a normal vector at a point along $\partial\mathcal{M}$.

### *1.2.3 Novel Quantum Interband Index*

To make its relevance to 2-dimensional condensed matter systems more apparent, we rewrite the $\lambda$-dependent interlevel index Eq. (1.29), which we refer to as $\Theta_\lambda$, explicitly in terms of momentum $\mathbf{k}$-space parameters by stripping the original format of its explicit time($\lambda$)-dependence. For specificity, we will focus on 2-dimensional $k$-space $(k_x, k_y)$ with loops parameterized by time $t \equiv \lambda$ and use the same setup as in the previous section.

For this derivation, first recall that if a function $F(k)$ is integrated over a loop parameterized

by $t$, the integration element $\mathrm{d}k$ becomes $|\dot{k}|\,\mathrm{d}t$ (where $|\dot{k}| = |\frac{\mathrm{d}k}{\mathrm{d}t}| = \sqrt{\dot{k}^2}$), and:

$$\oint_{\partial\mathcal{M}} F(k)\,\mathrm{d}k = \oint_{\partial\mathcal{M}} F(k(t))|\dot{k}|\,\mathrm{d}t. \tag{1.30}$$

Similarly, the winding integral $W[z]$ of $\Theta_\lambda$ becomes:

$$\oint_{\partial\mathcal{M}} \frac{\mathrm{d}}{\mathrm{d}t}\arg\left\langle m\left|\frac{\mathrm{d}}{\mathrm{d}t}n\right.\right\rangle \mathrm{d}t = \oint_{\partial\mathcal{M}} \frac{\partial}{\partial\mathbf{k}}\arg\left\langle m\left|\frac{\mathrm{d}}{\mathrm{d}t}n\right.\right\rangle \mathrm{d}\mathbf{k}\frac{1}{|\dot{k}|}, \tag{1.31}$$

where we applied the total derivative assuming that the left hand side is a function of $t$ while the right hand side is a function of $\mathbf{k}$. Recall that for a function $f(t)$ of variable $t$, the total derivative gives $\mathrm{d}f = \frac{\mathrm{d}f}{\mathrm{d}t}\,\mathrm{d}t$, and that for a function $f(x,y)$ of variables $x, y$, the total derivative gives $\mathrm{d}f = \frac{\partial f}{\partial x}\,\mathrm{d}x + \frac{\partial f}{\partial y}\,\mathrm{d}y$.

However, $\langle m|\frac{\mathrm{d}}{\mathrm{d}t}n\rangle$ is still in terms of $t$. So, we use the chain rule to get:

$$\begin{aligned}\oint_{\partial\mathcal{M}} \mathrm{d}\arg\left\langle m\left|\frac{\mathrm{d}}{\mathrm{d}t}n\right.\right\rangle \frac{1}{|\dot{k}|} &= \oint_{\partial\mathcal{M}} \mathrm{d}\arg\left\langle m\left|\frac{\partial}{\partial\mathbf{k}}n\right.\right\rangle \frac{\dot{k}}{|\dot{k}|} \\ &= \oint_{\partial\mathcal{M}} \mathrm{d}\arg\langle m|\nabla_{\mathbf{k}}n\rangle\cdot\hat{e}_\tau,\end{aligned} \tag{1.32}$$

where we used $\frac{\mathrm{d}}{\mathrm{d}t} = \frac{\partial}{\partial k_i}\dot{k_i} = \frac{\partial}{\partial k_x}\dot{k_x} + \frac{\partial}{\partial k_y}\dot{k_y}$ in the first equality above, $\hat{e}_\tau = \frac{\dot{k}}{|\dot{k}|} \equiv \frac{\partial}{\partial k_i}\hat{e}_{\tau_i} \equiv \frac{\partial}{\partial k_x}\hat{e}_{\tau_x} + \frac{\partial}{\partial k_y}\hat{e}_{\tau_y}$ is the unit tangent vector to a point on $\partial\mathcal{M}$, and $\nabla_{\mathbf{k}}$ is the vector differential operator. This gives us expressions for the new $\Theta_k$ that are devoid of time-dependence, which we introduced in Ref. [38]:

$$\begin{aligned}2\pi\Theta_k \equiv 2\pi\Theta_{mn} &= \Delta\Phi - \oint_{\partial\mathcal{M}} \mathrm{d}\arg\langle m\,|\,\nabla_{\mathbf{k}}n\rangle\cdot\hat{e}_\tau \\ &= \Delta\Phi - \oint_{\partial\mathcal{M}} \mathrm{d}\arg\frac{\langle m\,|\,\nabla_{\mathbf{k}}H\,|\,n\rangle}{E_{nm}}\cdot\hat{e}_\tau,\end{aligned} \tag{1.33}$$

where the second equality above follows from Eq. (1.18) with $E_{nm} = E_n - E_m$. This setup is illustrated in Fig. 1.4. We use the methods in Chapter 4 to calculate $\Theta$.

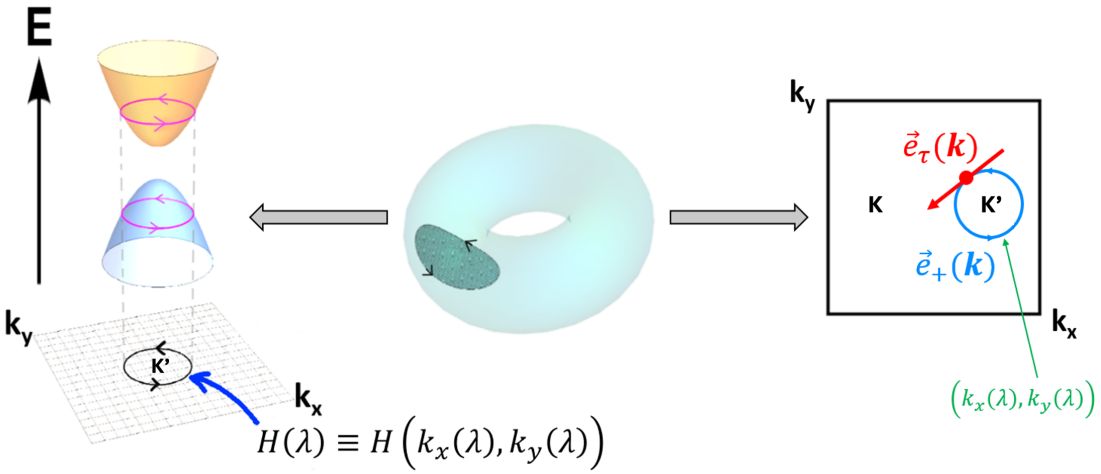


Figure 1.4: *Center:* 2D $k$-space Brillouin torus for a 2-level system. The counterclockwise loop is $\partial\mathcal{M}$, and defines the shaded region of the torus as $\mathcal{M}$ by convention. *Left:* Two bands of the dispersion E (valence and conduction bands of a material system, for example) for a region near a high-symmetry point. If the $\mathbf{k}$-space loop is parameterized by $\lambda$, the expressions $H(\lambda) \equiv H(k_x(\lambda), k_y(\lambda))$ are equivalent descriptions of the adiabatic loop $\partial\mathcal{M}$ shown on the Brillouin zone underlying E. $\Phi_m$ and $\Phi_n$ in (1.33) count the number of Berry singularities inside $\mathcal{M}$. *Right:* For $\mathbf{k}$ constrained to a closed loop $\partial\mathcal{M}$, the tangential vector $\vec{e}_\tau(k)$ at a point is denoted in red. $\mathbf{K}, \mathbf{K}'$ are high-symmetry points. For the discussion in Chapter 3, we mention that the uniquely-determined counterclockwise chiral operator $\vec{e}_+(k)$ for $\Theta_+$ may be represented by the same $\partial\mathcal{M}$. $\Theta_-$ would have used the same loop, but instead with the clockwise-oriented chiral operator $\vec{e}_-(k)$.

### *1.2.4 Interband Frequency*

Arguably, the notation used in the definition of the inter-level/band index does not make it straightforward to understand how the index behaves. To shed more light into it, we rewrite Eq. (1.29) as follows, as we introduced in Ref. [38]:

$$2\pi\Theta_{mn} = \iint_{\mathcal{M}} F_n - \iint_{\mathcal{M}} F_m - \oint_{\partial\mathcal{M}} \mathrm{Im}\frac{\langle m|\ddot{H}|n\rangle}{\langle m|\dot{H}|n\rangle} - \oint_{\partial\mathcal{M}} \sum_{q\neq m,n} \frac{1}{E_{nq}}\left(2 - \frac{E_{nm}}{E_{qm}}\right)\mathrm{Im}\frac{\langle m|\dot{H}|q\rangle\langle q|\dot{H}|n\rangle}{\langle m|\dot{H}|n\rangle}. \tag{1.34}$$

The above expression is derived using the mathematical relation $\mathrm{d}\arg z = \mathrm{Im}\frac{\mathrm{d}z(\lambda)}{z(\lambda)}$ for $z(\lambda) \in \mathbb{C}\backslash\{0\}$. We now define the overhead dot $\dot{}$ and d to both denote derivation with respect to $\lambda$. To prove this relation, notice that $z = |z|e^{i\mathrm{Arg}(z)}$ implies that $\log z = \log|z| + i\mathrm{Arg}(z)$. Although Arg is defined only up to a constant multiple of $2\pi$ ($\equiv c$), this ambiguity disappears when we take the derivative: $\frac{\mathrm{d}}{\mathrm{d}\lambda}\arg(z) = \frac{\mathrm{d}}{\mathrm{d}\lambda}(\mathrm{Im}\log\frac{z}{|z|} + c) = \mathrm{Im}\frac{\dot{z}}{z}$. Note that the derivative of $\arg(z)$ is well-defined locally when $z \in \mathbb{C}\setminus\{0\}$. Consider a general $N$-level model with non-degenerate bands. Then, for $z(\lambda) = \langle m|\dot{n}\rangle$:

$$\begin{aligned} \mathrm{d}\arg\langle m|\dot{n}\rangle &= \mathrm{Im}\frac{\mathrm{d}\langle m|\dot{n}\rangle}{\langle m|\dot{n}\rangle}, \\ \text{and } \mathrm{Im}(\mathrm{d}\langle m|\dot{n}\rangle) &= \mathrm{Im}(\langle\dot{m}|\dot{n}\rangle + \langle m|\ddot{n}\rangle). \end{aligned} \tag{1.35}$$

Then, for levels $|m\rangle, |n\rangle$ and $|q\rangle$,

$$\begin{aligned} \langle\dot{m}|\dot{n}\rangle &= \sum_q \langle\dot{m}|q\rangle\langle q|\dot{n}\rangle \\ &= \langle\dot{m}|m\rangle\langle m|\dot{n}\rangle + \langle\dot{m}|n\rangle\langle n|\dot{n}\rangle + \sum_{q\neq m,n}\langle\dot{m}|q\rangle\langle q|\dot{n}\rangle \\ &= -\langle m|\dot{m}\rangle\langle m|\dot{n}\rangle - \langle m|\dot{n}\rangle\langle n|\dot{n}\rangle - \sum_{q\neq m,n}\langle m|\dot{q}\rangle\langle q|\dot{n}\rangle \\ &= \langle m|\dot{n}\rangle\left[i\mathcal{A}_m + i\mathcal{A}_n - \sum_{q\neq m,n}\frac{\langle m|\dot{q}\rangle\langle q|\dot{n}\rangle}{\langle m|\dot{n}\rangle}\right], \end{aligned} \tag{1.36}$$

where we used the definition for the Berry connection $\langle a|\dot{a}\rangle = -i\mathcal{A}_a$ and the relation $\mathrm{d}\langle a|b\rangle = \mathrm{d}(0)$ implies that $\langle\dot{a}|b\rangle = -\langle a|\dot{b}\rangle$ for orthonormal states $\{|a\rangle, |b\rangle\}$.

To treat the last term in (1.35), recall that for any two functions $f, g$ of $\lambda$, the second derivative is $\mathrm{d}^2(fg) = (\mathrm{d}^2 f)g + 2(\mathrm{d}f)(\mathrm{d}g) + f(\mathrm{d}^2 g)$. Applying this to Schrödinger's equation $H|n\rangle = E_n|n\rangle$ gives:

$$\ddot{E}_n|n\rangle + 2\dot{E}_n|\dot{n}\rangle + E_n|\ddot{n}\rangle = \ddot{H}|n\rangle + 2\dot{H}|\dot{n}\rangle + H|\ddot{n}\rangle. \tag{1.37}$$

Applying ket $\langle m|$, using $\langle m|n\rangle = 0$ and the notation $E_{nm} = E_n - E_m$:

$$\langle m|\ddot{n}\rangle = \frac{\langle m|\dot{n}\rangle}{E_{nm}}\left(-2\dot{E}_n + \frac{\langle m|\ddot{H}|n\rangle}{\langle m|\dot{n}\rangle} + 2\frac{\langle m|\dot{H}|\dot{n}\rangle}{\langle m|\dot{n}\rangle}\right). \tag{1.38}$$

For a general $N$-level Hamiltonian, the numerator of the last term above becomes:

$$\begin{aligned}\langle m|\dot{H}|\dot{n}\rangle &= \sum_q \langle m|\dot{H}|q\rangle\langle q|\dot{n}\rangle \\ &= \langle m|\dot{H}|m\rangle\langle m|\dot{n}\rangle + \langle m|\dot{H}|n\rangle\langle n|\dot{n}\rangle + \sum_{q\neq m,n}\langle m|\dot{H}|q\rangle\langle q|\dot{n}\rangle.\end{aligned} \tag{1.39}$$

Using the Hellmann-Feynman-type relation $\langle m|\dot{H}|n\rangle = E_{nm}\langle m|\dot{n}\rangle$, the above

$$= \langle m|\dot{n}\rangle\left(\langle m|\dot{H}|m\rangle + E_{nm}\langle n|\dot{n}\rangle + \sum_{q\neq m,n} E_{qm}\frac{\langle m|\dot{q}\rangle\langle q|\dot{n}\rangle}{\langle m|\dot{n}\rangle}\right). \tag{1.40}$$

For $\beta = \{\langle m|\dot{H}|m\rangle\}$ with $\dot{E}_n \in \mathbb{R}$, we have $\mathrm{Im}(\beta) = 0$. Finally, we get:

$$\begin{aligned}\mathrm{Im}\frac{\mathrm{d}\langle m|\dot{n}\rangle}{\langle m|\dot{n}\rangle} &= \mathrm{d}\arg\langle m|\dot{n}\rangle \\ &= \mathcal{A}_m - \mathcal{A}_n + \mathrm{Im}\frac{\langle m|\ddot{H}|n\rangle}{\langle m|\dot{H}|n\rangle} + \sum_{q\neq m,n}\mathrm{Im}\frac{\langle m|\dot{q}\rangle\langle q|\dot{n}\rangle}{\langle m|\dot{n}\rangle}\left(2\frac{E_{qm}}{E_{nm}} - 1\right) \\ &= \mathcal{A}_m - \mathcal{A}_n + \mathrm{Im}\frac{\langle m|\ddot{H}|n\rangle}{\langle m|\dot{H}|n\rangle} + \sum_{q\neq m,n}\mathrm{Im}\frac{\langle m|\dot{H}|q\rangle\langle q|\dot{H}|n\rangle}{\langle m|\dot{H}|n\rangle}\left(\frac{2}{E_{nq}} - \frac{E_{nm}}{E_{qm}E_{nq}}\right).\end{aligned} \tag{1.41}$$

When plugged into Eq. (1.29), we get Eq. (1.34).

Notice that all terms in Eq. (1.34) are gauge-independent following gauge transformations of the form Eq. (1.10), and so, potentially observable. The first two terms in the right hand side of Eq. (1.34) make the difference between the Berry curvature integrals. The third boundary term

includes $\langle m|\ddot{H}|n\rangle/\langle m|\dot{H}|n\rangle$, which we call the *interband frequency*, since it resembles the ratio of an acceleration-like quantity to a velocity-like quantity. Since $k \to \infty$ implies the loop-parameter (e.g., time) $\lambda \to \infty$, we intuit that the frequency ($\propto 1/\lambda$) $\to 0$. We show later in Fig. 2.1 that as $k \to \infty$, this correction term also tends to 0 in our numerical calculations on 2-band models. To our knowledge, the interband frequency is new to the literature. Due to its dependence on the tangential vector $\hat{e}_\tau$, a unique vector field may be defined only *after* a loop is chosen. This makes the individual terms in the interband frequency ratio differ from existing quantities in the literature (such as the interband acceleration in second order nonlinear responses [63, 77]).

### *1.2.5 Hilbert Space Picture*

For intuition on the behavior of the winding element $\oint_{\partial\mathcal{M}} \mathrm{d}\arg\langle m\,|\,\nabla_k n\rangle\cdot\hat{e}_\tau \equiv \oint_{\partial\mathcal{M}} \mathrm{d}\arg\left\langle m\,\middle|\,\frac{\mathrm{d}}{\mathrm{d}\lambda}n\right\rangle$ appearing in the interband index Eq. (1.33), we refer the reader to Figure 1.5. Notice that we use the single-parameter version of the interband index $\Theta(\lambda) \equiv \Theta_\lambda$ instead of the $\Theta(k_x, k_y) \equiv \Theta_{\mathbf{k}}$ given previously. To help illustrate key points using Figure 1.5, we use a fictitious model and assume a convenient energy dispersion $E$ (bottom-left). The figure in the center is a 3-band extension of the 2-band illustration proposed by Haldane in [57]. The **k**-space torus (top-left) for each band is geometrically illustrated as tori (center). We partially represent the Berry curvature by the local curvature of the torus (with peaks representing high Berry curvature, for instance). As shown by the band diagram at the bottom-left, $E_A = E_B$ at the $K'$ point. While this degeneracy leads to a Berry curvature singularity in **k**-space, it is a 'wormhole' in Hilbert space (as indirectly depicted in the bottom-center by the link between tori for $|A\rangle$ and $|B\rangle$). The other band extrema (bottom-left) may correspond to potential gap closing points often associated with high-symmetry points and large sources of Berry curvature flux (torus peaks in the center). The red loops in the center are Hilbert space vector trajectories mapped from the blue **k**-space loop on the top-left, to the **k**-space tori in the center. Depending on details of the Hamiltonian, the orientation of these red loops in Hilbert space may be different from the **k**-space loop's (clockwise, etc.). One may calculate the interband indices $\Theta_{BA}, \Theta_{CA}$ and $\Theta_{CB}$ if the system is fully-gapped (i.e. if the degeneracy at $K'$ did not exist). These indices would describe the topology of the regions defined by the blue loop in the top-left (which are mapped to the red loops in the center). The inset on the right shows the

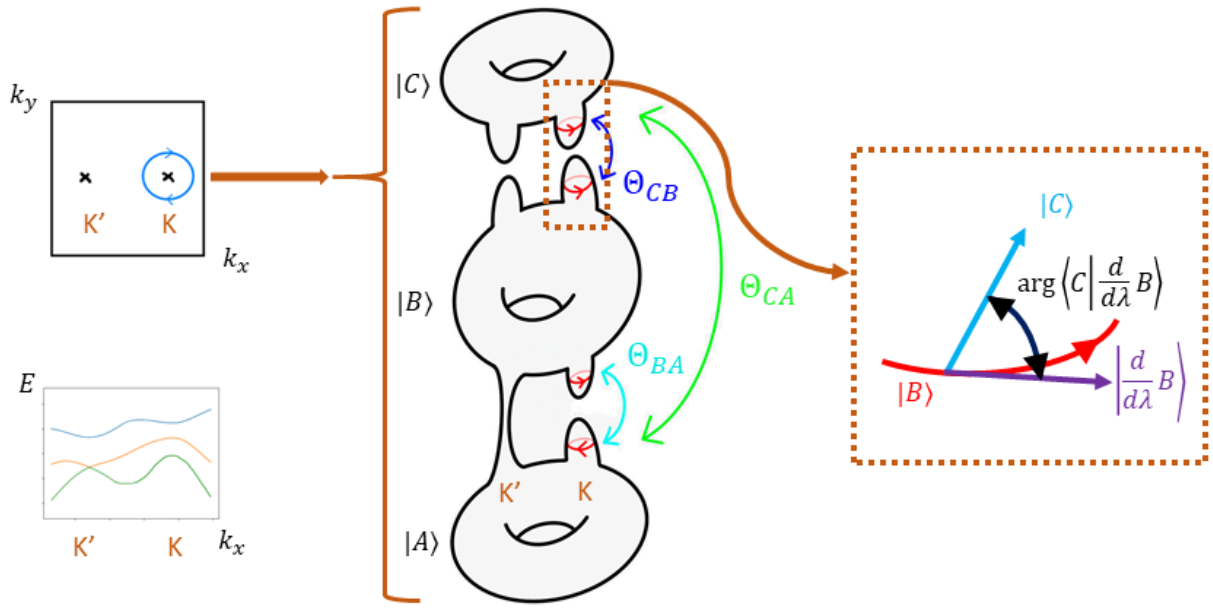


Figure 1.5: Example **k**-space geometric, and Hilbert space picture of an arbitrary 3-band model with states $|A\rangle, |B\rangle, |C\rangle$ ($E_A < E_B < E_C$).

eigenstates involved in $\Theta_{CB}$, as vectors in Hilbert space. Since the terms $\mathcal{A}_B - \mathcal{A}_C + \mathrm{d}\arg\left\langle C \,\middle|\, \dot{B}\right\rangle$ in the definition of $\Theta(\lambda)$ was proposed as a quantum mechanical analog of the geodesic curvature from differential geometry [180, 198], they may be interpreted as the rate of rotation of the tangent to the curve, around the normal to some regular, oriented surface. In other words, it is the rate of angular rotation of the 'parallel-transported' 'tangent' $|C\rangle$ moving along the curve specified by $|B\rangle$ with 'velocity' $|\dot{B}\rangle$ [156, 180]. Then, the geodesic curvature's closed loop line integral along the curve may be interpreted as the *total geodesic curvature*, or the *total rotation* of the curve on the oriented surface. Disclaimer: The visualization presented in this figure must be used with caution, as it combines different standard representations of involved concepts in an unconventional way intended to illustrate the complex context underpinning the interband index formalism.

This figure is an abstract representation of Hilbert space and the **k**-space geometric/topological manifolds, inspired by Haldane's description in Ref. [57]. To quote that reference: *There is a striking analogy to the idea of 'wormholes' connecting different universes, where here the two 'universes' are Bloch bands, and 'space' is k-space.*

This concludes the introduction of the technical interband index formalism and definitions.

## *1.3 Preliminary Observations*

In this section, we present preliminary observations from when we started seeking potential applications of $\Theta$ in condensed matter systems. Since we conducted explorations from multiple angles, the subsections below might appear disjointed, with no clear flow in the presentation. The subsections are as follows: similarities between $\Theta$ and other quantities in the literature; demonstrating $\Theta_{mn} = -\Theta_{nm}$; a discussion on the tangential vector dependence of the winding element in the definition of $\Theta$; some correlations in 2-band models (between $\Theta$ and: the sign of Berry curvature; the winding integral; the orientation of the normal vector to the Bloch sphere); and a discussion on the choice of $\mathbf{k}$-space loops. Numerical methods are presented in Chapter 4.

Inspired by these observations, we go on to propose two new applications of $\Theta$, one in valley topology, and another in optical selection rules for excitons.

### *1.3.1 Similarities in Literature*

A natural part of the process of exploring the interband index involved identifying its occurrence in the literature. We verified that the interband index is a novel addition to the literature from Ref. [38,173,180]. However, $\Theta$ (or just some of the terms appearing in its definition in Eq. (1.33)), does show up in the literature at least notationally (i.e., not conceptually). We assert that $\Theta$ is fundamentally different from the following quantities.

The tangential vector dependence of $W_i$ $(i = \lambda, k)$ makes it starkly different from the similar-looking shift vector and interband frequency-like terms appearing in nonlinear optical effects [63, 77, 161]. The shift vector may be interpreted as the relative Berry phase difference between two levels, that measures the real-space displacement of an electron wavepacket's center of charge when it undergoes an interband optical transition. The same applies even to Ref. [42], that features a quantized relationship between the zone-averaged shift photocurrent and polarization differences: their approach relies on a well-defined vector field whose quantities are independent of loop choice.

Similar arguments hold for why $\Theta_k$ differs from the expression for the side-jump contribution to the quantum anomalous Hall effect [157], and other quantities involving the quantum geometric

tensor [24]. This argument also applies to the ideas presented about the so-called dipole curvature in Ref. [20], and the curvature in Ref. [161].

We also remark that a quantity like $W_k$ appears in Ref. [61]. However, this is in a different context of degenerate multiplets, and the inability to define a unique vector field doesn't allow $\Theta_k$ to be an application of the argument principle as in Ref. [61] and Ref. [42]; here we may not calculate the net number of zeros and poles for the associated meromorphic function $\langle m \,|\, \frac{\mathrm{d}}{\mathrm{d}\lambda} n \rangle$.

We also mention that the quantity $\langle m \,|\, \frac{\mathrm{d}}{\mathrm{d}\lambda} n \rangle$ has been in the literature for a while, in the contexts of non-Abelian Berry phases, so-called off-diagonal Manini-Pistelosi phases [113], and Bargmann invariants [124, 125]. However, we emphasize that these quantities are not quantized and generally have more constraints and different applications.

$W_k$ is indeed similar to the interband matrix element occurring in optical selection rules for excitons, and this is explored in Chapter 3 as a new application of $\Theta$.

We separately remark that the expression for the number of Berry singularities Eq. (1.17) has appeared in the calculation of the $\mathbb{Z}_2$ index [44].

Besides notation, some other potential avenues for conceptual exploration might be the following. Note that the author is not well-versed in the following areas, and so the following might not be applicable at all. However, they are presented here to encourage the reader to think about and potentially investigate how the interband index plays into the following science concepts: Understanding interband frequency using planar geometry; reframing the interband index using the time-dependent Schrodinger formalism in the Heisenberg picture and Ehrenfest's theorem; covariant acceleration from quantum field theory; interband index in terms of Christoffel symbols; interband index in polar basis; de Rham cohomology; fiber bundle perspective; second-order tangent bundles; argument principle, ramification index and Poincare-Hopf; Atiyah-Patodi-Singer index theorem; extending definition to include sharp corners (preliminary analyses support that these terms do not exist in adiabatic evolutions); spectral flow; semiclassical dynamics; side-jump scattering and Bloch wavepacket picture; transition amplitude in second-order perturbation theory; $\mathcal{Z}_2$ insulators; Haldane's correction to Fermi liquid theory; Manini-Pistolesi off-diagonal phase; Mead-Berry connection; exotic holonomy; gapless systems and non-Abelian interband index; index in Bargmann invariant perspective; improving quantum adiabatic theorem (as in Ref. [173]); so-called Berry flux vortices in gauge field in degenerate systems; amongst others.

For completeness, we mention that, during the time of our investigations into $\Theta$, the following works appeared citing the interband index (in addition to our own contributions Ref. [36, 38]). Their titles are: *Geodesic nature and quantization of shift vector [170]; Nonreciprocal landau–zener tunneling [77]; Nonadiabatic nonlinear optics and quantum geometry—Application to the twisted Schwinger effect [162]; Multitunneling effect of nonreciprocal Landau-Zener tunneling: Insights from DC field responses [163]; Many-body quantum geometry in time-dependent quantum systems with emergent quantum field theory instantaneously [171]; Demonstration of geometric diabatic control of quantum states [151].*

In the following subsections, we present various potentially-disjointed observations from preliminary investigations into the interband index.

### *1.3.2 Demonstrating $\Theta_{mn} = -\Theta_{nm}$*

From Eq. (1.33) $\Delta\Phi^{mn} = \Phi_m - \Phi_n = -(\Phi_n - \Phi_m) = -\Delta\Phi^{nm}$. Next, we consider the term $\langle m|\dot{n}\rangle$ (using the $\lambda$ formulation for simplicity). Notice that: $\mathrm{d}(0) = \mathrm{d}(\langle m|n\rangle) = \langle \dot{m}|n\rangle + \langle m|\dot{n}\rangle = 0$. It follows that $\langle \dot{m}|n\rangle = -\langle m|\dot{n}\rangle$. Putting all this together, we get $\Theta^{mn} = -\Theta^{nm}$.

### *1.3.3 Tangential Vector Dependence of Winding Element*

We must be careful about the derivatives in the interband winding element $z(\lambda) = \langle m\,|\dot{n}\rangle$ in Eq. (1.29). As implied by its time derivative (and as shown explicitly in $\langle m\,|\,\nabla_{\mathbf{k}} n\rangle \cdot \hat{e_\tau}$ and $\langle m\,|\,\nabla_{\mathbf{k}} H\,|\,n\rangle \cdot \hat{e_\tau}$ in Eq. (1.33)), $z(\lambda)$ explicitly depends on the tangential direction, i.e., the vector $\hat{e}_\tau$. Therefore, $z(\lambda)$ can be defined only once a $k$-space loop has been chosen (i.e. submanifold boundary). Figure 1.6 demonstrates this subtlety. This is unlike the $\lambda$-independent $k$-space derivatives that appear often in discussions of geometric properties elsewhere in the literature, where a unique vector field may be defined prior to choosing a $k$-space loop (e.g, in the usual Berry curvature $F$ which contains terms such as $\langle m\,|\nabla_k n\rangle$).

Nevertheless, even though the winding loops $z(\lambda)$ might look different on the complex plane, they might still have the same winding number if describing the same topological area and have the same $\Delta\Phi$.

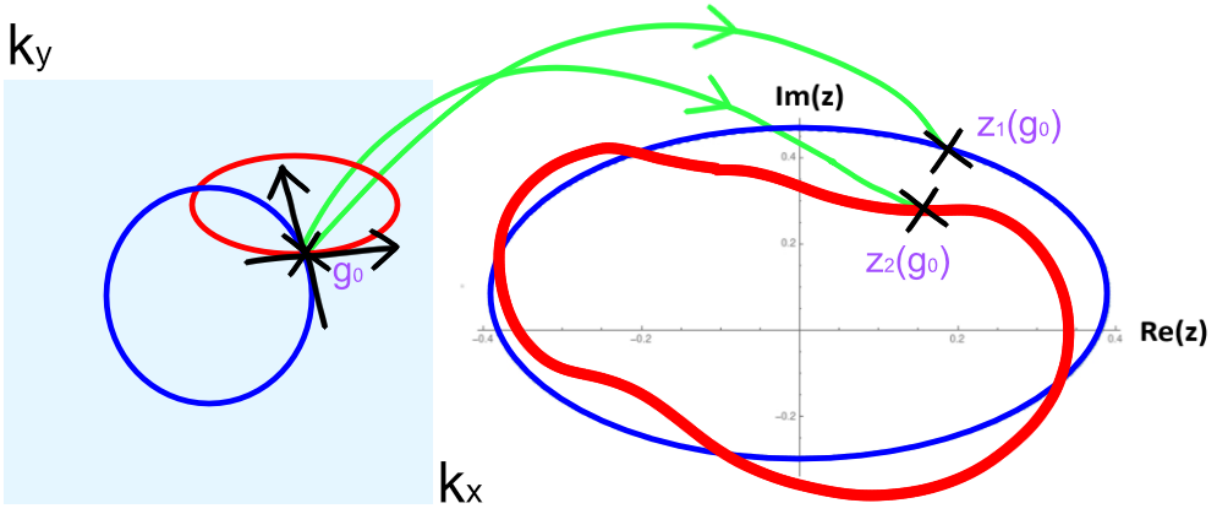


Figure 1.6: Consider a simple case where $\Delta\Phi = 0$ (no Berry singularities). Then, $\Theta = -W(\lambda)$. Now take a circular **k**-space loop $\partial\mathcal{M}_1$ (blue loop on the left) that gives $W = +1$. This $\partial\mathcal{M}_1$ gives a complex loop $z_1$ with some shape that winds counterclockwise once about the complex origin. Ignoring $\lambda$ dependence for brevity, consider a point $g_0 = (g_x, g_y)$ on the **k**-space $\partial\mathcal{M}_1$ (indicated by the **X** on the left) and notice that it is mapped to a point $z_1(g_0)$ on the complex plane (right). Then take a differently-shaped elliptical loop $\partial\mathcal{M}_2$ (red loop on the left) that also gives $W = +1$ and goes through the same **k**-space $g_0$. Notice how the tangential vector along each loop at $g_0$ points in a different direction as shown by the black arrows on the left. So, the corresponding complex loop $z_2$ will in general look different from $z_1$, as the point $g_0$ will not necessarily be mapped to the same point on the complex plane because of the different tangential directions in **k**-space. That is, $z_1(g_0) \neq z_2(g_0)$ in general. For pedagogical reasons, we assume all loops above are oriented counterclockwise and make one revolution about their origins.

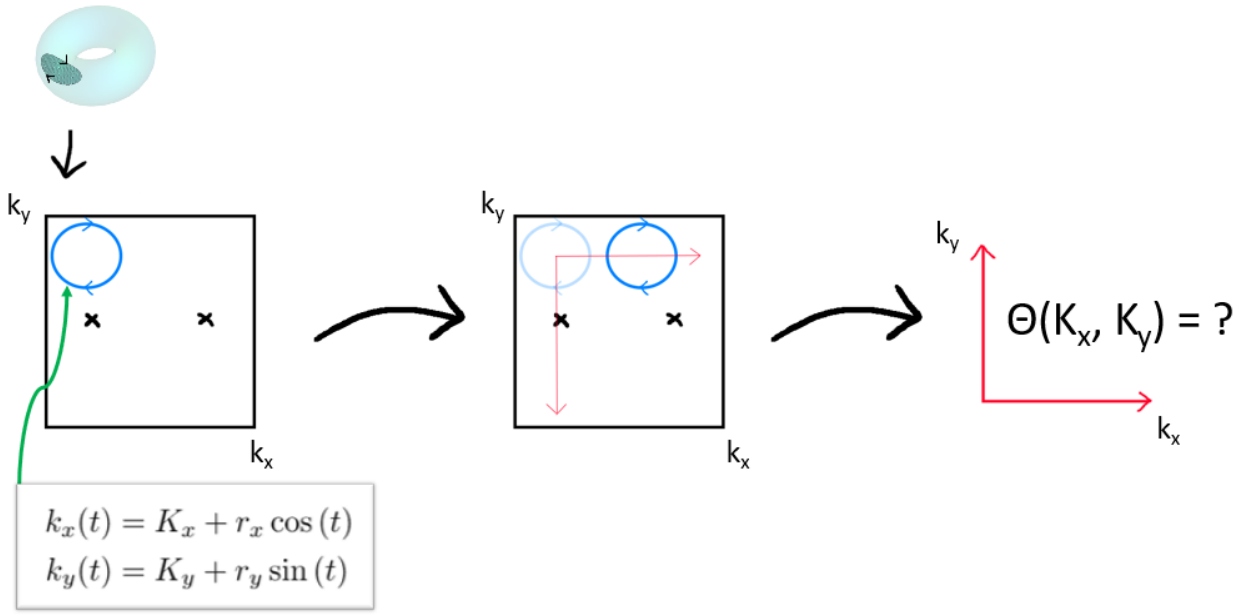


Figure 1.7: Method: Using small loops to sample the entire Brillouin zone. We calculated $\Theta$ as a function of the loop's center $(K_x, K_y)$.

### *1.3.4 2-band Models*

A few numerically-motivated results that hold for 2-band models are presented here. In this section, we use the Haldane model for the quantum anomalous Hall effect (Section 4.2.1).

*Sign of Berry curvature $F$ of either eigenstate in $\mathbf{k}$-space vs. value of interband index $\Theta$*

In 2-band models, we found that if a loop does not enclose a high-symmetry $K$ point, $\Theta$ is $\propto \mathrm{sgn}(F)$, and can take only values $\pm 1$ (i.e. $|\Theta| = |\,\mathrm{sgn}(F)| = 1$). With the exception that $\Theta = 0$ when at least one point along the $k$-space loop has $F = 0$ ($\mathrm{sgn}\, F = 0$). We use either eigenstate because, in 2-band models, $F \equiv F_m = -F_n$ due to the Berry curvature sum rule Eq. (1.20).

To see this, we used small loops to sample the entire Brillouin zone, as shown in Figure 1.7. Then we compared this with the Berry curvature, as illustrated in Figure 1.8.

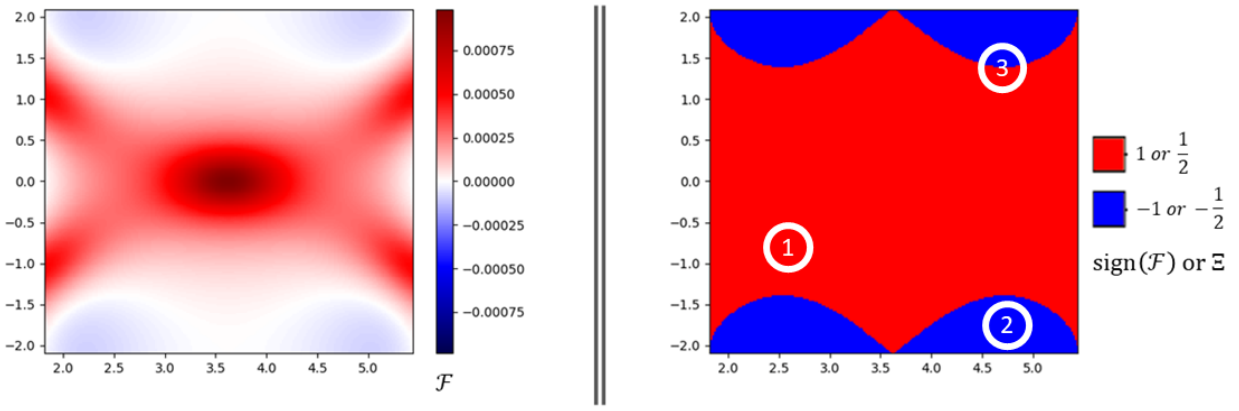


Figure 1.8: For the Haldane model with $M = 0, \phi = \pi/2$, we take very small loops (of radius 0.04) to sample the approximate area of the first Brillouin zone for insight into the behavior of $\Theta$ when it does not enclose a high-symmetry point. We do this by changing the loop's center coordinates such as to cover the entire Brillouin zone as in Figure 1.7. As shown on the right, we see that $\Theta$ is proportional to the sign of Berry curvature $F$. $F$ is plotted on the left. For loops that include regions of both $F > 0$ and $F < 0$ — i.e., when $F = 0$ at at least one point along the loop (such as in the loop labeled 3 on the right) — we see $\Theta = 0$. As shown in Figure 1.10, $\Theta = 0 = \Xi$ when the loop intersects with the Bloch sphere boundary, which correlates to $F = 0$ contours. The counterclockwise-oriented loops labeled $1, 2$ and 3 are for usage in Figure 1.10.

*Winding number vs. value of interband index* $\Theta$

We have the following correspondence between the winding number $W = \oint_{\partial\mathcal{M}} \mathrm{d}\arg z$ of loop $z = \langle m\,|\dot{n}\rangle$ (and therefore sign of Berry curvature per the preceding point above): $\Theta \propto \mathrm{sgn}(W) \propto \mathrm{sgn}(F)$, and $\Theta = W = 0$ when at least one point along the $\mathbf{k}$-space loop has $F = 0$. This is numerically seen in the absence of Berry singularities ($\Delta\Phi = 0$), which gives $\Theta = -W(\lambda)$. However, we illustrate this further visually in Figure 1.9.

*Interband index* $\Theta$ *vs. orientation of normal vector to the Bloch sphere (a.k.a. pseudospin surface)*

We also found a correspondence between the interband index $\Theta$ and the orientation of the normal vector along the $\mathbf{k}$-space loop when mapped to the Bloch sphere.

Note that a $2\times 2$ Hamiltonian $H(\mathbf{k})$ may be written in terms of the Pauli matrices $\sigma_i$: $H(\mathbf{k}) = h_0(\mathbf{k})\,\sigma_0 + \mathbf{h}(\mathbf{k})\cdot\boldsymbol{\sigma}$, with $\mathbf{h}(\mathbf{k}) = (h_x, h_y, h_z)$ and $\boldsymbol{\sigma} = (\sigma_x, \sigma_y, \sigma_z)$. The closed 2D $k$-space Brillouin zone/torus can therefore be mapped to the closed oriented surface (Bloch sphere) via a vector comprising the above $\mathbf{h}(\mathbf{k})$. For the Haldane model used in this section, $\mathbf{h}(\mathbf{k})$ is given in Eq. (4.15). Due to the role of the Pauli matrices' mapping to the spin-1/2 Hamiltonian Eq. (4.2.2), we could also call this Bloch sphere a *pseudospin surface*. In this picture, the direction of the 3-vector $\mathbf{h}(\mathbf{k})$ plays the role of a momentum-dependent "magnetic field" in the 2-level space, and its winding over the Brillouin zone encodes the band topology. Since $h_0(\mathbf{k})\,\sigma_0$ only shifts both bands uniformly in energy and does not affect the relative orientation of the pseudospin vector $\mathbf{h}(\mathbf{k})$, it can be dropped when discussing band topology.

To clarify, the pseudospin surface for the Haldane model Eq. (4.15) $\mathbf{h}(k) = \mathbf{h}(k_x, k_y)$ should technically be normalized to get a sphere (c.f. so-called *Gauss map* in differential geometry). However, to facilitate illustration, we use the unnormalized Bloch sphere $\mathbf{h}(k_x, k_y)$ in this exposition. This choice of normalization does not qualitatively change the results.

In the literature (e.g., in Ref. [43]), this $\mathbf{h}(k_x, k_y)$ surface has been used as a technique to calculate the Chern number and other related topological quantities. For instance, for a given Bloch sphere, the Chern number is the number of times a ray drawn from the origin $(0, 0, 0)$ to infinity intersects with the sphere, taking the surface's orientation into account. See Figure 8 of [43].

However, in our simulations we noticed a subtlety. Consider a closed loop $\mathbf{k}(\lambda)$ in $\mathbf{k}$-space and

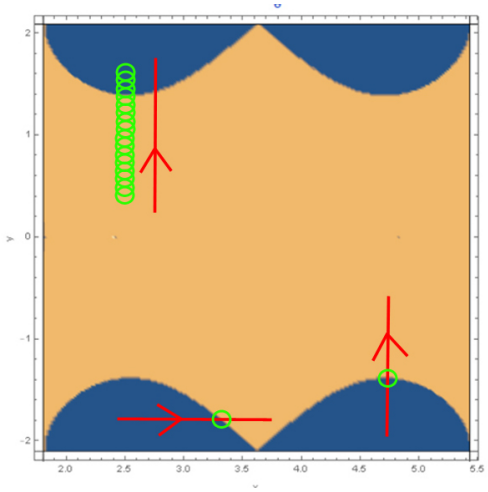

(a) We take tiny loops (in green) near the red path on the top-left to see how the interlevel winding loop $z(\lambda) = \langle m|\, \dot{n}\rangle$ changes in complex projective space. The loops at the bottom are random loops that include the boundary, which yield $\Theta = 0$. The different colors (blue vs dirty orange) correspond to regions of different $\Theta$ or Berry curvature in $(k_x, k_y)$ space (as in Figure 1.8 right).

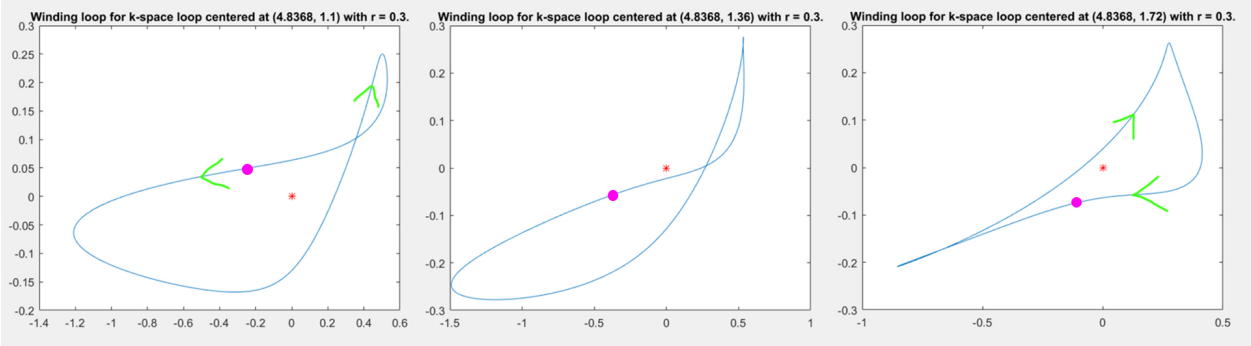


(b) As we go from the dirty orange to the blue region in Fig. (a) above, these complex winding loops $(\mathrm{Re}z, \mathrm{Im}z)$ for $z(\lambda) = \langle m|\, \dot{n}\rangle$ show how the winding number changes due to the counterclockwise loop enclosing the complex plane origin (red asterisk *) [left], not enclosing it [center], and then enclosing it again (but now clockwise) [right]. These cases give winding numbers $+1, 0$ and $-1$ respectively. Notice that the left-most loop gives $+1$ even if it appears to self-intersect because it can be contorted/untangled to make a counterclockwise unit circle without crossing the origin.

Figure 1.9: Seeing how the complex winding number term of the interband index changes.

its image on the unnormalized Hamiltonian/pseudospin/Bloch surface,

$$\mathbf{r}(\lambda) \;=\; \big(h_x(\mathbf{k}(\lambda)),\, h_y(\mathbf{k}(\lambda)),\, h_z(\mathbf{k}(\lambda))\big)\,, \tag{1.42}$$

with unit tangent

$$\mathbf{T} \;=\; \frac{d\mathbf{r}/d\lambda}{\|d\mathbf{r}/d\lambda\|} \;=\; \frac{d\mathbf{r}}{ds}, \qquad s(\lambda) = \int_0^{\lambda} \left\| \tfrac{d\mathbf{r}}{du} \right\| du. \tag{1.43}$$

The surface normal (up to a scale factor $\alpha$) is given by the cross-product of the Hamiltonian gradients,

$$\mathbf{S} \;=\; \frac{\partial H(\mathbf{k})}{\partial k_x} \times \frac{\partial H(\mathbf{k})}{\partial k_y}, \qquad \hat{S} \;=\; \frac{\mathbf{S}}{\|\mathbf{S}\|}. \tag{1.44}$$

The geodesic curvature is then

$$\kappa_g \;=\; \frac{d\mathbf{T}}{ds} \cdot \hat{S}, \tag{1.45}$$

which measures how rapidly $\mathbf{T}$ turns toward the in-plane normal $\hat{S}$. We computed $\hat{S}$ numerically over the Bloch sphere and found that its orientation correlates directly with the sign of the Berry curvature $F(\mathbf{k})$. If this holds generally, then the usual method of counting ray-intersections to obtain the Chern number could depend on the choice of projection ray (and so should be used with caution), since the relative orientation of $\hat{S}$ and that ray fixes the sign assignment; perhaps in many studied models the Berry curvature happens to be unipolar over the Brillouin zone. We visualized $\hat{S}$ only along the $\mathbf{k}$-space loop mapped to the Bloch sphere, and illustrate this and present results, in Figures 1.10 and 1.11.

*Choosing* $\mathbf{k}$*-space loops*

Above, we saw that the $\mathbf{k}$-space loop chosen determines the value of $\Theta$ (e.g., correlation to sign of Berry curvature $F$). This implies that the topology of the submanifold defined by the loop might differ based on location within the Brillouin zone. Taking into account the fact that the Haldane model has two special high-symmetry points $K$ and $K'$ that might influence topology (see Section 1.1.5), we construct $(M/t_2, \phi)$ 'phase diagrams' similar to Fig. 1.1 (a) to search for clues. We construct these diagrams by calculating $\Theta$ as $M$ and $\phi$ are varied for a fixed loop.

Fig. 1.12 is for when the loop does not include any high-symmetry points, and Figure 1.13 is

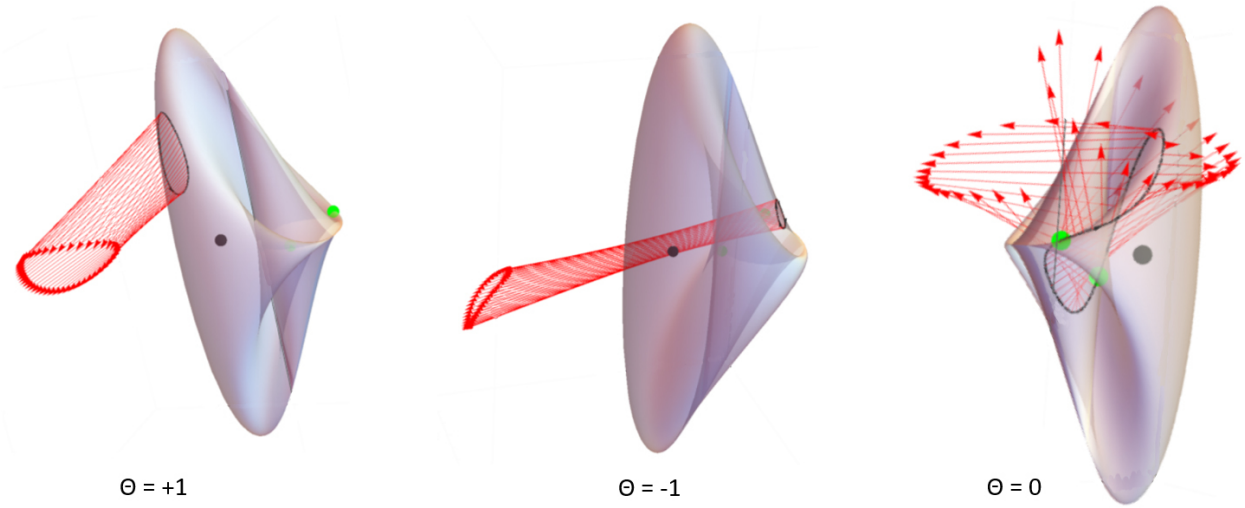


Figure 1.10: Using Figure 1.8 for reference, we map loops giving different values of $\Theta$ (loops labeled $1, 2$ and $3$) onto the unnormalized Bloch sphere surface (indicated by $\Theta = 1, -1$ and $0$ respectively for loops $1, 2$ and $3$). The origin $(h_x, h_y, h_z) = (0, 0, 0)$ is depicted by the black dot. We also plot the vectors normal to the surface along the loop (defined as $\hat{S} = \alpha(\partial H(\mathbf{k})/k_x \times \partial H(\mathbf{k})/k_y)$, for some scaling constant $\alpha$ used to emphasize the vectors' directions). We see that $\Theta = 1$ and $\Theta = -1$ give normal vectors of differing directions. Although not too visible due to the pixelation on the black loops, the $k$-space counterclockwise loop in this example is mapped to a counterclockwise pseudospin space loop when $\Theta = 1$, but to a clockwise loop when $\Theta = -1$. When $\Theta = 0$ (loop 3 in Figure 1.8), we see that the normal direction is not well-defined in pseudospin space. The green dots indicate regions where the $k$-space loop intersects the $F = 0$ boundary. This boundary of the Haldane model is probably the one discussed in Ref. [108]. If the Hamiltonian surface is normalized into the Bloch sphere, the loop appears to self-intersect (similar to the right panel in Figure 1.11 when the loop crosses a boundary). Figure 1.11 further clarifies that this behavior is due to a boundary.

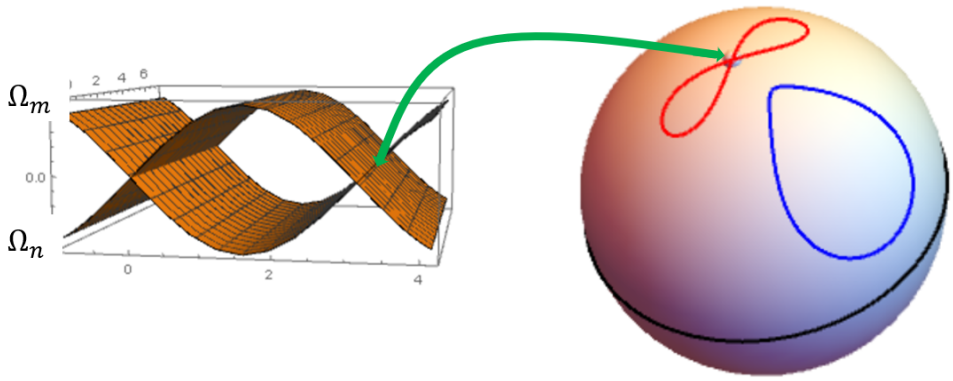


Figure 1.11: Berry curvatures of each level (left) in $(\phi, \theta)$-space mapped to the Bloch sphere (right) for the simple 2-level model for a spinor in magnetic field $B$: $H(\mathbf{k}) = B\mathbf{n} \cdot \vec{\sigma}$, for $B > 0$ and $\mathbf{n} = (\sin(\theta)\cos(\phi), \sin(\theta)\sin(\phi), \cos(\theta))$ (see Section 4.2.2; and we mapped angular variables $(\theta, \phi)$ to $(k_x, k_y)$). We observe that $\Theta = 1$ for all loops that do not intersect with the parameter space boundary, and that the sign of Berry curvature is either only positive or only negative for each level $|m\rangle, |n\rangle$ (unlike the Haldane model in Figures 1.8 and 1.10). Notice how a loop crossing the parameter space boundary is mapped to a self-intersecting loop on the Bloch sphere (and gives $\Theta = 0$). When a loop is outside the parameter space boundary (non-intersecting $F$ on the left), $\Theta$ reverses sign, clarifying the relationship to $\text{sign}(F)$. This suggests that the $\Theta = 0$ case in Figure 1.10 is due to a boundary on the Bloch sphere; but this argument needs clearer definitions and more thought.

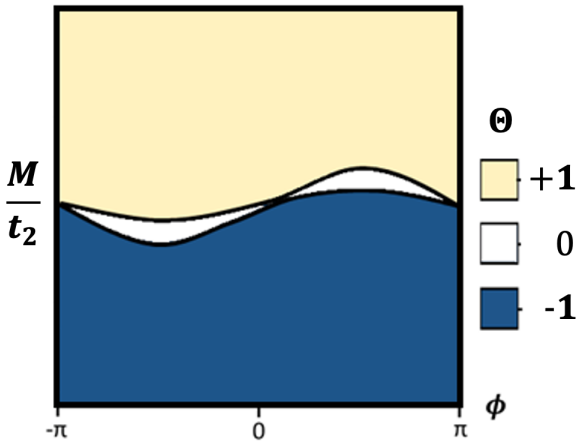


Figure 1.12: The phase diagram for a loop not centered at a high-symmetry point in the Haldane model. Above, we used a loop of radius 0.2 centered at $(2.7, 1)$. Due to the lack of nice symmetries that make the $K$ points special, we get a phase diagram that is not symmetric, and that may not be as useful in recovering quantities such as the first Chern number.

for when the loop encloses both valleys $K$ and $K'$. Besides the relationship $\Theta \propto \text{sgn}(F)$ discussed previously for the case of Fig. 1.12, it is not clear what these figures might represent because they do not seem to correspond to existing phase diagrams in the literature to the best of our knowledge. Given the geometric/topological nature of $\Theta$, there is very likely some relation to geometry/topology; but its nature is unclear. We additionally conjecture that the given 'phase diagrams' might be some indicator of the system's underlying symmetry.

Even though the cases of not having any high-symmetry points within the loop and having both points were not promising, we made headway in the case when the loop enclosed only one high-symmetry point $P$. Based on our numerical results, these $P$ are high-symmetry points associated with crystal symmetry (such as $K, K', M, \Gamma, X, ...$). They may not necessarily be points where the band gap may close. We observe that the interband matrix element $\langle m \,|\, \boldsymbol{\nabla}_{\boldsymbol{k}} n\rangle \cdot \hat{e}_\tau$ from Eq. (1.33) diverges at these $P$. However, due to the matrix element's gauge-dependence, we doubt that this observation can be used to identify $P$ besides what's already determinable via the model's prescription. This is also due to the fact that, in a non-azimuthal basis, we do not have a unique $\mathbf{k}$-space vector field prior to choosing a loop. Otherwise, its critical points may have been used to

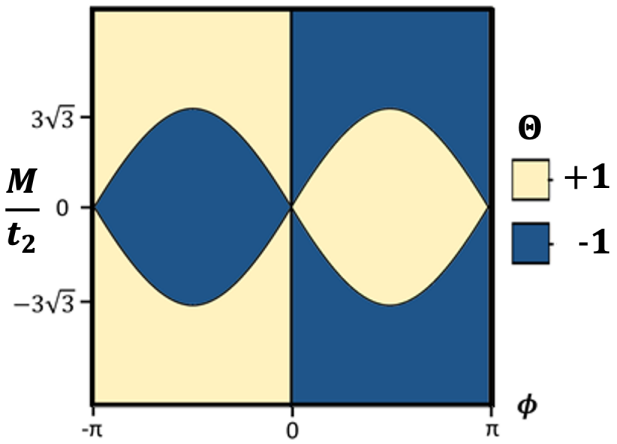


Figure 1.13: The same phase diagram for a loop enclosing both $K$ and $K'$ valleys in the Haldane model. Again, it is not clear how one may extract a useful quantity (such as the first Chern number) using this information. However, one may venture that this diagram is a result of the loop always containing at least one Berry flux-source (regardless of whether it is $K$ or $K'$), and therefore is a reflection of the system's time-reversal symmetry. We additionally observe the outline of the sinusoidal curves in the middle to be the same shape as Haldane's phase diagram given in Fig. 1.1 (a).

identify $P$. The case of having only one high-symmetry point (or *valley*) within the chosen loop forms the foundation of one of our key results that makes the content of the next chapter in the context of the application of the interband index in valley topology.

# Chapter 2

# APPLICATION I: MULTIBAND VALLEY TOPOLOGY

In this chapter, we present a new application of the gauge-invariant, quantized interband index $\Theta_{mn}$ that was introduced in the previous chapter. $\Theta_{mn}$ provides a bulk topological classification of a submanifold of parameter space, and therefore overcomes difficulties in characterizing multiband topology of submanifolds. In this chapter, we focus on submanifolds comprising electron valleys in the Brillouin zone. We confirm the topological nature of $\Theta_{mn}$ by numerically demonstrating a one-to-one correspondence to various Chern numbers in both $k \cdot p$ and lattice models. Furthermore, we derive a band-resolved topological charge $\Xi_{mn}$ and demonstrate that it can be used to investigate the nature of edge states due to band inversion in valley systems like multilayer graphene. Numerical methods are presented in Chapter 4.

The work in this chapter culminated in the publication of Ref. [38] as a Letter in *APS Physical Review B*, as an *Editor's Suggestion*. We acknowledge use of the material in Ref. [38] in this work.

## *2.1 Conventional Valley Chern Number and Limitations*

In the previous chapter, we mentioned that it was promising to explore $\Theta$ in the case of a $k$-space submanifold/loop containing a single high-symmetry point. We call these submanifolds containing high-symmetry points, which often correspond to the vicinity of band edges, *valleys*. In *valleytronics* (i.e., the study of physical phenomena at valleys), quasiparticles in 2-dimensional crystals with a periodic lattice structure may possess a valley degree of freedom at special points in the Brillouin zone (such as $K, \Gamma, M$, etc.), where the band energy gaps may be small (and potentially become zero and change the band topology). Systems used in valleytronics often possess time-reversal symmetry and have broken inversion symmetry [176]. Due to large momentum space $\mathbf{k}$ separation between valleys, inter-valley scattering tends to be suppressed, making the valley index a good quantum number. These valley degrees of freedom play key roles in future electronics and quantum

information science, as quasiparticles residing in the valleys may carry information much like charge and spin [34, 35, 52, 69, 71, 93–95, 110, 114, 127, 139, 140, 148, 153, 167, 177, 181, 185, 191, 192].

The topology of valleys is characterized by the *valley Chern number*. This number can be used to characterize several effects, such as valley Hall effects. These effects drive valley-polarized transverse currents that manifest as counterpropagating, valley-resolved edge states at sample boundaries. Valleytronics has recently received much interest as a result of theoretical and experimental advancements in several 2-dimensional material systems ranging from simple monolayer transition metal dichalcogenides to those demonstrating Moirè effects (as in multilayered graphene).

Generally, both $k \cdot p$ and lattice models have proven useful in the study of topological phenomena of valleys. $k \cdot p$ effective models often follow from low-energy expansions about a high-symmetry point or band extremum $P$, and can describe important band inversions leading to chiral edge states [60, 69, 71, 114, 127, 167, 185, 191, 192]. However, being subspaces of the complete Hilbert space, these models may not have a closed $k$-space manifold (e.g., 2-dimensional Brillouin torus). The conventional valley Chern number $\bar{\nu}^P$ is usually given by the $k$-space integral of the Berry curvature $F_m$ of filled bands in the vicinity of a valley centered at $P$, integrated to infinity:

$$\bar{\nu}^P = \sum_{i \in \text{filled}} \iint_{k \to \infty} F_i \equiv \sum_{i \in \text{filled}} \bar{C}_i^P. \tag{2.1}$$

Above, $\bar{C}_i^P$ is the valley Chern number at $P$ per band $|i\rangle$, and the overhead bars indicate that we used the conventional definition of (2.1) in contrast to the new definition that we will discuss subsequently. Topological quantities like $\bar{\nu}^P$ are only approximately quantized, unless the range of the integral in $k$ is truly infinite.

Lattice models (e.g., the Haldane model previously discussed; Section 4.2.1) describe quantum degrees of freedom confined to the sites of a discrete, periodic lattice with prescribed local hoppings or interactions, providing a minimal framework to capture collective phenomena and emergent phases in solids. Unlike with $k \cdot p$ models, in lattice models, there is no general quantized character to describe valley topology when the Berry curvature is not peaked at the valley; at least not without low-energy expansions or additional synthetic dimensions [41, 60]. This is because the Berry curvature is not necessarily highly localized at $P$, and the area of the valley available for integration is finite. Therefore, quantities like $\bar{\nu}^P$ cannot often be directly acquired from lattice

models. This is arguably inconvenient, because the physics at valleys can be significant even in lattice models, as we saw in Fig. 1.1 for the Haldane model.

It must be noted, however, that in some cases where the Berry phase is peaked in some submanifold around point $P$ (in both lattice and $k \cdot p$ models), one could use a finite $\mathbf{k}$-space integration of Berry curvature (similar to Eq. (2.1)), or a loop integral of the Berry connection:

$$\bar{\nu}^P = \sum_{i \in \text{filled}} \oint_{\partial \mathcal{M}_P} \mathcal{A}_i. \tag{2.2}$$

However, the above equation is arguably restrictive due to requiring a non-singular gauge.

An issue with the conventional valley Chern number is that, as just seen, there are arguably inconsistencies in its definition. In addition to the above, some references, such as [34], even define the valley Chern number as the difference between two $\bar{\nu}^P$ (as defined above in this section), whether calculated around two different valleys, or at the same valley but across a domain wall. To minimize ambiguity and generalize, we refer to this quantity as the *number of edge modes* $b$, which follows from the bulk-edge correspondence:

$$b = |T^\alpha - T^\beta|, \tag{2.3}$$

where $\alpha$ and $\beta$ indicate two systems and $T^\gamma$ is some topological character for context $\gamma$. For example, two adjacent Chern insulators with Chern number $C$ give: $b = |C^\alpha - C^\beta|$ [60]. Or, for a domain boundary between two valleys, we have [34, 140]:

$$b = |\nu^K - \nu^{K'}|. \tag{2.4}$$

The domain boundary above could be between 1D strips separating a $K$-edge from a $K'$-edge. Or within one Brillouin zone, when inter-valley scattering is suppressed [176]. Another example is that if the boundary is due to two bulk systems with different external potentials $U_1$ and $U_2$ at the same $P$, we get [140]:

$$b = |\nu^{P,U_1} - \nu^{P,U_2}|. \tag{2.5}$$

In Eq. (2.4) and Eq. (2.5) above, we did not use the overhead bar in anticipation of using our new definitions for the valley Chern number.

In summary, starting with inconsistent definitions, we find several issues with the conventional formalism for the valley Chern number. In $k \cdot p$ models, we usually only have approximate quantization even though the number of edge states is quantized. Even then, the **k**-space area of integration must be taken to infinity (which may be inconvenient both numerically and analytically). In lattice models, we do not have a general quantized character for valley topology without further model manipulations. In general, relating existing bulk indices to edge modes by the bulk-edge correspondence often requires summing the valley Chern number over all filled bands [176], and/or downfolding multiband Hamiltonians into simpler models [8, 104, 107]. This may cause a loss of information on the topological origin of edge states. For example, if the edge state arises from inverting a pair of bands among many bands, such band-resolved information would be missing in the valley Chern number description.

We found that we can use $\Theta$ to resolve all of the above issues.

## 2.2 *Correspondence between Interband Index $\Theta$ and Conventional Valley Chern Number*

### *2.2.1 $k \cdot p$ Models*

Using $\Theta$ instead of $\bar{\nu}^P$ Eq. (2.1) gives manifestly *quantized* integers using a *finite* loop about $P$. This property may be considered advantageous since we do not need an infinite area of integration. Indeed, the relation to topology becomes clear when we show that the interband index is twice the valley Chern number, i.e., $\Theta = 2\bar{\nu}^P$ in 2-band $k \cdot p$ models.

For illustration, consider the 2D gapped Dirac fermion model in Section 4.2.3. For a circular loop parameterized as $(k_x, k_y) = (r\cos(\lambda), r\sin(\lambda))$ and centered at the K' point (see Fig. 1.4 (left)), the first three integrals in Eq. (1.34) conspire to give quantized $\Theta$. The last term in Eq. (1.34) does not exist in 2-band models. As the area of integration approaches the limit $k \to \infty$, the third integral in Eq. (1.34) contributes less, making $\Theta$ the difference in integrals of $F_m$ and $F_n$. In the $k \to \infty$ limit, these two integrals are just $\bar{C}_m^K$ and $\bar{C}_n^K$ (Eq. (2.1)). We demonstrate this in Fig. 2.1, where we used $w = 3$, $\Delta = 1$, $\gamma = 1$ and $\alpha = 1$. See Section 4.2.3 for more on the model's Berry curvature.

To verify $\Theta = 2\bar{\nu}^{K'}$, consider the $k \to \infty$ limit. The Berry curvature sum rule $\sum_i F_i = 0$ gives $F_n = -F_m$ for 2-band models. Since $\bar{\nu}^{K'} = \iint F_n$ in this limit, the claim follows from Eq. (1.34) since the interband frequency integral tends to 0. Indeed, the figure shows $\iint F_n \to -1.5 = \bar{\nu}^{K'}$. With $\Theta = -3$, we verify $\Theta = 2\bar{\nu}^{K'}$.

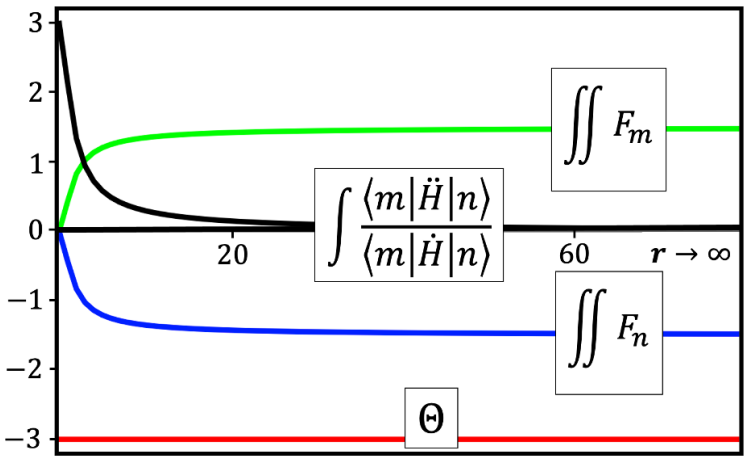


Figure 2.1: Berry curvature area integrals of upper and lower bands, integral of interband frequency, and the interband index in Eq. (1.34) as we vary the size of $k$ loops using $r = \sqrt{k_x^2 + k_y^2}$.

### *2.2.2 Lattice Models*

Next, we discuss $\Theta$ in lattice models. For demonstration, we use Haldane's 2-band model for the quantum anomalous Hall effect (Section 4.2.1). As discussed in Section 1.1.5, this model can give topologically nontrivial first Chern numbers that may yield topologically-protected edge states. The Chern number changes when the band gap closes and reopens at the high-symmetry points (K or K'), as shown in Fig. 1.1. The physics at these valleys is therefore significant, because their gap closings can change the topology, and therefore edge state physics. However, as discussed previously, unlike with the Dirac fermion model, it is not easy to define an analogous near-quantized topological quantity at valleys in lattice models.

However, $\Theta$ can again provide a quantized valley characterization using a small loop centered at $P$. Fig. 2.2 shows 'phase diagrams' analogous to Fig. 1.1 (a), but showing $\Theta$ for each valley. Clearly, when $\Theta^K$ and $\Theta^{K'}$ are summed at each phase space $(M/t_2, \phi)$ point in Fig. 2.2 (a) and (b),

we recover Haldane's phase diagram Fig. 2.2 (a): $\Theta^K + \Theta^{K'} = 2C$ [1]. Hence, compared to the state of the art, we now have a tool to analyze each valley in lattice models without using low-energy expansions.

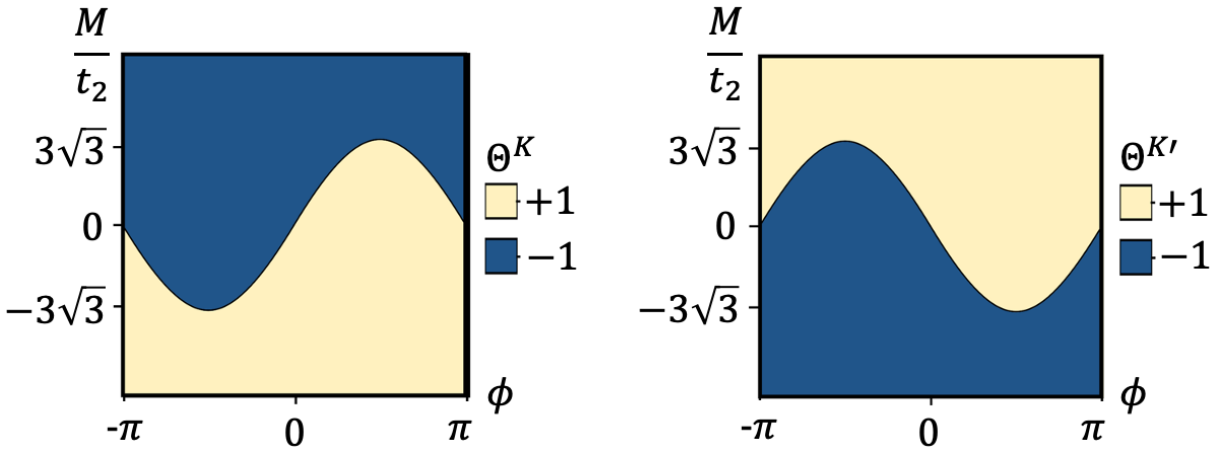


(a) (b)

Figure 2.2: (a) $\Theta^K(M/t_2, \phi)$ using a fixed $k$-space loop of radius 0.2 around the K point (b) $\Theta^{K'}(M/t_2, \phi)$. Notice that $\Theta^K(M/t_2, \phi) + \Theta^{K'}(M/t_2, \phi) = 2C(M/t_2, \phi)$, which is exactly twice the expected phase diagram for the first Chern number in Fig. 1.1 (a).

## *2.3 New Band-Resolved Topological Charge*

### *2.3.1 Motivation and Definition*

The connections between the interband index and local topological characteristics just seen motivate us to define a band-resolved topological charge $\Xi^P$ for each high-symmetry point $P$ that would add up to the Chern number $C$. For example, in the Haldane mode, we can define $\Xi^K + \Xi^{K'} \equiv \Theta^K/2 + \Theta^{K'}/2 = C$. This band-resolved topological charge can be generalized to valley and multiband problems. This allows us to not only calculate band-resolved and valley topological

[1] The factor of 2 is a peculiarity of 2-band models that arises from the Berry curvature sum rule $\sum_{i \in \text{all bands}} F_i = 0$, which guarantees us that the Berry curvature at each $k$-point of each band differs only by a sign. Therefore, the first two integrals in Eq. (1.34) simplify to a single integral with a factor of 2 (i.e., either $2\int_{\mathcal{M}} F_n$ or $-2\int_{\mathcal{M}} F_m$).

indices, but also to identify the number and source of edge states from inverting bulk bands without downfolding Hamiltonians.

To make this multiband functionality apparent, we use $\Theta_{mn}$ Eq. (1.33) to define the novel generalized band-resolved topological charge $\Xi_i^\gamma$ per band $|i\rangle$, of *context* $\gamma$ (e.g., $\gamma$ could be $P$, such as $K$). For an $N$-level Hamiltonian, the $N$ possible $\Xi_i^\gamma$ values may be found by solving the overdetermined simultaneous equations:

$$\{\Theta_{mn}^\gamma = \Xi_n^\gamma - \Xi_m^\gamma, \quad \sum_i \Xi_i^\gamma = 0\}. \tag{2.6}$$

We choose $N-1$ of the $N(N-1)/2$ equations involving $\Theta_{mn}^\gamma$ that make an appropriate linearly independent subset of equations along with $\sum_i \Xi_i^\gamma = 0$, which is a *conservation condition* that resolves linear dependence. This conservation condition is analogous to the Berry curvature sum rule Eq. (1.20): for a complete basis, the topological charges should sum to 0. Notice that since $\Theta_{mn}^\gamma$ is always an integer, it is reasonable to expect $\Xi_i^\gamma$ to be rational. Also note that, since $\Xi_i^\gamma$ exists for each band, we now have a topological character for each band (including unoccupied bands), and so now have a framework to aid in the study of excited state topology (which we exemplify in the next chapter). This is in addition to the conventional standard of considering sums of quantities over all filled bands.

Motivated by how $\bar{\nu}^P$ is a sum over filled bands (Eq. (2.1)), we define[2]:

$$\nu^\gamma = \sum_{i \in \text{filled}} \Xi_i^\gamma. \tag{2.7}$$

We numerically find that $\Xi_i^\gamma$ and $\nu^\gamma$ are sufficient to calculate the number of edge modes, without using conventional topological quantities such as the Chern number and valley Chern number. Our numerical results shown in the next section support these claims.

Before proceeding, we state that we can use this new $\nu^\gamma$ to calculate the number of edge modes $b$ Eq. (2.3). We can also use $\nu^\gamma$ to re-define existing topological indices. To use a specific example, consider a spinful system with only two $P$ $(K, K')$ for each spin label $(\uparrow, \downarrow)$. This could be the spinful

[2]Recall that we used an overhead bar $\bar{\nu}^P$ in Eq. (2.1) to denote conventional definitions. $\nu^\gamma$ in Eq. (2.7) lacks an overhead bar to differentiate our novel contribution, which is quantized as a rational number.

Dirac Hamiltonian on a monolayer honeycomb lattice (see Section 4.2.4). Then, per Ref. [34], the first, valley, spin, and spin-valley Chern numbers are respectively:

$$\begin{aligned} C &= \nu^{K,\uparrow} + \nu^{K',\uparrow} + \nu^{K,\downarrow} + \nu^{K',\downarrow} \\ V &= (\nu^{K,\uparrow} + \nu^{K,\downarrow}) - (\nu^{K',\uparrow} + \nu^{K',\downarrow}) \\ 2C_s &= (\nu^{K,\uparrow} + \nu^{K',\uparrow}) - (\nu^{K,\downarrow} + \nu^{K',\downarrow}) \\ 2C_{sv} &= (\nu^{K,\uparrow} + \nu^{K',\downarrow}) - (\nu^{K',\uparrow} + \nu^{K,\downarrow}). \end{aligned} \tag{2.8}$$

Under certain symmetries, the $\mathbb{Z}_2$ index for topological insulators $= C_s \pmod 2$ [34]. For all models tested[3], we recovered the expected topological quantities Eq. (2.8). For instance, we got the $N\pi$ Berry phases for the $N$-layer graphene models, and the $V$ in Ref. [192].

### *2.3.2 Models Tested*

We tested several models to successfully confirm the correspondence between the novel band-resolved topological charge $\Xi$ and existing topological quantities (such as various Chern numbers per $P$ and the ones in Eq. (2.8)). We tested the following $k \cdot p$ models: 2-band gapped Dirac fermion model [196]; 4-band gapped bilayer graphene model [192]; 4-band spinful Dirac Hamiltonian on monolayer honeycomb lattice [34]; 4-band ferrimagnetic honeycomb lattice model for the valley-polarized quantum anomalous Hall effect [199] (see also Ref. [131, 169, 200]); 6-band ABC-Stacked trilayer graphene [80]; 8-band gated bilayer graphene with Rashba spin-orbit coupling and exchange field [140]. We tested the following lattice models: Haldane model for the quantum anomalous Hall effect [56]; Qi-Wu-Zhang model [3]; 3-band generalized Haldane model on optical lattice [102]; and models allowing $|C| > 1$ such as the ones engineered in Ref. [159].

We demonstrate some of these results in the remainder of this section.

#### *$k \cdot p$ models*

We first exemplify the quantities we introduced using the **gapped Dirac fermion model** in Section 4.2.3. For the example discussed in Section 2.2.1 with $w = 3$, $\Delta = 1$, $\gamma = 1$ and $\alpha = 1$, we

[3] With the exception of Ref. [100], which remains an open problem.

use $\Theta = -3$ and solve the simultaneous equations $\{-3 = \Xi_n - \Xi_m, \Xi_n + \Xi_m = 0\}$ Eq. (2.6) to get $\Xi_n = -1.5$ and $\Xi_m = 1.5$, which is consistent with the conventional valley Chern number per band Eq. (2.1) $\bar{C}_n^K \approx -1.5$ and $\bar{C}_m^K \approx 1.5$; see Fig. 2.1.

The 4-band **gapped bilayer graphene model** (see Section 4.2.5) gives $\Xi^K = (\Xi_A, \Xi_B, \Xi_C, \Xi_D) = (0, -1, 1, 0)$ and $\Xi^{K'} = (0, 1, -1, 0)$ at valleys $K$ and $K'$ respectively. We set $\mu = 1, \Delta = 1, \gamma = 0.1$. For sanity, we see that the first Chern number $C = \Xi^K + \Xi^{K'} = (0, 0, 0, 0)$ is a expected due to the system's time-reversal symmetry. This is expected in the analysis in Ref. [192].

As another example, we see that the 6-band **model for ABC-stacked trilayer graphene** (see Section 4.2.6) gives $\Xi^K = (\Xi_A, \Xi_B, \Xi_C, \Xi_D, \Xi_E, \Xi_F) = (-1/2, 1/2, -3/2, 3/2, -1/2, 1/2)$ and $\Xi^{K'} = (1/2, -1/2, 3/2, -3/2, 1/2, -1/2)$ regardless of whether it is for a loop of radius $r = 0.001$, or $r = 5$. Again, we see that the first Chern number $C = \Xi^K + \Xi^{K'} = (0, 0, 0, 0)$ is a expected due to the system's time-reversal symmetry.

We may use $\Xi$ even in non-degenerate spinful systems[4]. For instance, we can use the low-energy expansion the **spinful Dirac Hamiltonian on a monolayer honeycomb lattice** in Ref. [34] (see Section 4.2.4) and consider the individual $2 \times 2$ blocks corresponding to each spin to recover the authors' results easily using $\Xi$. For the case $|m_z| < \lambda_{SO}$, we get $(\Xi_\uparrow^K, \Xi_\uparrow^{K'}, \Xi_\downarrow^K, \Xi_\downarrow^{K'}) = (1/2, 1/2, -1/2, -1/2)$ and using Eq. (2.8):

$$\begin{aligned} C &= \Xi_\uparrow^K + \Xi_\uparrow^{K'} + \Xi_\downarrow^K + \Xi_\downarrow^{K'} = 0 \\ V &= \Xi_\uparrow^K - \Xi_\uparrow^{K'} + \Xi_\downarrow^K - \Xi_\downarrow^{K'} = 0 \\ 2C_s &= \Xi_\uparrow^K + \Xi_\uparrow^{K'} - \Xi_\downarrow^K - \Xi_\downarrow^{K'} = 2 \\ 2C_{sv} &= \Xi_\uparrow^K - \Xi_\uparrow^{K'} - \Xi_\downarrow^K + \Xi_\downarrow^{K'} = 0, \end{aligned} \tag{2.9}$$

where $C_s$ and $C_{sv}$ are respectively the spin Chern number and spin-valley Chern number. Above, $\uparrow, \downarrow$ respectively correspond to spin-up and spin-down. Note that, under certain symmetries, the $\mathbb{Z}_2$ index for topological insulators $= C_s \pmod 2$ (Ref. [34]). We remark that an analysis that directly uses the $4 \times 4$ Hamiltonian does not coincide with the above analysis since the added off-diagonal couplings may make it different from the $2 \times 2$ block case just discussed.

[4] the study of degenerate systems is outside the scope of this work, although Ref. [180] presents a version of $\Theta$ for degenerate systems

We see that for these low-energy-expansion systems, we have a robust quantity $\Xi$ that appears to characterize the valley topology. We present more results for $k \cdot p$ models in Section 2.3.2 in the discussion of edge modes.

*Lattice models*

Our results hold even in the lattice models we tested.

For the **Haldane model** from Section 2.2.2, we simply get the same diagrams as in in Fig. 2.2, but with $\Xi^K = \Theta^K/2$ and $\Xi^{K'} = \Theta^{K'}/2$. Clearly, we then have $C = \Xi^K + \Xi^{K'}$ to match the phase diagram in Fig. 1.1 (a).

For another example, consider the topologically trivial $C = 0$ regimes $|u| > 2$ of the **Qi-Wu-Zhang model** with four valley points $X, X', M, \Gamma$ (see Section 4.2.7). Then, considering only the filled band,

$$C = \sum_{i \in \text{valleys}} \Xi^i = \Xi^X + \Xi^{X'} + \Xi^M + \Xi^\Gamma \tag{2.10}$$

gives us $C = 1/2+1/2-1/2-1/2 = 0$ for $u < 2$ and $C = -1/2-1/2+1/2+1/2 = 0$ for $u > 2$. For the nontrivial regime $-2 < u < 2$, we similarly get $|C| = 1$ (such as using $1/2+1/2-1/2+1/2 = +1$ for $u = -1$). We draw attention to how the Berry phase around each valley point is not peaked (as discussed previously in the context of lattice models). For instance, for $u = -1$ and a loop of $r = 0.3$, we have the Berry curvature integral within it as $\approx (0.02, 0.02, -0.002, 0.02) \times 2\pi$ to one significant figure.

We also verified our results using the **generalized 3-band Haldane model on an optical lattice** (see Section 4.2.8). Our findings are presented in Fig. 2.3. This example shows that electron-hole symmetry is not necessary for our conclusions to hold, since this model inherently lacks electron-hole symmetry.

*Number of edge states*

We now demonstrate how the relationships between $\Xi_i$ and bulk topological invariants just discussed allow us to count edge states without downfolding a multiband Hamiltonian into fewer-band ones. Context matters in this application, as one must have an appropriate problem (such as a domain wall) in terms of a $\boldsymbol{k}$-space Hamiltonian $H(\mathbf{k})$. Then, a Hamiltonian parameter (such as valley,

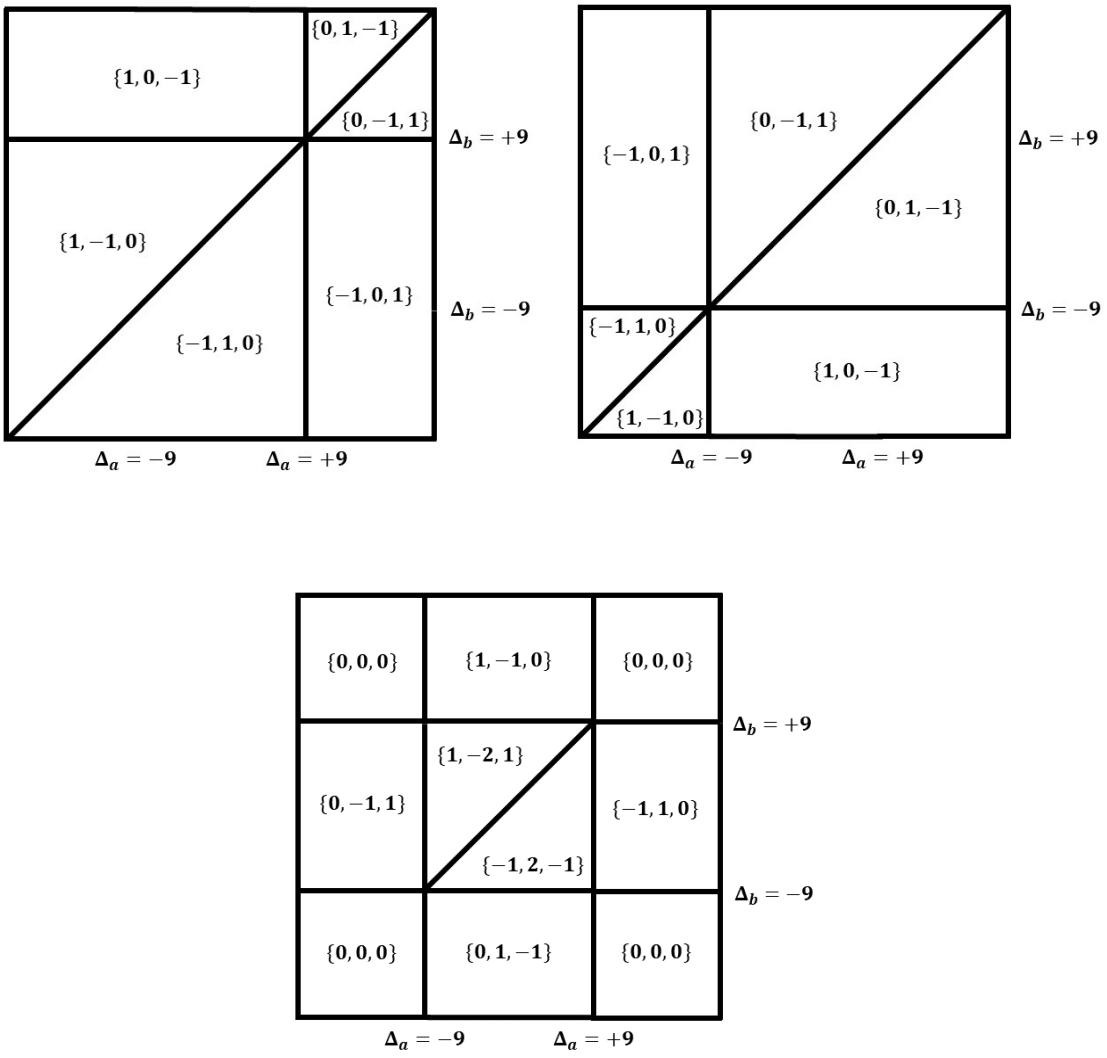


Figure 2.3: We recover the phase diagram in Ref. [102] (see Section 4.2.8) for the first Chern number $C$ per level by calculating $\Xi^K$ (top left) and $\Xi^{K'}$ (top right). To replicate the authors' results, we recover the Chern number per level $\{C_A, C_B, C_C\}$ using $C = \Xi^K + \Xi^{K'}$ at each $(\Delta_a, \Delta_b)$. However, we achieve this without relying on the gauge-dependent Berry connection the way the authors did. Notice that this calculation differs from other examples because we consider the Chern number of each band (see Eq. (2.1)), as opposed to the sum of filled bands.

electric/magnetic field or stacking order) may be used to define two different domains in order to calculate the number of edge modes Eq. (2.3) $b = |T^\alpha - T^\beta|$.

For instance, for the 4-band **gapped bilayer graphene model** (see Section 4.2.5), a change in sublattice registry from AB ($\mu = 1$) to BA ($\mu = -1$) stacking may make $(\Xi_A, \Xi_B, \Xi_C, \Xi_D)$ change from $(0, -1, 1, 0) \to (0, 1, -1, 0)$ at the K point. Since $|A\rangle, |B\rangle$ are the filled states, we have $\nu^{\mu=1} = \Xi_A^{\mu=1} + \Xi_B^{\mu=1} = 0 + (-1) = -1$ and $\nu^{\mu=-1} = 0 + 1 = 1$, which gives $b = |\nu^{\mu=1} - \nu^{\mu=-1}| = |(-1) - (1)| = 2$. This number of edge modes is consistent with the authors' work.

As another example, consider the 6-band model for **ABC-stacked trilayer graphene** (see Section 4.2.6), which has Fermi level between states $|C\rangle$ and $|D\rangle$. For a loop of radius 1, the Berry curvature integrals of each valence band for first case of valley $K$ (which has the same results as the case of bias potentials $(U_1, U_2, U_3) = (-0.2, 0, 0.2)$ at valley K) are $\approx (0.087, 0.49, -2.1) \times 2\pi$, and

$$(\Xi_A, \Xi_B, \Xi_C, \Xi_D, \Xi_E, \Xi_F) = (-1/2, 1/2, -3/2, 3/2, -1/2, 1/2). \tag{2.11}$$

For the second case of valley K' (and also of bias potentials $(U_1, U_2, U_3) = (0.2, 0, -0.2)$ at valley K), we have $\approx (-0.087, -0.49, 2.1) \times 2\pi$ and

$$(\Xi_A, \Xi_B, \Xi_C, \Xi_D, \Xi_E, \Xi_F) = (1/2, -1/2, 3/2, -3/2, 1/2, -1/2). \tag{2.12}$$

Then, the valley Chern number $\nu = -3/2$ in the first case and $\nu = 3/2$ in the second. This gives $b = |3/2 - (-3/2)| = 3$ as the number of edge modes, both when considering a domain boundary between K and K'; and a domain boundary separating two regions of the bias potentials whose values are given above. Note that $\Xi_i$ aren't the exact apparent limits of the Berry curvature (example: the Berry curvature of band $|A\rangle$ seems to tend to 0 whereas $|\Xi_A| = 1/2$). However, if we sum the Berry curvatures of filled bands, we get $|\pm 1.5 \times 2\pi| = 3\pi$ in both cases, as is expected for ABC-stacked trilayer graphene.

Finally, consider the 8-band model for **gated bilayer graphene with Rashba spin-orbit coupling and exchange field** (see Section 4.2.9). As the spin-orbit coupling parameter is tuned from $\lambda_R = 0.2t$ to $0.4t$, we expect a band inversion at the $K$ valley, as in Fig. 2.4 (a). For these two values of $\lambda_R$, we present $\Xi_i$ in Table 2.1. We map the $\Xi_i^{\lambda_R}$ in Table 2.1 to existing

topological quantities: First, we see that for each choice of $\lambda_R$, $C = \nu^K + \nu^{K'} = 0$, due to $\Xi_i^{\lambda_R,K} = -\Xi_i^{\lambda_R,K'}$. This is consistent with the time-reversal symmetry of the model. We note, as we've seen before, that the limit of each $\bar{C}_i^P$ may not tend to the quantized $\Xi_i$ in $N$-band models with $N > 2$. To see this, we calculated $\bar{C}_i^P$ at valley $K$ in the $k \to \infty$ limit using Eq. (2.1). For $\lambda_R = 0.2t$, $(\bar{C}_A^K, \bar{C}_B^K, \bar{C}_C^K, \bar{C}_D^K, ...) \approx (-0.01, 0.99, -1.99, -0.99, ...)$. We see that $\bar{C}_A \approx -0.01 \to 0$, which is different from $\Xi_A = -1/2$. This mismatch arises from the last two correction terms in Eq. (1.34), which do not necessarily tend to 0 in models with $N > 2$ bands. However, again, a difference between indices may indicate the number of edge states. Consider a valley problem with a domain boundary between $K$ and $K'$ for fixed $\lambda_R$ at half-filling. From Table 2.1, we have $b = |\nu^K - \nu^{K'}| = |-1-1| = 2$ for $\lambda_R = 0.4t$, and $b = |-2-2| = 4$ for $\lambda_R = 0.2t$. If we instead take a domain boundary problem at $K$ for the two $\lambda_R$ values, we get $b = |\nu^{0.4} - \nu^{0.2}| = |-1-(-2)| = 1$ as the number of edge modes due to the band inversion. These results are consistent with Ref. [140].

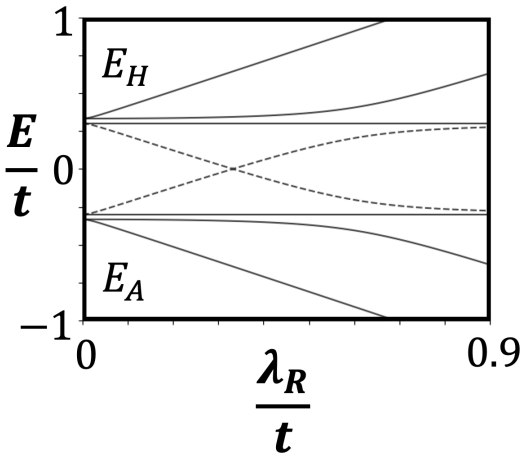


(a)

Figure 2.4: Band diagram at the $K$ point $(k_x, k_y) = (0, 0)$ for the 8-band bilayer graphene model. At $\lambda_R = 0.2\,t$, the bands are labeled $E_A, E_B, \ldots, E_H$ as we go from $-1$ to $+1$ along the vertical axis. As $\lambda_R$ is varied from $0.2\,t$ to $0.4\,t$, the bands $E_D$ and $E_E$ invert at $\lambda_R \approx 0.33\,t$.

| | $\Xi_A$ | $\Xi_B$ | $\Xi_C$ | $\Xi_D$ | $\Xi_E$ | $\Xi_F$ | $\Xi_G$ | $\Xi_H$ |
|---|---|---|---|---|---|---|---|---|
| $\Xi_i^{0.4}$ | $-\frac{1}{2}$ | $\frac{1}{2}$ | $-\frac{3}{2}$ | $\frac{1}{2}$ | $-\frac{1}{2}$ | $\frac{3}{2}$ | $-\frac{1}{2}$ | $\frac{1}{2}$ |
| $\Xi_i^{0.2}$ | $-\frac{1}{2}$ | $\frac{1}{2}$ | $-\frac{3}{2}$ | $-\frac{1}{2}$ | $\frac{1}{2}$ | $\frac{3}{2}$ | $-\frac{1}{2}$ | $\frac{1}{2}$ |

Table 2.1: $\Xi_i^{\lambda_R}$ for the $K$ valley of the 8-band model for gated bilayer graphene. At $K'$, $\Xi_i^{\lambda_R,K'} = -\Xi_i^{\lambda_R,K}$.

*Sources of edge states*

In the previous subsection we saw that $\Xi$ could be used to determine the number of edge states using existing bulk topological invariants. Now, we use $\Xi$ to identify the sources of these edge modes (e.g., which orbitals the edge states are from if an orbital basis is used). We claim that there is a correspondence between $\Xi$ values that change, and band ordering. With this observation, we can identify the bulk bands and orbitals causing edge states in lieu of the standard techniques. The standard techniques used to identify the two bands swapped involves either tracking the energy dispersion at the band crossing point with respect to the external parameter (e.g., as in Fig. 2.4), or by inspecting the wavefunction density in the vicinity of the band crossing.

To clarify the procedure, consider a system with bands $A, B, ...N$, and a context $\alpha$ (e.g., valley K, or potential $U$) with a set of $\Xi_i^\alpha$ : $(\Xi_A^\alpha, \Xi_B^\alpha, ..., \Xi_N^\alpha)$, and a different context $\beta$ with $\Xi_i^\beta$ : $(\Xi_A^\beta, \Xi_B^\beta, ..., \Xi_N^\beta)$. We numerically verified that if only two bands touch/invert and represent an edge state, all $\Xi_i^\gamma$ will be the same between the two contexts, except for two from each context which correspond to the bands that invert.

For example, in the 8-band model just discussed (i.e., **gated bilayer graphene with Rashba spin-orbit coupling and exchange field**; Section 4.2.9), Table 2.1 shows that the only indices that differ between $\lambda_R = 0.4t$ and $\lambda_R = 0.2t$ are $\Xi_D$ and $\Xi_E$ (which respectively correspond to bands $E_D$ and $E_E$). From Fig. 2.4, we confirm that the orbitals causing edge states are indeed from bands $E_D$ and $E_E$.

To verify that the edge states are indeed from bands $E_D$ and $E_E$, we used *Kwant* [53] to model a tight-binding nanoribbon of 120 sites that is periodic in the $y$-direction, that has a domain boundary in the $x$-direction at site $i = 60$, as in Fig. 2.5 (a) (top). We discretized the continuum model

Eq. (4.30) to get a tight-binding model that includes both valleys. Our calculations [53] show that edge states accumulate at the domain boundary. We then calculated the nanoribbon bands in Fig. 2.5 (a) (bottom), which shows one zero-energy edge state from each valley. Fig. 2.5 (b) shows that these edge states are composed of orbitals from $E_D$ and $E_E$, evident from the large overlap between the zero-energy edge state wavefunction $|\phi\rangle$ and the bulk wavefunctions $|\psi\rangle$ of $E_D$ and $E_E$ (calculated in a homogeneous nanoribbon at $\lambda_R = 0.2t$).

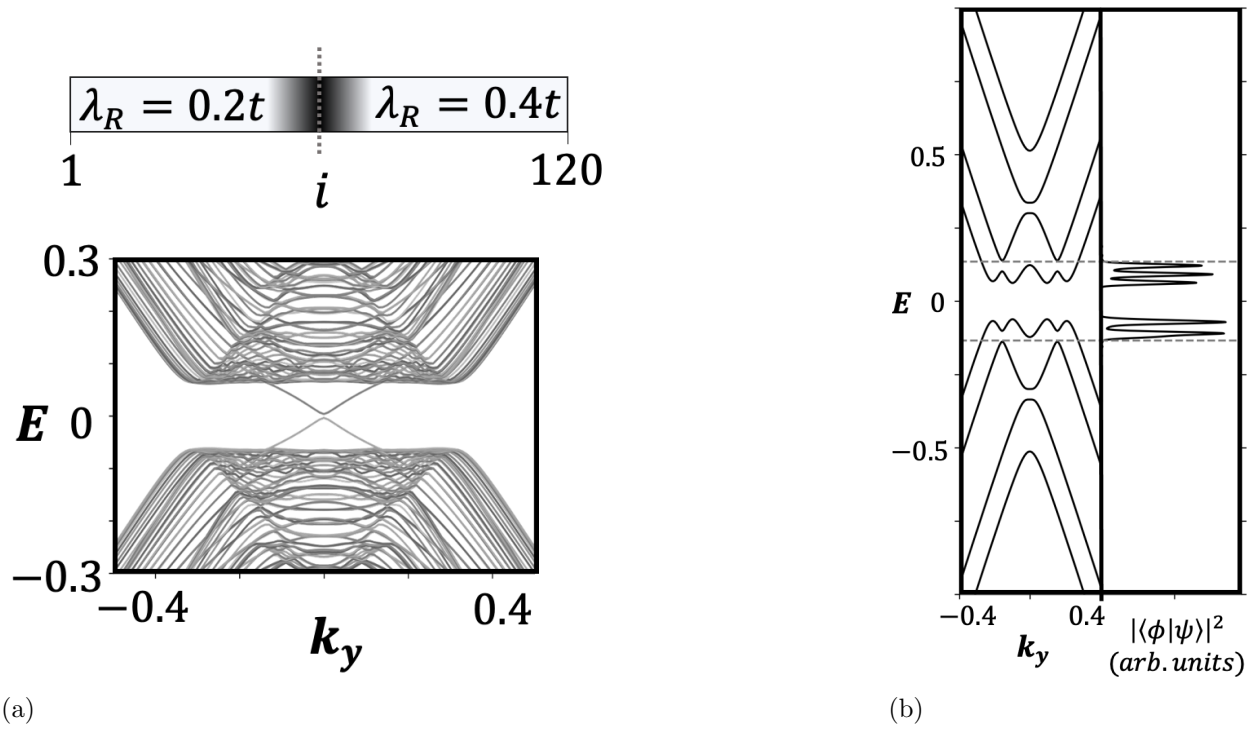


Figure 2.5: Verifying sources of edge states in 8-band bilayer graphene model. (a) *Top:* Schematic of real-space nanoribbon with a domain boundary in the $x$-direction separating regions of two different $\lambda_R$. The shaded area represents the calculated wavefunction density. *Bottom:* Nanoribbon bands at $k_x = 0$ along the $k_y$ direction. (b) *Left:* Bulk bands at $k_x = 0$ for $\lambda_R = 0.2\,t$. *Right:* Gaussian-broadened overlap element between bulk and domain boundary band wavefunctions $|\langle\phi|\psi\rangle|^2$.

From the discussion above, we confirm that the novel band-resolved topological charge $\Xi$ may be used to count, and identify the sources, of edge states.

*Identifying band reordering using* $\Theta$

Before moving on, we also state that we empirically discovered an algorithm that uses $\Theta$ (instead of $\Xi$) to identify band reorderings.

Consider a fixed $\boldsymbol{k}$-space loop that is traversed twice adiabatically using $H(\boldsymbol{k}, \alpha_1)$ and $H(\boldsymbol{k}, \alpha_2)$ separately, where the Hamiltonian $H$'s external parameters $\alpha_i$ have the potential to change the energy band ordering. This is regardless of whether the band reordering is topologically non-trivial or not. We claim that all the interband indices $\Theta^{mn}$ (superscript now indicating that the indices correspond to bands $|m\rangle$ and $|n\rangle$) can be used to uniquely identify the bands that swapped positions (or inverted) using our algorithm and example in Figure 2.6.

As another example, we consider the **gated bilayer graphene with Rashba spin-orbit coupling and exchange field** (see Section 4.2.9). To cross-check against the band inversion demonstrated in Fig. 2 of the model's source in Ref. [140], occurring for $\lambda_R \approx 0.33t$ we calculate the interband indices ($\Theta^{21}, \Theta^{31}, \Theta^{32}, \Theta^{41}, \Theta^{42}, \Theta^{43}, \Theta^{51}, \Theta^{52}, \Theta^{53}, \Theta^{54}, \Theta^{61}, \Theta^{62}, \Theta^{63}, \Theta^{64}, \Theta^{65}, \Theta^{71}, \Theta^{72}, \Theta^{73}$, $\Theta^{74}, \Theta^{75}, \Theta^{76}, \Theta^{81}, \Theta^{82}, \Theta^{83}, \Theta^{84}, \Theta^{85}, \Theta^{86}, \Theta^{87}$), using the same band labeling convention as the authors: $E_1 < E_2 < E_3 < E_4 < E_5 < E_6 < E_7 < E_8$. With $M = 0, U = 0.3t$ and $t_\perp = 0.143t$, for $H(\lambda_R = 0.2)$ we get $\Theta_i = (-1, 1, 2, 0, 1, -1, -1, 0, -2, -1, -2, -1, -3, -2, -1, 0, 1, -1, 0, 1, 2, -1, 0,$ $-2, -1, -0, 1, -1)$, and for $H(\lambda_R = 0.4)$ we get $\Theta_f = (-1, 1, 2, -1, 0, -2, 0, 1, -1, 1, -2, -1, -3, -1,$ $-2, 0, 1, -1, 1, 0, 2, -1, 0, -2, 0, -1, 1, -1)$. Then, our algorithm correctly identifies that the correct band swap was $|4\rangle \leftrightarrow |5\rangle$.

The $\Theta_i$ and $\Theta_f$ in Figure 2.6 are for a loop enclosing the valley $K$. However, for a similar loop enclosing $K'$, we see that $\Theta_i = (1, -1, -2) = \Theta_f$ for both $\Delta_b = 6$ and $\Delta_b = 10$ (implying no band swap in this region). This highlights the role of $\Theta$ as a descriptor of only the chosen submanifold. It also stresses the importance of an appropriate setup/experiment: Since the gap closing occurs only at $K$ for chosen $\Delta_b$, $\Theta$ for $K'$ cannot reveal the band reordering that occurred elsewhere. $\Theta$ also may not be used to identify avoided crossings within the same band. For instance, consider a 3-band model with bands labeled $|A\rangle, |B\rangle, |C\rangle$ (with eigenvalues $E_A < E_B < E_C$). Even if it is known that $A, B$ are inverted only in the vicinity of a $\Gamma$ point but not inverted elsewhere in $\boldsymbol{k}$-space, $\Theta^{BA}$ will be the same in all regions of $\boldsymbol{k}$-space, unless the bands switch orders (i.e. to $E_B < E_A < E_C$, or $E_A < E_C < E_B$, etc). This is a consequence of the algorithm requiring both a

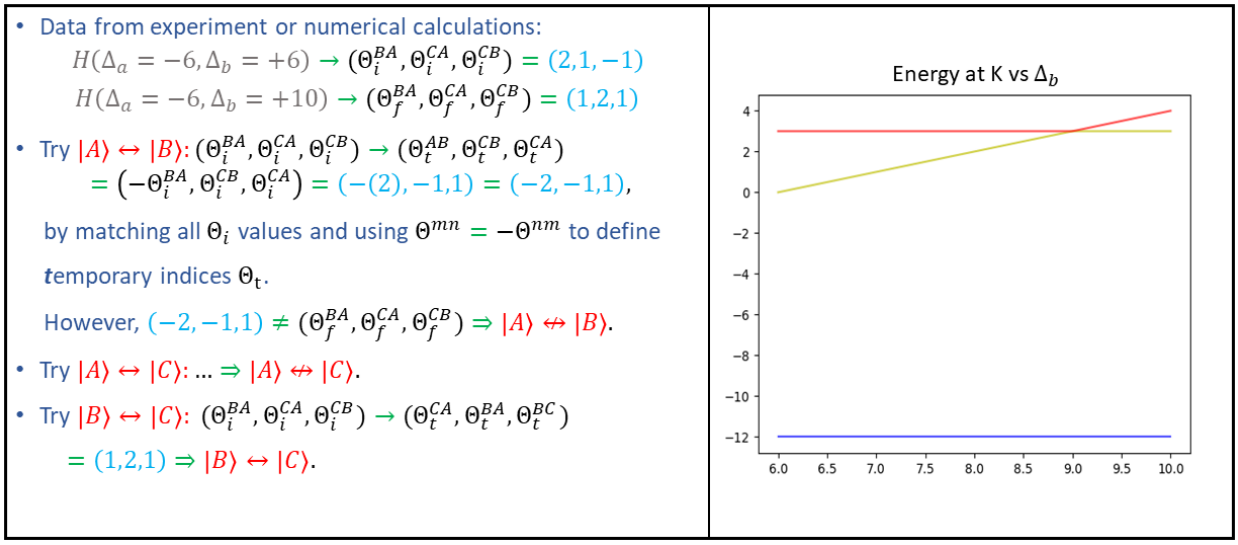


Figure 2.6: Algorithm for detecting band reordering, introduced by example. We consider the 3-band generalized Haldane model on optical lattices with bands labeled $|A\rangle, |B\rangle, |C\rangle$ (eigenvalues initially labeled $E_A < E_B < E_C$ when $H(\Delta_a = -6, \Delta_b = 6)$). Then, we consider a loop of radius 0.3 centered at the $K$ point $(4\pi/3\sqrt{3}, 0)$ and calculate the initial interband indices $\Theta_i^{mn}$ and final indices $\Theta_f^{mn}$, respectively for $H(\Delta_a = -6, \Delta_b = 6) \rightarrow H(\Delta_a = -6, \Delta_b = 10)$. This results in a reordering between bands $|B\rangle \leftrightarrow |C\rangle$, as confirmed by the figure on the right. The algorithm on the left considers only non-identity mappings $|m\rangle \not\rightarrow |m\rangle$, and may take only a few seconds to run using an appropriate program. The rule $\Theta^{mn} = -\Theta^{nm}$ is demonstrated in Section 1.3.2. As shown, our algorithm correctly identifies the swapped bands.

$\Theta_i$ and a $\Theta_f$.

To the best of our knowledge, this algorithm correctly and uniquely identifies the band pair swapped as long as: the bands in the 'initial' and 'final' configurations are fully gapped inside and on the loop; and that the $\boldsymbol{k}$-space loop chosen encloses only one high-symmetry point. If there are several potential band crossings, the result may be ambiguous. For example, in the 3-band model example above with bands $|A\rangle, |B\rangle, |C\rangle$, consider a loop that does not enclose a valley point, where $(\Theta^{BA}, \Theta^{CA}, \Theta^{CB})$ from $(-1, +1, -1) \rightarrow (+1, -1, +1)$ after some external parameter change. Then, our algorithm accurately identifies that all three possible band swaps are valid (i.e. $|B\rangle \leftrightarrow |A\rangle, |C\rangle \leftrightarrow |A\rangle, |C\rangle \leftrightarrow |B\rangle$). On the other hand, it is also possible that no valid band swaps will be identified. This may happen if the bands are not fully gapped, or if the indices calculated are from a complicated, non-bijective-mapping case potentially involving several variables (such as $H(\boldsymbol{k}, \alpha_1, \beta_1) \rightarrow H(\boldsymbol{k}, \alpha_2, \beta_2)$). Such cases often correspond to when the absolute values of the elements of the unordered sets are different: $|\Theta_i^{mn}| - |\Theta_f^{mn}| \neq 0$.

Also consider the 4-band **gapped bilayer graphene model** (see Section 4.2.5). Changing the sign of parameter $\mu$ indicates a transition from AB to BA interlayer registry. As the authors of that model's source Ref. [192] demonstrate, this transition is accompanied by and comes with propagating chiral boundary modes. At valley $K$, for $H(\mu = -1)$, we have $(\Theta^{21}, \Theta^{31}, \Theta^{32}, \Theta^{41}, \Theta^{42}, \Theta^{43}) = (-1, 1, 2, 0, 1, -1)$ while $H(\mu = +1)$ gives us $= (1, -1, -2, 0, -1, +1)$. Then, our algorithm correctly identifies that the second and third bands invert (and result in edge states). But unlike their work, we were able to deduce this without simplifying the Hamiltonian further into a 2-band model.

Unlike existing methods of detecting band reordering, we are now able to acquire the same information in a quantifiable, and arguably more-elegant manner that can be applied in broader generality to any $N$-band system using orthogonal instantaneous energy eigenstates.

### *2.4 Chapter Summary*

In this chapter, we introduced a novel quantized topological interband index $\Theta_{mn}$ Eq. (1.34) that characterizes the multiband topology of a submanifold of 2-dimensional parameter space. This is in contrast to the conventional theoretical framework that uses the entire parameter space in lattice models, and an infinite parameter space in $k \cdot p$ models. This is also in contrast to how

conventional methods sum quantities over all filled bands, as opposed to giving a quantity that explicitly characterizes the topology of a pair of bands (including unoccupied bands; thereby allowing for the study of excited state topology). We introduced a complementary interband frequency Eq. (1.33) which gives further insight into the behavior $\Theta_{mn}$. We applied $\Theta_{mn}$ to the context of valley topology and introduced a novel band-resolved topological charge $\Xi_{mn}$. This quantity, compared to the conventional method of summing topological quantities over all filled bands only, additionally gives a perfectly quantized topological character for each band (including unoccupied bands). To highlight its topological nature, we mapped $\Xi_{mn}$ to existing standard topological quantities (such as various Chern numbers), but now with the added advantages of being able to do so without downfolding multiband Hamiltonians to simpler models and without necessarily having to sum quantities over filled levels. We thereby preserve information on the origin of edge states, while verifying the number of edge modes is as expected. In $k \cdot p$ models, we are now able to use a finite $\boldsymbol{k}$-space integration which yields a perfectly quantized number (as opposed to an infinite integration yielding approximate quantization). And in lattice models, we are able to define a valley character even if the Berry curvature is not peaked at the valley. Overall, we claim that $\Theta_{mn}$ and $\Xi_{mn}$ offer a new theoretical framework that arguably improves the classification of submanifold topology.

The work in this chapter culminated in the publication of Ref. [38] as a Letter in *APS Physical Review B*, as an *Editor's Suggestion*. In the next chapter, we introduce another application of the interband index, now in the context of optical selection rules for excitons.

Chapter 3

# APPLICATION II: EXCITON SELECTION RULES

In the previous chapter, we presented an application of the novel interband index $\Theta_{mn}$ Eq. (1.33) in the context of valley topology. We now present a second application of the interband index in a very different context, of exciton selection rules. Presently, the optical selection rules for excitons under circularly-polarized light are manifestly gauge-dependent. The interband index $\Theta_{mn}$ may improve the topological classification of material excited states because it is intrinsically an inter-level quantity. In this chapter, we expand on this index to introduce its chiral formulation, and use it to make the selection rules gauge-invariant. We anticipate this development to strengthen the theory of quantum materials, especially two-dimensional semiconductor photophysics. Numerical methods are presented in Chapter 4.

The contents of this chapter culminated in the publication Ref. [36] in *Physica B: Condensed Matter* by *Elsevier*. We acknowledge use of this reference in this work.

## *3.1 Background and Motivation*

Excitons in semiconductors are excited states with electron-hole pairs bound by mutual Coulomb interactions [26, 172]. Their ability to mediate light-matter interactions allows them to play significant roles in phenomena such as optoelectronic, spintronic, and valleytronic properties in a wide array of material systems at the forefront of contemporary condensed matter research, particularly 2-dimensional semiconductors [25, 78, 89, 111, 115, 142, 152, 178, 187]. Example systems include materials such as hexagonal boron nitride (hBN) [27, 46, 81, 135], transition-metal dichalcogenides (TMDs) [47, 54, 128, 141, 166], gapped graphene systems [21, 70, 134, 196], and 2-dimensional photonic devices such as light-emitting diodes (LEDs) and lasers [178]. Excitonic effects can have a significant influence on the optical response of solids [1, 6, 91, 129, 147], which can provide valuable information about material properties such as band structure [14, 188], and act as a sensor for

probing charge ordering and quantum phases [23] (e.g., Mott insulators in twisted bilayer moiré superlattices [182], and fractional quantum Hall states in twisted bilayer $MoTe_2$ [18]). Excitons therefore offer a lucrative platform to study fundamental quantum phenomena, along with applications in tunable materials devices such as future excitonic-carrier devices in quantum computation and excitonic circuits [178]. Therefore, it is important to have a unified theoretical framework to determine excitonic properties, which can offer important insights for experiments and device applications. A crucial step in predicting the excitonic response is determining whether a bright or dark exciton is formed in response to light. This is determined by the optical selection rules for excitons.

The original *optical selection rules for excitons* [32] can be explained by the hydrogen model, since the constituent electron-hole pairs form hydrogen-like bound states [26,172]. For conventional semiconductors, these rules would state that in dipole-allowed materials like TMDs, s-like excitons are optically active, while p-like excitons are optically inactive; and that in dipole-forbidden materials, the optically active excitons are p-like states, while s-like states are optically inactive [21]. However, it was recently shown that for 2-dimensional systems, the states near the band edge may be of multiple orbital and spin components, and the bands can have nontrivial topological characteristics arising from band topology (including Berry phase effects) [21, 176, 196]. This nontrivial topology was accounted for by Refs. [21, 196] when they proposed new optical selection rules for excitons under circularly polarized light. These modified rules build on the fact that the optical response of excitons depends on the oscillator strength (which relies on the exciton envelope function), and the interband velocity matrix element characterized by angular momentum. Then, whether a bright or dark exciton shows for a given angular momentum is governed by the selection rule:

$$m = -l_{\mp} \pmod{n}, \tag{3.1}$$

where $n$ is from the system's discrete $n$-fold rotational symmetry, $m$ is the angular momentum quantum number, and $l_{\pm}$ is the winding number of the interband dipole matrix element $\langle m \,|\, \hat{p} \,|\, n \rangle \cdot \hat{e}_{\pm}$ in left $(+)$ and right $(-)$ circular polarization, where $\hat{p}$ is the momentum operator and $\hat{e}_{\pm} = \frac{1}{\sqrt{2}}(\hat{e}_{k_x} \pm i\hat{e}_{k_y})$ are the chiral unit vectors, for unit vectors $\hat{e}_{k_x}$ and $\hat{e}_{k_y}$ in momentum space $\boldsymbol{k} = (k_x, k_y)$. These new selection rules Eq. (3.1) have since been experimentally verified (e.g., in Ref. [70]), and are

key to understanding the photophysics of semiconductors.

Yet, despite their success, these modified selection rules may arguably be considered incomplete from a theoretical standpoint due to their inherent gauge-dependence, which arises from requiring a hydrogenic gauge that doesn't allow singularities at the band edge [21,196]. This gauge-dependence might impose limitations on the scope of theoretical calculations involving the selection rules, and therefore impact the potential to verify experiment and propose new physical applications. We address this issue in this work by making the selection rules gauge-invariant. We do this using the interband index $\Theta_{mn}$ Eq. (1.33) from the previous chapters. We will denote this $\Theta_{mn}$ as $\Theta_k$ in this chapter to indicate the tangential vector dependence, to prevent confusion with the interband index's chiral formulation $\Theta_\pm$ Eq. (3.2) that we will introduce. We use $\Theta_\pm$ to make the selection rules Eq. (3.1) into gauge-invariant selection rules Eq. (3.4). This gauge-invariance may strengthen the theory of excitonic optical selection rules, thereby making associated phenomenology more accessible for both theoretical and experimental work.

## *3.2 Gauge-Invariant Optical Selection Rules for Excitons*

### *3.2.1 Chiral formulation of interband index $\Theta_\pm$*

As just mentioned, we make the selection rules gauge-invariant using a new chiral version of the original interband index $\Theta_k$. The $k$-dependent form of $\Theta_k$ in Eq. (1.33) makes it clear that the tangential vector $\hat{e}_\tau$ may be replaced by an appropriate vector that preserves a winding property of the matrix element $\langle m \,|\, \boldsymbol{\nabla_k} H \,|\, n \rangle$. Therefore, we introduce another physically-useful formulation of the interband index in terms of the chiral unit vectors $\hat{e}_\pm$ (see Fig. 1.4, right):

$$2\pi\Theta_\pm = \Delta\Phi - \oint_{\partial\mathcal{M}} \mathrm{d}\arg \frac{\langle m \,|\, \boldsymbol{\nabla_k} H \,|\, n \rangle}{E_{nm}} \cdot \hat{e}_\pm, \tag{3.2}$$

where

$$\hat{e}_\pm = \frac{1}{\sqrt{2}}\big(\hat{e}_x \pm i\hat{e}_y\big). \tag{3.3}$$

All the terms in the definitions of the interband index work together to give a quantized, gauge-invariant quantity.

### *3.2.2 New gauge-invariant optical selection rules*

The chiral unit vectors $\hat{e}_\pm$ are known to decompose the interband matrix element $\langle m\,|\,\hat{p}\,|\,n\rangle$ into chiral components $\langle m\,|\,\hat{p}\,|\,n\rangle \cdot \hat{e}_+$ and $\langle m\,|\,\hat{p}\,|\,n\rangle \cdot \hat{e}_-$. These may respectively correspond to left- and right-circularly polarized photon modes ($\sigma_-$ and $\sigma_+$) [21]. This means that the complex-valued $\langle m\,|\,\hat{p}\,|\,n\rangle \cdot \hat{e}_\pm$ yield two unique vector fields with possibly different winding patterns over $k$-space. Since $\hat{p}$ is the $k$-space derivative of the Hamiltonian, we observe that the winding number of $\langle m\,|\,\hat{p}\,|\,n\rangle \cdot \hat{e}_\pm$ is simply the interband line integral in our chiral formulation of the interband index Eq. (3.2). Therefore, we rid the optical selection rules Eq. (3.1) of their explicit gauge-dependence by rewriting them as:

$$m = -\Theta_\mp \pmod{n}. \tag{3.4}$$

One could argue that the above selection rule Eq. (3.4) strengthens the theory of excitons due to explicit gauge-invariance.

### *3.2.3 Verifying new selection rules*

We computationally verified Eq. (3.4) by calculating $\Theta_\pm$ (and $m$) for the biased bilayer graphene model in Section 4.2.10, which we present here again:

$$H = \begin{pmatrix} \Delta & \alpha k_+^2 \\ \alpha k_-^2 & -\Delta \end{pmatrix} + 3\gamma_3 \begin{pmatrix} 0 & k_- \\ k_+ & 0 \end{pmatrix}, \tag{3.5}$$

where $k_\pm = k_x \pm i k_y$, $\gamma_3$ is the interlayer hopping amplitude, $2\Delta$ is the energy gap, and we set the factor $\alpha = 1$.

Without the interlayer hopping term (i.e. $\gamma_3 = 0$), the biased bilayer graphene system has $C_\infty$ symmetry and yielded $\Theta_+ = -3$ and $\Theta_- = -1$ (i.e. $m = 3$ and $m = 1$ from Eq. (3.4)), as expected in Ref. [196]. Non-zero $\gamma_3$ reduces $C_\infty$ to $C_3$ and should give $m = -2, 0, 1, 3 = 0, 1 \pmod 3$. Using $\gamma_3 = 0.3$, we got $\Theta_+ = 0$ and $\Theta_- = -1$ (i.e. $m = 0$ and $m = 1$), as expected. However, we caution against using this reasoning to determine which excitons show, without first calculating the oscillator strength explicitly. This is because the mapping involving $\Theta_\pm$ may be many-to-one, while the full calculation might specify a many-to-many relation in the sense that different $m$ may

result from the same $\Theta_{\pm}$ (as we saw when mapping $m = -2, 0, 1, 3 \to 0, 1$).

### *3.3 Chapter Summary*

We showed how the interband index $\Theta_{\pm}$ Eq. (3.2) may be used to make the gauge-dependent optical selection rules for excitons Eq. (3.1) gauge-invariant Eq. (3.4). This gauge-invariance may broaden the scope of the types of theoretical calculations that may be done, since we now do not need to fix the gauge or transform between different gauges. This may lead to fewer ambiguities in physical interpretations that stem from gauge-dependence, since we now have a unified theoretical framework that is consistent across different materials and models. By this enhancement of the predictive power of theoretical models, our new selection rules may now allow for clearer physical insights into excitonic effects, since they may allow for more-accurate comparisons between theoretical simulations and experiments (which are typically gauge-invariant). This may lead to potentially new phenomena and advances in material design (especially of quantum materials possessing novel electronic and optical properties), which may be achievable in the near-term given today's high rate of advances in interband physics and topological effects in systems like multilayer graphene, TMDs, Moiré heterostructures, qubits, and even other kinds of quasiparticles that can couple with each other (e.g., excitons, magnons, polaritons, polarons, plasmons, and phonons). These advantages may directly influence the development of advanced materials and technologies, with potential applications in optoelectronics, photovoltaics, quantum computing, excitonics, spintronics, and other exciting research fronts in contemporary materials science and condensed matter physics.

# Chapter 4

# METHODS

In this chapter, we outline techniques one could use to calculate the interband index numerically, and list the model Hamiltonians used in this project.

## *4.1 Calculating Interband Index*

In this section, we demonstrate techniques one could use to calculate the interband index. Although we used *Python*, *MATLAB* and *Mathematica* in this work, the choice of programming language should not matter as long as the computational schemes are accurate and consistent. Recall from Eq. (1.33) that

$$\begin{aligned} 2\pi\Theta_k \equiv 2\pi\Theta_{mn} &= \Delta\Phi - \oint_{\partial\mathcal{M}} \mathrm{d}\arg\langle m \,|\, \nabla_{\mathbf{k}} n\rangle \cdot \hat{e}_\tau \\ &= \Delta\Phi - \oint_{\partial\mathcal{M}} \mathrm{d}\arg \frac{\langle m \,|\, \nabla_{\mathbf{k}} H \,|\, n\rangle}{E_{nm}} \cdot \hat{e}_\tau \\ &= \Delta\Phi - W, \end{aligned} \tag{4.1}$$

where we take $W$ to be the interband winding integral (which yields a winding number of the interband matrix element in the complex plane). Recall that $\Delta\Phi = \Phi_m - \Phi_n$ is the net number of Berry singularities between levels, and is given by the difference between the Berry curvature area integral and Berry connection line integral in the chosen parameter space region, as given in Eq. (1.17) (replicated below):

$$\Phi_m = \int_{\partial\mathcal{M}} \mathcal{A}^\mu_m \,\mathrm{d}\lambda_\mu - \iint_{\mathcal{M}} F_m \,\mathrm{d}\lambda_\mu \,\mathrm{d}\lambda_\nu. \tag{4.2}$$

So, to calculate $\Theta_k$, one must:

1. Choose a submanifold $\mathcal{M}$ of 2-dimensional $\boldsymbol{k}$-space by defining a $\boldsymbol{k}$-space loop $\partial\mathcal{M}$ parame-

terized by some parameter $\lambda$.

2. Using the loop $\partial\mathcal{M}$, calculate the winding number of the interband matrix element along the loop.

3. Separately, inside $\mathcal{M}$, calculate the Berry curvature and Berry connection integrals for each band involved to get $\Delta\Phi$.

4. Put everything together in Eq. (4.1) to calculate $\Theta_{mn}$.

In the context of this work, Hamiltonian models $H(\boldsymbol{k})$ are $N \times N$ matrices and generally do not have simple analytic expressions, even for their eigenstates $|m(\boldsymbol{k})\rangle$ and eigenvalues $E_m(\boldsymbol{k})$ (all of which are quantities that are required for the calculation). So we use numerical methods to discretize $\mathcal{M}$ and $\partial\mathcal{M}$ into finite $\boldsymbol{k} = (k_x, k_y)$ segments, and use these coordinates to numerically solve the eigenvalue problem Eq. (1.5). As we shall see in this section, we use finite differences to take derivatives of quantities. Note however, that in some simple cases such as the gapped Dirac fermion model (Section 4.2.3), we can directly use analytic expressions for $H(\boldsymbol{k})$, $|m(\boldsymbol{k})\rangle$ and $E_m(\boldsymbol{k})$, and analytically take derivatives with respect to $\boldsymbol{k}$ to calculate $\Theta$ and even the interband frequency Eq. (1.34) (which contains a second derivative of the Hamiltonian).

We now elaborate on the above steps required to calculate $\Theta$.

### *4.1.1 Choosing k-space $\mathcal{M}$ and $\partial\mathcal{M}$*

To choose a submanifold to calculate $\Theta$ for, one must first define a loop $\partial\mathcal{M}$ in $k$-space. Since $\Theta$ is a topological quantity, the result should not depend on the shape of the loop as long as the same high-symmetry point is enclosed, as long as the loop is smooth, and at least in the case of 2-band models when the sign of Berry curvature is the same within the loop (see Section 1.3.4). So, without loss of generality, we can use a parameterization for a counterclockwise elliptical loop or radii $(r_x, r_y)$ centered at $(K_x, K_y)$:

$$\begin{aligned} k_x(\lambda) &= K_x + r_x \cos(\lambda), \\ k_y(\lambda) &= K_y + r_y \sin(\lambda). \end{aligned} \tag{4.3}$$

Although we tested $\Theta$ using elliptical loops, for further simplicity, we used circular loops ($r_x = r_y = R$) in most of our calculations. In a numerical discretization scheme (as we require for the loop when calculating $W$), one simply chooses to discretize/break the loop into $n$ segments by having $\lambda_i = \frac{2\pi\,(i-1)}{n} \in [0, 2\pi] \quad (i = 1, 2, \ldots, n)$. Unless otherwise noted, we used $n = 250$ in our simulations. Since $\partial\mathcal{M}$ is counterclockwise (CCW), the area of integration is the area inside the loop by convention, as shown in Fig. 4.1 (left).

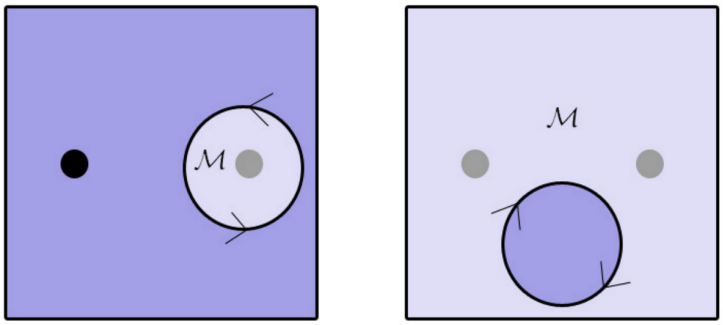


Figure 4.1: The domain of integration $\mathcal{M}$ (light-purple) depends on the orientation of the loop. High-symmetry points $P$ are indicated by black dots, and loops as the circles with arrows indicating orientation. For the CCW loop on the left, only one $P$ is counted. For the CW loop on the right, both are. In general, one cannot expect $\Theta$ calculated for these two examples to correspond to the same topological situation.

### *4.1.2 Calculating winding number W*

To calculate $W$, one must calculate the winding number of the complex-valued quantity $z(\mathbf{k}) = \langle m \,|\, \nabla_{\mathbf{k}} H \,|\, n \rangle / E_{nm} \in \mathbb{C}$ Eq. (4.1). To do this, we evaluate $z(k_x, k_y)$ at each discretized $(k_x, k_y)$ point of the loop and use the curve $(\mathrm{Re}(z), \mathrm{Im}(z))$ to calculate the winding number (i.e., the number of times the curve winds around the complex origin). This winding number is exactly what the integral $W$ above evaluates to. To numerically evaluate the first-order derivative appearing in $z(\mathbf{k})$, we use a central finite difference. For a function $f(\mathbf{k})$, the first-order derivative $f'(\mathbf{k}) = \mathrm{d}f(\mathbf{k})/\mathrm{d}\mathbf{k}$ with error $O(\Delta\mathbf{k}^2)$ could be approximated as:

$$f'(\mathbf{k}) = \frac{f(\mathbf{k} + \Delta\mathbf{k}) - f(\mathbf{k} - \Delta\mathbf{k})}{2\Delta\mathbf{k}}. \tag{4.4}$$

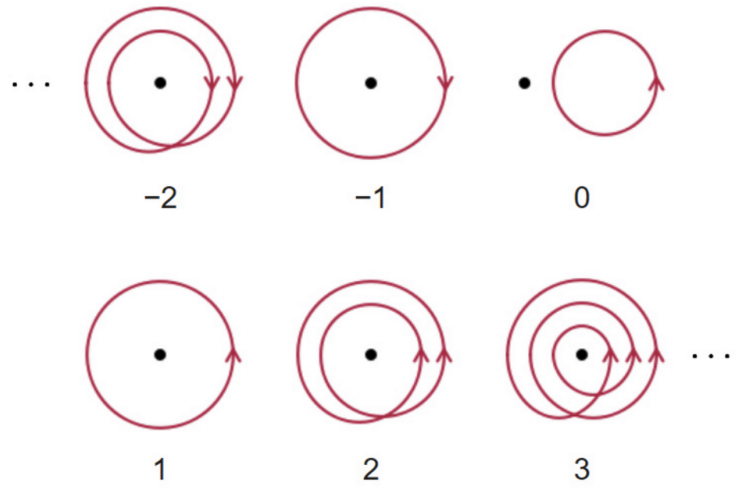


Figure 4.2: Examples of Winding numbers for various CCW and CW loops. The black dots denote the complex origin. Source: *Wikipedia*.

Instead of taking derivatives of the wavefunctions $|m(\boldsymbol{k})\rangle$, we take derivations with respect to $H(\boldsymbol{k})$ (c.f. the second line of Eq. (4.1)) since the derivatives of non-degenerate $H(\boldsymbol{k})$ are guaranteed to be well-defined (unlike $|m(\boldsymbol{k})\rangle$ due to arbitrary complex phases that may be singular). Then, we get $z(\mathbf{k})$ by solving the eigenvalue equation to get $H(\boldsymbol{k}_i), |m(\boldsymbol{k}_i)\rangle, |n(\boldsymbol{k}_i)\rangle, E_m(\mathbf{k}_i)$ and $E_n(\mathbf{k}_i)$ at each point $\mathbf{k}_i = (k_x(\lambda_i), k_y(\lambda_i))$ (computationally represented as an array, for instance) along the loop Eq. (4.3). Bear in mind that the computed eigenstates must be normalized, and that we have the relationship $|m(\boldsymbol{k})\rangle = \langle m(\boldsymbol{k})|^\dagger$, where † denotes the complex conjugate transpose.

From here, one just has to compute the winding number of $z(\mathbf{k})$. Although one could visually determine the winding number (e.g., see Fig. 4.2), it is convenient to do so computationally. For instance, see the Python code in Listing 4.1 [5].

Listing 4.1: Compute the winding number of the complex contour $z(\mathbf{k})$

```
1 def winding_number(w):
2     """
3     Compute the winding number of the complex loop z(k).
4     Parameters
5     ----------
6     w : array_like of complex
```

```
7           Sampled points of the loop z(k) in the complex plane.
8           Adjacent changes in arg(z) must be less than pi for accuracy.
9       Returns
10      -------
11      int
12          The integer winding number of the loop.
13      """
14      out = 0
15      for k in range(len(w) - 1):
16          # handle branch cut at negative real axis
17          if (np.imag(w[k+1]) == 0) and (np.real(w[k+1]) < 0):
18              kp = np.pi * np.sign(np.imag(w[k]))
19          else:
20              kp = np.imag(np.log(w[k+1] / np.linalg.norm(w[k+1])))
21          if (np.imag(w[k]) == 0) and (np.real(w[k]) < 0):
22              kc = np.pi * np.sign(np.imag(w[k+1]))
23          else:
24              kc = np.imag(np.log(w[k] / np.linalg.norm(w[k])))
25          # choose the smaller phase increment
26          opt1 = kp - kc
27          opt2 = -(2 * np.pi - abs(opt1)) * np.sign(opt1)
28          out += opt1 if abs(opt1) <= abs(opt2) else opt2
29      # normalize by 2pi and round to nearest integer
30      return int(round(out / (2 * np.pi)))
```

If one desires to calculate the chiral version of the interband index $\Theta_\pm$ Eq. (3.2), the only change in the algorithm is to use the chiral vectors $\hat{e}_\pm$ Eq. (3.3) instead of the tangential vector $\hat{e}_\tau$. This translates to calculating the winding number of the quantity $\langle m \,|\, \nabla_{\mathbf{k}} H \,|\, n \rangle \cdot \hat{e}_\pm$ as $\left\langle m \,\middle|\, \frac{\mathrm{d}H}{\mathrm{d}k_x} \pm i \frac{\mathrm{d}H}{\mathrm{d}k_y} \,\middle|\, n \right\rangle$ (up to scaling by constants), which again can be carried out using finite differences, or using analytic expressions if feasible.

Finally, we note that the interband frequency Eq. (1.34) was calculated only algebraically in this work (see Fig. 2.1). We used *Mathematica* to take derivatives and products of the quantities in Section 4.2.3. However, a numerical second-order central finite-difference could have been used.

### *4.1.3 Calculating $\Delta\Phi$ using Berry curvature and connection integrals*

To calculate $\Delta\Phi$, one must calculate $\Phi_m$ and $\Phi_n$ Eq. (4.2). To calculate $\Phi_m$, we discretized the two-dimensional $\mathbf{k}$-space grid in the region inside the circular loop, and computed for each energy level the phases from both the Berry curvature $F_m$ and Berry connection $\mathcal{A}_m$ integrals separately. For the $F_m$ integral, we used the standard numerical technique given in Ref. [45] to determine the phase of the product of so-called overlap matrices around each closed rectangular path of the $k$-space grid, but only for the rectangles inside the circular loop. The $\mathcal{A}_m$ integral was obtained by summing the phases of the individual overlap matrices along each segment of each closed rectangular path.

To elaborate, one first discretizes the region inside the loop into a rectangular mesh, as in Fig. 4.3. Unless otherwise noted, in this work, we used a $50 \times 50$ mesh and shift the coordinates of the constituent rectangles by an infinitesimal amount (on the order of $1/100000$) to avoid potential numerical divergences of relevant quantities to infinity. With this setup, following the procedure in Ref. [45], we define matrices $U_{ij}$ to calculate the Berry curvature and Berry connection integrals. The discrete contribution of each integral in each rectangle (see Fig. 4.3):

$$\mathbf{k}_1 = (k_x,\ k_y), \quad \mathbf{k}_2 = (k_x + \Delta k_x,\ k_y), \quad \mathbf{k}_3 = (k_x + \Delta k_x,\ k_y + \Delta k_y), \quad \mathbf{k}_4 = (k_x,\ k_y + \Delta k_y), \tag{4.5}$$

is used to calculate the overlap matrices

$$U_{12} = \big\langle m(\mathbf{k}_2) \,\big|\, m(\mathbf{k}_1)\big\rangle, \quad U_{23} = \big\langle m(\mathbf{k}_3) \,\big|\, m(\mathbf{k}_2)\big\rangle, \tag{4.6}$$

$$U_{34} = \big\langle m(\mathbf{k}_4) \,\big|\, m(\mathbf{k}_3)\big\rangle, \quad U_{41} = \big\langle m(\mathbf{k}_1) \,\big|\, m(\mathbf{k}_4)\big\rangle. \tag{4.7}$$

Then the discrete contribution of the rectangle to the Berry curvature integral $\iint_{\mathcal{M}} F_m \,\mathrm{d}\lambda_\mu \,\mathrm{d}\lambda_\nu$ is

$$\arg\big(U_{12}\, U_{23}\, U_{34}\, U_{41}\big), \tag{4.8}$$

and the discrete contribution to the Berry connection integral $\int_{\partial\mathcal{M}} \mathcal{A}_m^\mu \,\mathrm{d}\lambda_\mu$ is

$$\arg(U_{12}) + \arg(U_{23}) + \arg(U_{34}) + \arg(U_{41}), \tag{4.9}$$

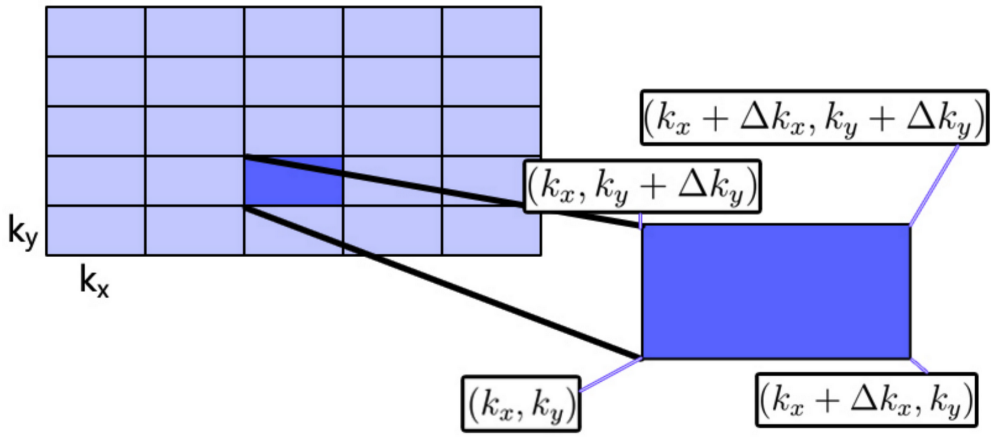


Figure 4.3: Visualizing discretization of $\mathcal{M}$ into a rectangular grid.

where arg() is the complex angle (equivalently Imlog()). We use this technique to calculate $\Phi_m$ and $\Phi_n$ to get $\Delta\Phi$. For illustration, Fig. 4.4 shows what the Berry curvature and Berry connection integrals could look like when plotted.

### *4.1.4 Calculating $\Theta_{mn}$*

We finally calculate $\Theta_k$ using: $2\pi\Theta_{mn} = \Delta\Phi - W$ Eq. (4.1). By calculating all possible $N(N-1)/2$ values of $\Theta_{mn}$ for an $N$-level Hamiltonian, one could the go on to use $N-1$ of them to solve the overdetermined simultaneous equations to calculate the $N$ values of the band-resolved topological charge $\Xi_m$ Eq. (2.6).

## *4.2 Model Hamiltonians*

Following are details of some of the model Hamiltonians that were explored in this project.

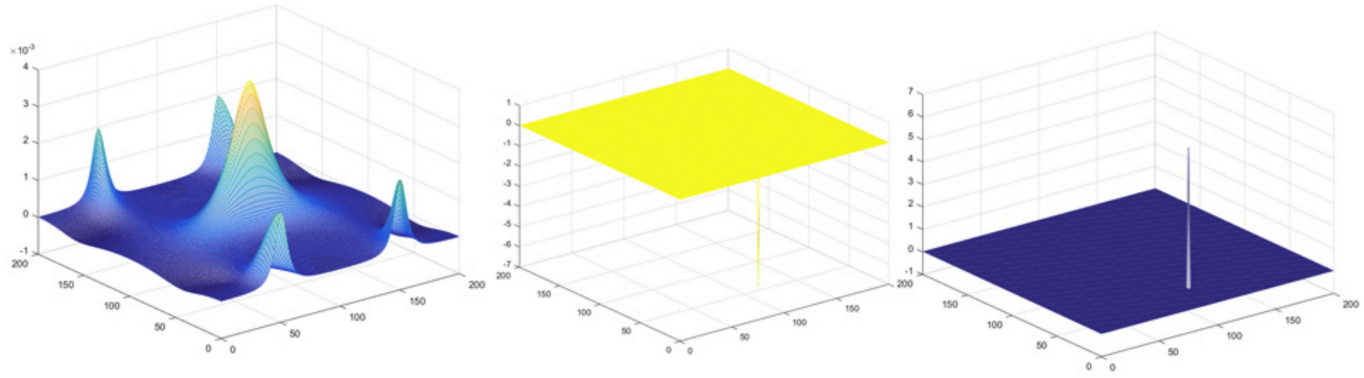

Figure 4.4: Visual representation of quantities used in calculating number of Berry singularities $\Phi_m$, shown over entire Brillouin zone for illustration (instead of within a chosen loop). Simulated for the Haldane model (Section 4.2.1). Left (z-axis values): local Berry curvature integral. Center: Berry connection integral. Right: $\Phi_m$. Notice the peaks occurring at values $\approx |6.3| \approx |2\pi| \to |1|$ singularity. As an aside, if the sum of the Berry curvature integral (left) is taken over the entire Brillouin zone, we get the first Chern number, as in Ref. [45].

### *4.2.1 Haldane model*

On a honeycomb lattice, the Haldane model's Hamiltonian can be written in a Bloch state basis on two sublattices $A, B$, using Pauli matrices $\sigma_i$:

$$\sigma_0 = \mathcal{I} = \begin{pmatrix} 1 & 0 \\ 0 & 1 \end{pmatrix}, \quad \sigma_x = \begin{pmatrix} 0 & 1 \\ 1 & 0 \end{pmatrix}, \quad \sigma_y = \begin{pmatrix} 0 & -i \\ i & 0 \end{pmatrix}, \quad \sigma_z = \begin{pmatrix} 1 & 0 \\ 0 & -1 \end{pmatrix}. \tag{4.10}$$

Below, $t_1$ is the nearest-neighbor hopping, $t_2$ the amplitude of the complex second-neighbor hopping, $\phi$ the phase accumulated by the $t_2$ hopping, and $M$ the on-site energy between the $A$ and $B$ sublattices. $\boldsymbol{a_i}$ are displacements from a $B$ site to its three nearest-neighbor $A$ sites, and $\boldsymbol{b_i}$ are

displacements for nearest-neighbor sites in the same sublattices [43, 56]:

$$\begin{aligned} H(\boldsymbol{k}) &= 2t_2\cos\phi\left[\sum_i \cos\left(\boldsymbol{k}\cdot\boldsymbol{b_i}\right)\right]\sigma_0 \\ &+ t_1\left[\sum_i \left[\cos\left(\boldsymbol{k}\cdot\boldsymbol{a_i}\right)\sigma_x + \sin\left(\boldsymbol{k}\cdot\boldsymbol{a_i}\right)\sigma_y\right]\right] \\ &+ \left[M - 2t_2\sin\phi\left(\sum_i \sin\left(\boldsymbol{k}\cdot\boldsymbol{b_i}\right)\right)\right]\sigma_z. \end{aligned} \tag{4.11}$$

Above,

$$a_1 = \begin{pmatrix} \sqrt{3}/2 \\ 1/2 \end{pmatrix}, \quad a_2 = \begin{pmatrix} -\sqrt{3}/2 \\ 1/2 \end{pmatrix}, \quad a_3 = \begin{pmatrix} 0 \\ -1 \end{pmatrix}, \tag{4.12}$$

and

$$b_1 = a_2 - a_3, \quad b_2 = a_3 - a_1, \quad b_3 = a_1 - a_2. \tag{4.13}$$

Notice that we can write the above Hamiltonian Eq. (4.11) in the form

$$H(\mathbf{k}) \;=\; h_0(\mathbf{k})\,\sigma_0 \;+\; \mathbf{h}(\mathbf{k})\cdot\boldsymbol{\sigma}, \tag{4.14}$$

with $\mathbf{h}(\mathbf{k}) = (h_x, h_y, h_z)$ and $\boldsymbol{\sigma} = (\sigma_x, \sigma_y, \sigma_z)$, and

$$\begin{aligned} h_0(\mathbf{k}) &= 2\,t_2\cos\phi\sum_i \cos\big(\mathbf{k}\cdot\mathbf{b}_i\big), \\ h_x(\mathbf{k}) &= t_1\sum_i \cos\big(\mathbf{k}\cdot\mathbf{a}_i\big), \\ h_y(\mathbf{k}) &= t_1\sum_i \sin\big(\mathbf{k}\cdot\mathbf{a}_i\big), \\ h_z(\mathbf{k}) &= M \;-\; 2\,t_2\sin\phi\sum_i \sin\big(\mathbf{k}\cdot\mathbf{b}_i\big). \end{aligned} \tag{4.15}$$

### *4.2.2 Spin-1/2 in external magnetic field*

This simple 2-level Hamiltonian is of the form

$$H(t) = B\mathbf{n}(t) \cdot \boldsymbol{\sigma}, \tag{4.16}$$

where $B$ is a constant dictating the strength of the external magnetic field, $\mathbf{n}(t)$ is a 3-dimensional unit vector and the entire parameter space is the $\mathbb{S}^2$ Bloch sphere. The angular variables $(\theta, \phi)$ could be made to parameterize the parameter space with

$$\mathbf{n}(\theta, \phi) = (\sin(\theta)\cos(\phi), \sin(\theta)\sin(\phi), \cos(\theta)). \tag{4.17}$$

This setup is illustrated in Fig. 1.3.

For calculations, one could select a gauge where the two wavefunctions are:

$$|n(\theta,\phi)\rangle = \begin{pmatrix} \sin\left(\frac{\theta}{2}\right) e^{-i\phi} \\ -\cos\left(\frac{\theta}{2}\right) \end{pmatrix}, \qquad |m(\theta,\phi)\rangle = \begin{pmatrix} \cos\left(\frac{\theta}{2}\right) e^{-i\phi} \\ \sin\left(\frac{\theta}{2}\right) \end{pmatrix}. \tag{4.18}$$

### *4.2.3 Gapped chiral fermion model*

The 2-dimensional gapped Dirac fermion model [29,56,195,196] has a $k \cdot p$ Hamiltonian with integer winding number $w$:

$$H(\boldsymbol{k}) = \begin{pmatrix} \Delta & \alpha|\boldsymbol{k}|^\gamma e^{iw\phi_k} \\ \alpha|\boldsymbol{k}|^\gamma e^{-iw\phi_k} & -\Delta \end{pmatrix}, \tag{4.19}$$

where the energy gap is $2\Delta$, and $\phi_{\boldsymbol{k}} = \tan^{-1}(k_y/k_x)$. While $\gamma$ can take on arbitrary integral values in graphene multilayers [196], we note that in monolayer $MoS_2$ and gapped topological surface states, $\alpha(|\boldsymbol{k}|) \propto |\boldsymbol{k}| = \sqrt{k_x^2 + k_y^2}$ (that is, $\gamma = 1$), and that in biased bilayer graphene, $\alpha(|\boldsymbol{k}|) \propto |\boldsymbol{k}|^2$ ($\gamma = 2$). The energy dispersions for the upper ($E_m$) and lower ($E_n$) bands are respectively $\pm\sqrt{\Delta^2 + \alpha^2|\boldsymbol{k}|^{2\gamma}}$. Diagonalizing Eq. (4.19), we can get the eigenstates

$$|m(\mathbf{k})\rangle = \begin{pmatrix} \cos\dfrac{\theta_k}{2} \\ \sin\dfrac{\theta_k}{2}\, e^{-iw\phi_k} \end{pmatrix}, \qquad |n(\mathbf{k})\rangle = \begin{pmatrix} \sin\dfrac{\theta_k}{2}\, e^{iw\phi_k} \\ -\cos\dfrac{\theta_k}{2} \end{pmatrix}, \tag{4.20}$$

where $\theta_k = \cos^{-1}\left(\frac{\Delta}{E_m}\right)$, and the eigenstates have $U(1)$ gauge freedom, meaning you can multiply the states by some arbitrary $\boldsymbol{k}$-dependent phase $e^{i\theta(\boldsymbol{k})}$.

Using the above expressions, the Berry curvature of the gapped Dirac fermion model is calculated as [176]:

$$\frac{\gamma\omega\Delta\alpha^2|k|^{2(\gamma-1)}}{2(\Delta^2+\alpha^2|k|^{2\gamma})^{3/2}}. \tag{4.21}$$

Fig. 4.5 shows the Berry curvature distribution to supplement the argument around Fig. 2.1. Notice that the Berry curvature sums to $\approx 1.5 \times 2\pi$ Å$^{-2}$.

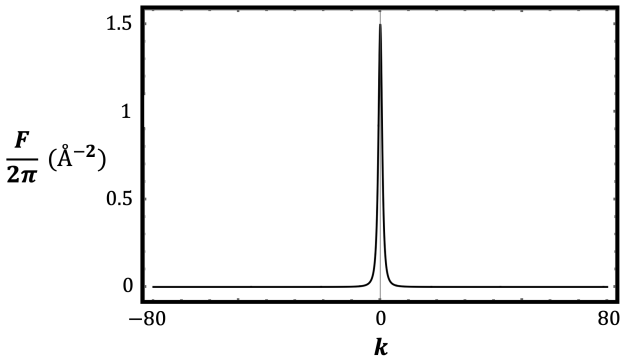


Figure 4.5: Berry curvature of the gapped Dirac fermion model along the line $k_y = 0$. This is the same case as in Fig. 2.1, where varying $r$ from 0 to 80 encompasses $-80 \leq k_x \leq 80$.

### *4.2.4 Spinful Dirac Hamiltonian on monolayer honeycomb lattice*

Ref. [34] gives the following low-energy Hamiltonian:

$$H(\boldsymbol{k}) = \hbar v_F(\eta_z k_x \tau_x + k_y \tau_y) + \lambda_{SO}\eta_z\sigma_z\tau_z + m_z\sigma_z\tau_z, \tag{4.22}$$

at the $K$ or $K'$ point. Above, $s_z = \pm 1$ for spin $(\uparrow, \downarrow)$, $\tau_z = \pm 1$ for sublattice $(A, B)$ and $\eta_z = \pm 1$ for valley $(K, K')$. The Pauli matrices $\sigma_a, \tau_a$ and $\eta_a$ are used for spin, sublattice pseudospin and valley pseudospin respectively. The first term represents electron hoppings with Fermi velocity $v_F$; the second term describes spin-orbit coupling defined by $\lambda_{SO}$; and the third term breaks time-reversal symmetry (equivalent to antiferromagnetic exchange magnetization in $z$-direction).

### *4.2.5 Gapped bilayer graphene with layer-stacking wall*

Ref. [192] uses the following 4-band Hamiltonian to study topological properties in a layer-stacking domain wall problem:

$$H(\boldsymbol{k}) = \Delta\tau_z + \nu k_x\sigma_x + k_y\sigma_y + \frac{\gamma}{2}(\sigma_x\tau_x - \mu\sigma_y\tau_y), \tag{4.23}$$

where the Brillouin zone corners $K$ and $K'$ are at the origin and labeled by the valley index $\nu = \pm 1$ respectively. $\Delta$ controls the strength of the applied electric potential difference, $\gamma$ is the renormalized nearest-interlayer-neighbor hopping amplitude, and $\mu \to \pm 1$ controls the interlayer registry (i.e. whether an AB or BA sublattice is used). In our calculations, we used $\Delta = 0.05, \gamma = 0.1$, and $\nu = +1$. The band edge is at the origin.

### *4.2.6 ABC-stacked trilayer graphene*

Ref. [80] gives the following effective Hamiltonian around a $K$ valley:

$$H(\boldsymbol{k}) = \begin{pmatrix} D_1 & V & W \\ V^* & D_2 & V \\ W^* & V^* & D_3 \end{pmatrix}, \tag{4.24}$$

where the $2 \times 2$ blocks, for $i = 1, 2, 3$ are

$$D_i = \begin{pmatrix} U_i & v\pi^*, \\ v\pi & U_i \end{pmatrix}, \tag{4.25}$$

$$V = \begin{pmatrix} -v_4\pi^* & v_3\pi \\ \gamma_1 & -v_4\pi^* \end{pmatrix}, \tag{4.26}$$

$$W = \begin{pmatrix} 0 & \gamma_2/2 \\ 0 & 0 \end{pmatrix}, \tag{4.27}$$

for $\pi = \xi k_x + ik_y$, $\xi$ the valley index, $v = (\sqrt{3}/2)a\gamma_0/\hbar, v_3 = (\sqrt{3}/2)a\gamma_3/\hbar, v_4 = (\sqrt{3}/2)a\gamma_4/\hbar, \gamma_0 = 3.16, \gamma_1 = 0.39, \gamma_2 = -0.020, \gamma_3 = 0.315, \gamma_4 = 0.044, a = 2.46$, and choose $(U_1, U_2, U_3) = (-0.2, 0, 0.2)$ for a loop centered around band edge $(0, 0)$.

### *4.2.7 Qi-Wu-Zhang (QWZ) model*

In the spirit of Haldane's model, Qi, Wu and Zhang introduced this simple toy model for a two-dimensional Chern insulator leading to the Quantum Anomalous Hall Effect. This model is the basic building block for the Bernevig-Hughes-Zhang model for the quantum spin Hall effect. While the reader is referred to Ref. [3] for a review of the Qi-Wu-Zhang model, we draw from it information on its $k$-space Hamiltonian, information of high-symmetry points, and topological phases.

The model is given by:

$$H(\boldsymbol{k}) = \sin k_x \sigma_x + \sin k_y \sigma_y + [u + \cos k_x + \cos k_y]\sigma_z \tag{4.28}$$

The energy gap

$$E_{\pm}(k_x, k_y) = \pm\sqrt{\sin^2(k_x) + \sin^2(k_y) + [u + \cos(k_x) + \cos(k_y)]^2}$$

closes when $u = \pm 2, 0$ at the following four inequivalent Dirac points in the Brillouin zone chosen as $(k_x, k_y) \in [-\pi/2, 3\pi/2] \times [-\pi/2, 3\pi/2]$:

- $(k_x, k_y) = (0, 0)$ when u = -2 ($\Gamma$ point),
- $(k_x, k_y) = (0, \pi)$ and $(k_x, k_y) = (\pi, 0)$ when u = 0 (inequivalent $X$ points),
- $(k_x, k_y) = (\pi, \pi)$ when u = +2 ($M$ point).

### *4.2.8 Generalized 3-band Haldane model on optical lattice*

Ref. [102] gives the following 3-band Hamiltonian:

$$H(\boldsymbol{k}) = \begin{pmatrix} \xi_a^k & \lambda_a^{k*} & 0 \\ \lambda_a^k & \xi_c^k & \lambda_b^{k*} \\ 0 & \lambda_b^k & \xi_b^k \end{pmatrix}, \tag{4.29}$$

where:

$$\begin{aligned}\xi^k_{a(b)} &= \Delta_{a(b)} - 2t\Sigma_i \cos(\boldsymbol{k}\cdot\boldsymbol{u_i} + \phi_i)\\ \xi^k_c &= -2t\Sigma_i \cos(\boldsymbol{k}\cdot\boldsymbol{u_i} - \phi_i)\\ \lambda^k_{a(b)} &= \lambda_{a(b)}\Sigma_i e^{i\boldsymbol{k}\cdot\nu_i},\end{aligned}$$

for $\boldsymbol{u_i} = (b_1, b_2, b_3)$ and $\boldsymbol{\nu_i} = (a_1, a_2, a_3)$ given by honeycomb lattice vectors:

$$a_1 = \begin{pmatrix}\sqrt{3}/2\\ 1/2\end{pmatrix}, \quad a_2 = \begin{pmatrix}-\sqrt{3}/2\\ 3/2\end{pmatrix}, \quad a_3 = \begin{pmatrix}0\\ -1\end{pmatrix},$$
$$b_1 = \begin{pmatrix}-\sqrt{3}/2\\ 3/2\end{pmatrix}, \quad b_2 = \begin{pmatrix}-\sqrt{3}/2\\ -3/2\end{pmatrix}, \quad b_3 = \begin{pmatrix}\sqrt{3}\\ 0\end{pmatrix}.$$

In this model, $*$ denotes complex conjugation (or conjugate transpose).

The 2D Brillouin zone used was $(k_x, k_y) \in [\pi/\sqrt{3}, 3\pi/\sqrt{3}] \times [-2\pi/3, 2\pi/3]$, with Dirac points at $(k_x, k_y) = (\pm 4\pi/3\sqrt{3}, 0)$. We set the coupling strength $\lambda_{a(b)}$ as $\lambda_a = 0.3$ and $\lambda_b = 1.7$ (their values do not affect Chern numbers). For consistency with the authors' analysis, we stick to the isotropic case with $\phi_i = 2\pi/3$.

### *4.2.9 Gated bilayer graphene with Rashba spin-orbit coupling and exchange field*

Ref. [140] gives the following momentum space 8-band effective Hamiltonian for the valley points $K$ and $K'$ (centered at the origin $(0, 0)$ and respectively labeled by $\eta = \pm 1$):

$$\begin{aligned}\boldsymbol{H}(\boldsymbol{k}) = {} & v(\eta\sigma_z k_x + \sigma_y k_y)\mathbf{1}_s\mathbf{1}_\tau + \frac{t_\perp}{2}(\sigma_x\tau_x - \sigma_y\tau_y)\mathbf{1}_s\\ & + \frac{\lambda_R}{2}(\eta\sigma_x s_y - \sigma_y s_x)\mathbf{1}_\tau + M s_z\mathbf{1}_\sigma\mathbf{1}_\tau + U\tau_z\mathbf{1}_s\mathbf{1}_\tau,\end{aligned} \tag{4.30}$$

where $s$, $\sigma$ and $\tau$ are Pauli matrices representing the spin, AB sublattice, and top-bottom layer degrees of freedom respectively. $\mathbf{1}_i$ are $2 \times 2$ identity matrices. The Fermi velocity is given by $v = 3at/2$ with $a$ the lattice constant, and $t$ the hopping amplitude. $t_\perp$ is the interlayer tunneling amplitude, $\lambda_R$ the Rashba spin-orbit coupling, $U$ the interlayer potential, and $M$ the exchange field. We used $a = 1, t = 2.6, t_\perp = 0.143t, M = 0, U = 0.3t$ and $t_R = 0.058t$.

We ignored the exchange field $M$ in our calculations for simplicity in presentation. However, using $M \neq 0$, we were able to reproduce the phase diagrams in Ref. [140] which classify quantum anomalous Hall, quantum valley Hall, and metallic phases (c.f. Fig. 15 of the reference).

#### *4.2.10 2-band biased bilayer graphene model*

From Ref. [117, 132, 196], we have:

$$H = \begin{pmatrix} \Delta & \alpha k_+^2 \\ \alpha k_-^2 & -\Delta \end{pmatrix} + 3\gamma_3 \begin{pmatrix} 0 & k_- \\ k_+ & 0 \end{pmatrix}, \tag{4.31}$$

where $k_\pm = k_x \pm ik_y$, $\gamma_3$ is the interlayer hopping amplitude, $2\Delta$ is the energy gap, and we set the factor $\alpha = 1$.

### *4.3 Part I Summary*

In Part I of this dissertation, we explored the theory behind the novel interband index, and presented two new applications of the index: 1) in valley topology [38]; and 2) in optical selection rules for excitons [36]. We have thus shown that the interband index, although appearing abstract at first, does have physical manifestations in the real world.

# Part II

# MAGNETISM IN MONOLAYER $Nb_3Cl_8$

# Chapter 5

# BACKGROUND AND MOTIVATION

The study of two-dimensional (2D) magnetic phenomena in quantum materials has gained significant interest due to its potential to reveal novel quantum states and exotic magnetic properties [17, 67, 194]. The ability to control and tune the magnetic order of a material is particularly appealing because it allows us to explore new physical phenomena, develop advanced technologies, and improve the performance of existing materials and devices [92, 189]. This ability facilitates several applications in condensed matter physics and materials science, such as in quantum information science and technology [190, 202], the development of spintronic devices and memory [190, 202], magnetic sensing and imaging [28], and the exploration of phenomena in quantum materials including novel electronic and magnetic materials [17, 67, 194] and magnetic frustration [118]. The phenomenon of magnetic frustration, where competing interactions prevent the system from adopting a simple magnetic order, is particularly appealing. In particular, frustrated systems can host exotic quantum states, such as spin liquids, which offer insights and applications in high-temperature superconductivity, quantum computation, and other emergent phenomena [4, 16, 118]. In this work, we explore the tuning of magnetic correlations in a 2D breathing kagome lattice material which may yield frustration.

A kagome lattice consists of corner-sharing triangles that tile the plane to form hexagons. Its band structure can host Dirac crossings, van Hove singularities, and nearly dispersionless flat bands that amplify interaction effects and enable unusual transport and topology [103, 116]. ARPES has directly observed several of these signatures in kagome compounds [72, 130], which has driven interest in using kagome platforms to explore topological responses and correlation-enhanced phenomena with device relevance [144, 145].

A breathing kagome lattice is a variant where the triangles alternate between large and small, so bond lengths and triangle areas are modulated across the plane. This alternation can stabilize (sometimes topological) flat-band features, modify Dirac gaps through symmetry breaking, and even

allow coupling to polar distortions and ferroelectricity in some cases [11,96]. Because the breathing pattern reshapes the low-energy electronic structure and the spin Hamiltonian, it provides extra handles for tuning magnetic anisotropy and exchange, which makes it a natural setting for strain control.

The $Nb_3X_8$ family (X = Cl, Br, I) are layered van der Waals semiconductors whose Nb planes realize a breathing kagome motif [109]. They have moderate band gaps, can be exfoliated to monolayers, and integrate well into heterostructures, which is attractive for optoelectronic and spintronic architectures [75, 160]. Prior work has highlighted kagome-derived flat-band features and semiconducting behavior in this family using ARPES, and has motivated detailed studies of how lattice geometry couples to magnetism. My own contributions include DFT calculations for works studying phonon modes using Raman spectroscopy on $Nb_3Cl_8$ [65], as well as for works using ARPES measurements on $Nb_3Br_8$ [39, 145] and $Nb_3I_8$ [144]. However, in this dissertation I focus on monolayer $Nb_3Cl_8$ and show how controlled strain can be used to tune its magnetic order, as given in Ref. [37].

### *5.1 Monolayer $Nb_3Cl_8$*

Several factors motivate a focused study of $Nb_3Cl_8$. It may host topological flat bands in its electronic dispersion [19, 30, 65, 101, 146, 160], which in turn can stabilize strongly correlated insulating phases [2, 64, 155]. It has also been identified as a candidate to realize the Hubbard model [48, 55, 197], Mott-insulating behavior [48, 55, 64, 99, 158, 183, 197], field-effect transistors [90, 106], topological insulators [15], heterostructure phenomena [105, 184], excitonic effects [74], and charge-ice physics [158]. Magnetically, both bulk and monolayer $Nb_3Cl_8$ are paramagnetic at high temperature [48,133,158], with bulk material undergoing a $\sim$90 K transition to a nonmagnetic singlet ground state [13,48,58,59,65,76,99,133,154]. However, the exact magnetic ground state of the monolayer remains unsettled, with reports ranging from ferromagnetic [66,76] to antiferromagnetic [2,55,59,158,160,186] and even quantum spin liquid candidates [55,59,64,99,197]. To date, there are very few studies addressing the impact of spin–orbit coupling (SOC) in the monolayer or exploring how its magnetic order can be tuned. Strain is especially important, as it can drive changes in the ground state; yet aside from Ref. [122], which considered strain only in terms of mechanical

properties, strain effects in $Nb_3Cl_8$ have not been examined.

In this work, we focus on the magnetic properties of monolayer $Nb_3Cl_8$. Recent studies of the monolayer cover a wide range of topics [48, 55, 64, 66, 122, 158, 160, 186, 197], including evidence that its synthesis may be experimentally achievable [66, 122, 160, 186]. $Nb_3Cl_8$ belongs to space group 156 (P3m1), which lacks inversion symmetry, permitting nonzero Dzyaloshinskii–Moriya interactions (DMI) in the presence of SOC. SOC further enriches the magnetic landscape by introducing anisotropy and extending the role of extended-neighbor interactions, whose combined influence on the magnetic order remains unexplored.

### *5.2 Band Diagrams*

As a first illustrative step, we use DFT calculations (using methods in Chapter 6.1) to present band diagrams for monolayer $Nb_3Cl_8$ in Fig. 5.1 (a)-(c). We note that our band diagram for the case without spin polarization Fig. 5.1 (a) compares well with diagrams from other references, such as Ref. [55, 160] even though they used PBE as the exchange-correlation energy functional (compared to the LDA we used, see Sec. 6.1).

We also present a plot of magnetization (i.e., spin density) in Fig. 5.1 (d).

### *5.3 Effective Triangular Lattice and Frustration*

As mentioned, $Nb_3X_8$ has a breathing Kagome lattice consisting of alternating large and small $Nb_3$ triangles. However, it is a molecular cluster magnet because each small $Nb_3$ triangle, or *$Nb_3$ trimer*, shares a single molecular orbital with a $S = \frac{1}{2}$ moment [48, 55, 58, 59, 64, 99, 126, 133, 154, 155, 158, 186, 197]. The $Nb_3$ trimers share a single spin-$\frac{1}{2}$ moment because the three Nb $4d$ $t_{2g}$ orbitals $\{d_{xy}, d_{yz}, d_{xz}\}$ on each site hybridize strongly within a face-sharing triangle to form cluster molecular orbitals that split into a bonding singlet $1a_1$, a bonding doublet $1e$, and a higher bonding level $2a_1$. With a total of seven $4d$ electrons per $[Nb_3]^{8+}$ unit, six electrons fully occupy the lower bonding states, $1e^4\,1a_1^2$, and the seventh electron resides in the $2a_1$ level, giving the configuration

$$(1e)^4(1a_1)^2(2a_1)^1,$$

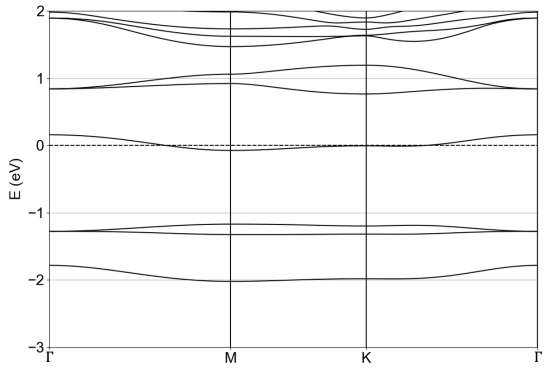


(a) No spin polarization.

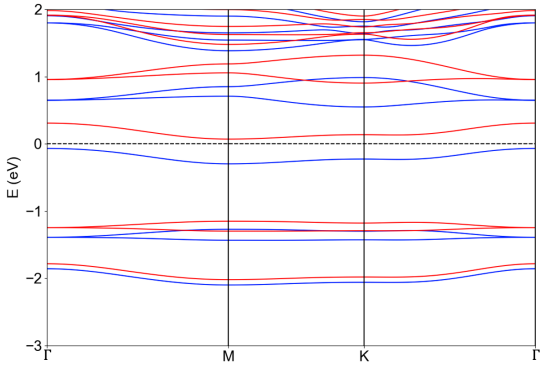


(b) Spin polarized, but without SOC. Blue bands are the spin up channel, and red bands spin down.

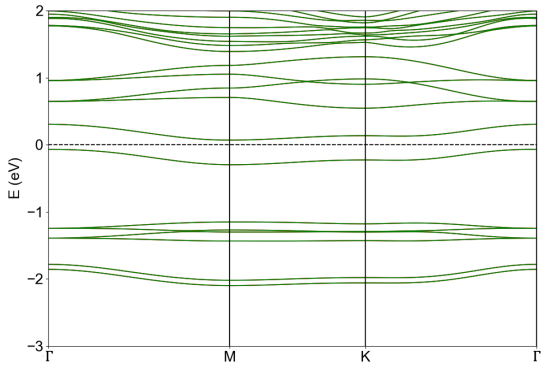


(c) With SOC. Bands are doubly-degenerate.

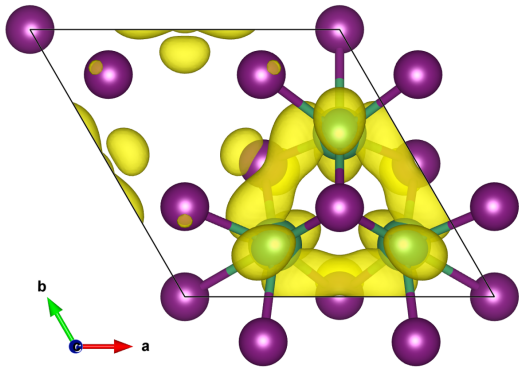


(d) Magnetization in monolayer $Nb_3Cl_8$.

Figure 5.1: (a)-(c) Band diagrams for monolayer $Nb_3Cl_8$ along the path $\Gamma - M - K - \Gamma$ in the Brillouin zone. (d) Magnetization (yellow) in monolayer $Nb_3Cl_8$ unit cell, viewed from above the *ab*-plane. The magnetization is calculated by subtracting the spin up density by the spin down density. Nb atoms are in green, and Cl atoms in purple. Most of the magnetization is from the Nb atoms, while the small yellow bubbles in the top-left are minor contributions from Cl atoms.

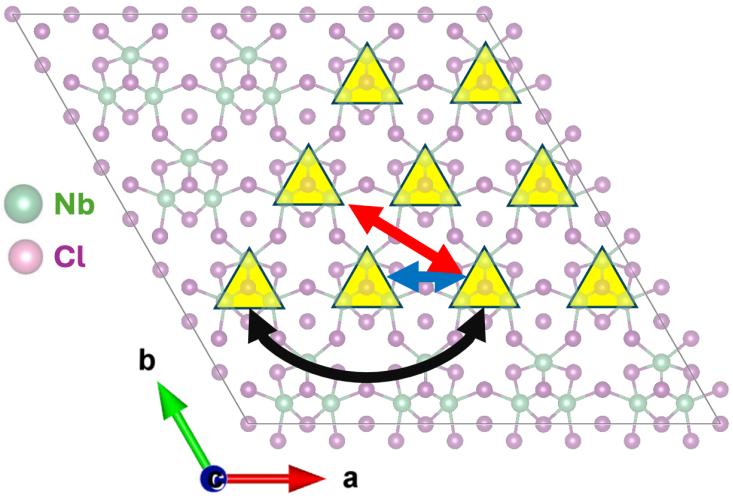


Figure 5.2: $Nb_3Cl_8$ crystal structure shown as a $4 \times 4 \times 1$ supercell, viewing the $ab$-plane from above [120]. The semi-transparent atoms show the Nb (green) and Cl (purple) atoms of the breathing Kagome lattice (with alternating big and small $Nb_3$ triangles). A few $Nb_3$ trimers (small $Nb_3$ triangles sharing a single $S = \frac{1}{2}$ moment) are marked as yellow triangles. If each yellow triangle is considered a single point, we see the overlying triangular lattice. The arrows connecting triangles indicate the trimer bond pairs we chose in calculating NN (blue), 2NN (red), and 3NN (black) interactions. The triangle with three arrows pointing towards it is considered the atom with the first index in each bond.

so that one unpaired electron is delocalized over the trimer and yields an effective spin-$\frac{1}{2}$ per $Nb_3$ cluster [58].

So, despite having a Kagome lattice, $Nb_3X_8$ effectively behaves as a triangular lattice magnetically, with each $Nb_3$ trimer corresponding to a single triangle vertex (see Fig. 5.2). The triangular lattice makes $Nb_3X_8$ susceptible to magnetic frustration, because the geometric arrangement of spins in an equilateral triangle prevents all three spins from simultaneously aligning antiferromagnetically, leading to competing interactions that cannot be satisfied simultaneously. If the magnetic correlations could be tuned between antiferromagnetic and other states, we would have an exciting means to progress in the hunt for quantum systems offering magnetic control. Therefore, it is important to accurately model the magnetic properties of $Nb_3X_8$ to understand its potential for hosting exotic quantum states, and as a playground for manipulating magnetic order.

### *5.4 This Work*

A common approach to study magnetic anisotropy is to calculate energy differences among distinct spin configurations. The 4-state energy mapping formalism is especially powerful in this regard [150, 174, 175]. It reduces ambiguity in near-degenerate cases, accounts comprehensively for interactions (including anisotropic exchange), and, when based on accurate *ab initio* calculations, can yield good agreement with experiment. Yet for $Nb_3Cl_8$, this formalism has not been applied to the effective triangular lattice formed by $Nb_3$ trimers [2, 48, 55, 58, 112, 154, 158, 160, 193].

To address this gap in the literature, we employ the 4-state mapping method [150] on the triangular trimer lattice to extract magnetic anisotropy parameters for a generalized Heisenberg-like Hamiltonian [Eq. (6.9)], including interactions up to third-nearest neighbors. To capture the system's complexity more accurately, we extend beyond isotropic exchange [2, 48, 55, 58, 112, 154, 158, 160, 193] by incorporating SOC-induced anisotropic exchange, DMI, and single-ion anisotropy. Using *ab initio* calculations, we determine these parameters, which are collectively absent in prior studies, and subsequently calculate the magnetic susceptibility using classical Monte Carlo simulations. Fitting the data to the Curie-Weiss law reveals local antiferromagnetic correlations with a negative Weiss temperature, consistent with frustration on the triangular lattice (which is also evidenced by the calculated moderate frustration index). We also find nonzero DMI of comparable magnitude to the anisotropic exchange. Finally, we demonstrate that biaxial strain can tune the magnetism between antiferromagnetic, paramagnetic, and ferromagnetic correlations, providing a route to manipulate the magnetic properties of $Nb_3Cl_8$.

In the next Chapter 6 we present the methods used in this work, and in the following Chapter 7 we present our results. My work on $Nb_3X_8$ appears in Ref. [37, 39, 40, 65, 144].

# Chapter 6

# METHODS

## *6.1 Density Functional Theory Calculations*

In this work, we use *ab initio* Density Functional Theory (DFT) in our ground-state calculations. First-principles DFT recasts the interacting $N$-electron problem in terms of the ground-state electron density $n(\mathbf{r})$, rather than the full many-body wavefunction, thereby making calculations for real materials tractable [62, 79]. DFT is commonly implemented in plane-wave codes such as VASP [85] and Quantum Espresso [49].

### *6.1.1 Kohn–Sham Equations*

Under the Born–Oppenheimer approximation [12], the nuclei are treated as fixed, and the electronic Hamiltonian (in atomic units $\hbar = m = e = 1$) reads

$$H \;=\; \sum_{i}^{N}\Big(-\tfrac{1}{2}\nabla_i^2 \;+\; V_{\mathrm{ext}}(\mathbf{r}_i)\Big) \;+\; \tfrac{1}{2}\sum_{i\neq j}^{N}\frac{1}{|\mathbf{r}_i-\mathbf{r}_j|}, \tag{6.1}$$

where the first term is the kinetic energy of the electrons, the second term is the external potential due to the fixed nuclei, and the last term accounts for electron-electron Coulomb repulsion. The exact many-electron wavefunction $\Psi(\mathbf{r}_1,\ldots,\mathbf{r}_N)$ satisfies

$$H\,\Psi \;=\; E\,\Psi. \tag{6.2}$$

Because solving Eq. (6.2) directly is exponentially expensive in $N$, DFT uses two theorems by Hohenberg and Kohn [62] to show that the ground-state energy $E[n]$ is a functional of $n(\mathbf{r})$ and that the correct $n(\mathbf{r})$ minimizes this functional.

Kohn and Sham [79] derived a practical scheme in which one solves a set of effective single-

particle equations

$$\left[-\tfrac{1}{2}\nabla^2 + V_{\mathrm{ext}}(\mathbf{r}) + V_H(\mathbf{r}) + V_{\mathrm{xc}}(\mathbf{r})\right]\psi_i(\mathbf{r}) \;=\; \varepsilon_i\,\psi_i(\mathbf{r}), \tag{6.3}$$

where the electron density is built from the occupied Kohn–Sham orbitals,

$$n(\mathbf{r}) \;=\; \sum_{i=1}^{N} |\psi_i(\mathbf{r})|^2. \tag{6.4}$$

In Eq. (6.3), the Hartree potential

$$V_H(\mathbf{r}) \;=\; \int \frac{n(\mathbf{r}')}{|\mathbf{r}-\mathbf{r}'|}\,\mathrm{d}\mathbf{r}' \tag{6.5}$$

describes the classical electrostatic repulsion of the total electron density (including a self-interaction error), and $V_{\mathrm{xc}}$ is the exchange-correlation potential defined by the functional derivative

$$V_{\mathrm{xc}}(\mathbf{r}) \;=\; \frac{\delta E_{\mathrm{xc}}[n]}{\delta n(\mathbf{r})}. \tag{6.6}$$

### *6.1.2 Exchange–Correlation Functionals*

Since the exact $E_{\mathrm{xc}}[n]$ is unknown, practical DFT uses approximations. In the local density approximation (LDA), one assumes the exchange–correlation energy density at each point equals that of a uniform electron gas of density $n$:

$$E_{\mathrm{xc}}^{\mathrm{LDA}}[n] \;=\; \int n(\mathbf{r})\,\varepsilon_{\mathrm{xc}}\big(n(\mathbf{r})\big)\,\mathrm{d}\mathbf{r}, \tag{6.7}$$

where $\varepsilon_{\mathrm{xc}}(n)$ is taken from quantum Monte Carlo data for the homogeneous electron gas [22, 138].

Generalized gradient approximations (GGA) are also popular and include dependence on the density gradient $\nabla n$:

$$E_{\mathrm{xc}}^{\mathrm{GGA}}[n] \;=\; \int n(\mathbf{r})\,\varepsilon_{\mathrm{xc}}\big(n(\mathbf{r}),\,\nabla n(\mathbf{r})\big)\,\mathrm{d}\mathbf{r}. \tag{6.8}$$

Common GGA forms include the Perdew–Wang (PW91) [137] and Perdew–Burke–Ernzerhof (PBE) [136] functionals.

In this work, we use LDA.

### *6.1.3 Simulation Details*

First-principles DFT+U+SOC calculations were performed using the VASP package version 6.4.1 [82–84, 86, 87], for Hubbard $U$ and spin-orbit coupling (SOC). The valence electron and core interactions were described using the projector augmented wave (PAW) method [10, 88]. For the exchange-correlation energy functional, we used the local density approximation (LDA) [79]. Within the applied PAW pseudopotentials, we included semicore $4s$ and $4p$ states as valence electrons for Nb, and only the standard $3s$ and $3p$ states as valence electrons for Cl. We used a $4 \times 4 \times 1$ supercell for the monolayer. Since lattice parameter information from experiment is not available for the monolayer, we used the parameters $a = 6.744$ Å and $\alpha = 120°$ from single-crystal X-ray diffraction data for $\alpha$-$Nb_3Cl_8$ [109], which is the multi-layer high-temperature structure that is proposed to lead to exotic spin phenomena and remain in the $\alpha$ phase at low temperatures if exfoliated at high temperatures [55, 99, 133]. A vacuum spacing of 25Å along the $c$-direction was applied to avoid interactions between periodic images of the monolayers. We used a $1 \times 1 \times 1$ Γ-centered mesh with automatically-determined $k$ points. The conjugate-gradient algorithm was used to relax only the atom positions until the norms of all the forces were smaller than $10^{-7}$ $eV/\dot{\text{A}}$.

We constrained all magnetic moments of the Nb atoms to be in the $x$-direction in the relaxation, to account for the in-plane anisotropy, which we verified by noting that in-plane moments yielded the lowest energies. To reach this conclusion, we compared the energies of several configurations that differed in the direction of magnetic moments assigned. All Nb atoms in each case had one of the following directions: $(1, -1.73205, 0)$, $(-0.5, 0.8660254, 0)$, $(1, 0, 0)$, $(0, 1, 0)$,$(-1.73205, -1, 0)$, $(1, 1, 0)$, $(-1, 1, 0)$, $(0, 1, 1)$, $(1, 0, 1)$, $(0, 0, 1)$.

In order to accurately capture the shared spin-1/2 moment, we constrained the direction and sign of the assigned moment, but not the size (which we let the software determine). When considering different spin configurations between $Nb_3$ trimers (e.g., for the 4-state energy mapping analysis in Sec. 6.3), each Nb atom in a trimer is assigned the same initial magnetic moment, to correspond to the desired moment of a triangle vertex point. The convergence criterion of the total energy was $10^{-8}$ eV. The energy cutoff for the plane-wave basis set was $ENCUT = 400$ eV, which is greater than the standard value of 1.3× the highest $ENMAX$ value appearing in $POTCAR$ (in our case, $ENMAX = 293.304$). This is with the exception for the $J_{ij}^k$ vs. strain plots Fig. 7.4,7.5,7.6, which

use *ENCUT* = 350 eV; see Sec. 7.2). We used Gaussian smearing, with a smearing width of 0.03 eV. The Wigner-Seitz radii for Nb and Cl were 1.270 Å and 1.111 Å respectively; and the *LAMBDA* parameter (which sets the weight with which the penalty terms of the constrained local moment approach enter into the total energy expression and the Hamiltonian) was set to 9. The simplified (rotationally invariant) approach to DFT+U introduced by Dudarev et al. [31] was used to incorporate the DFT+U formalism. A Hubbard potential of $U = 1$ eV was used on Niobium d orbitals to account for effective on-site Coulomb interactions. Our optimized structure yielded an Nb-Nb bond length of 2.8112 Å within an $Nb_3$ trimer. This is only 0.01% different from the experimental bond length of 2.8109 in Ref. [58, 59], although it is quite different from the 2.85 Å bond length in Ref. [179].

### *6.1.4 Strain Tuning*

We applied biaxial strain in our DFT calculations by changing the $a$ and $b$ lattice vectors by the same percentage, and relaxing atom positions before running self-consistent field calculations.

### *6.1.5 Phonon Dispersions*

We used VASP to perform Density Functional Perturbation Theory (DFPT) calculations for the monolayer unit cell with SOC, with unconstrained Nb magnetic moments starting in the $(1, 0, 0)$ direction. Otherwise, the calculation details are as described in Sec. 6.1.3.

## *6.2 Spin Hamiltonian*

For the model we consider in this work, which includes anisotropies allowed by SOC and extended-neighbor interactions, the corresponding generalized Heisenberg-like spin Hamiltonian on the triangular lattice (see Fig. 5.2) becomes:

$$H = \sum_{i<j} \mathbf{S}_i \cdot J_{ij}^k \cdot \mathbf{S}_j + \sum_i A_i (S_i^z)^2 \tag{6.9}$$

where $k = 1, 2, 3$ corresponds to nearest-neighbor (NN), second-nearest-neighbor (2NN) and third-nearest-neighbor (3NN) pairs respectively. We use the index $k$ to make explicit the usual $J^1$, $J^2$,

$J^3$ notation for NN–3NN couplings. $\mathbf{S}_i = (S_i^x, S_i^y, S_i^z)$ represents the spin-1/2 operator at site $i$. $J_{ij}^k$ is the anisotropic exchange interaction between spins at sites $i$ and $j$, and $A_i$ is the single-ion anisotropy constant at site $i$. We assume this form of the single-ion anisotropy contribution to the Hamiltonian due to the system's easy-plane anisotropy that we numerically determined. Otherwise, we would have the general form [175]:

$$A_{i,xx}(S_i^x)^2 + A_{i,yy}(S_i^y)^2 + A_{i,zz}(S_i^z)^2 + 2A_{i,xy}S_i^xS_i^y + 2A_{i,xz}S_i^xS_i^z + 2A_{i,yz}S_i^yS_i^z.$$

In our case, we have $A_i(S^z)^2 \equiv (A_{i,zz} - A_{i,xx})(S_i^z)^2$.

We note that, to the best of our knowledge, the complete Hamiltonian in Eq. (6.9), including anisotropic exchange, DMI, and single-ion anisotropy up to third-nearest neighbors, has not been systematically explored in previous studies of spin-1/2 triangular-lattice systems. Earlier works have typically considered simplified models, such as isotropic or XXZ-type exchanges, sometimes including DMI or up to only second-nearest-neighbor interactions, within limited parameter regimes [9,50,51,68,149,168]. By using the full Hamiltonian, we can capture the combined influence of SOC-induced anisotropies and extended-neighbor couplings on the competition between ferromagnetic and antiferromagnetic correlations, the emergence of noncollinear spin textures, and possible chiral ground states, which cannot always be accessed within the simplified forms.

### *6.3 4-state Energy Mapping Analysis*

To investigate magnetic properties, a common strategy is to calculate magnetic anisotropy parameters using test cases that differ in how spins are assigned to atoms. The 4-state energy mapping formalism has proven to be quite powerful in calculating these parameters [150, 174, 175]. It can provide close agreement to experiment depending on the accuracy of the underlying *ab initio* calculations. It also offers a comprehensive consideration of interactions (e.g., including anisotropic exchange), and reduced ambiguity when dealing with spin configurations with near-degenerate energy levels (compared to two-state approaches and fitting methods, for instance). It is also simpler and more efficient to implement compared to Green's function and random phase approximation (RPA) methods, and is particularly well-suited to analyzing magnetic order.

Recall our Hamiltonian Eq. (6.9) (replicated below):

$$H = \sum_{i<j} \mathbf{S}_i \cdot J_{ij}^k \cdot \mathbf{S}_j + \sum_i A_i (S_i^z)^2 \tag{6.10}$$

where $k = 1, 2, 3$ corresponds to nearest-neighbor (NN), second-nearest-neighbor (2NN) and third-nearest-neighbor (3NN) pairs respectively. $\mathbf{S}_i = (S_i^x, S_i^y, S_i^z)$ represents the spin-1/2 operator at site $i$. $J_{ij}^k$ is the anisotropic exchange interaction between spins at sites $i$ and $j$ of form (using a Cartesian frame of reference, and ignoring the superscript $k = 1, 2, 3$ for brevity):

$$J = \begin{bmatrix} J_{xx} & J_{xy} & J_{xz} \\ J_{yx} & J_{yy} & J_{yz} \\ J_{zx} & J_{zy} & J_{zz} \end{bmatrix}, \tag{6.11}$$

and $A_i$ is the single-ion anisotropy constant at site $i$. Note that we can get the components of the Dzyaloshinskii–Moriya interaction (DMI) vectors from $J_{ij}^k$, i.e., $D^k = (D_x^k, D_y^k, D_z^k)$, in a Cartesian frame of reference as:

$$\begin{aligned} D_x^k &= \tfrac{1}{2}\big(J_{yz}^k - J_{zy}^k\big), \\ D_y^k &= \tfrac{1}{2}\big(J_{zx}^k - J_{xz}^k\big), \\ D_z^k &= \tfrac{1}{2}\big(J_{xy}^k - J_{yx}^k\big). \end{aligned} \tag{6.12}$$

The general idea behind the 4-state energy mapping technique is that, for each component in Eq. (6.10) (e.g., $J_{12}^{xz}$), we calculate the energies of 4 different spin configurations, and combine them in a way that isolates the contribution of the component. In this notation, the superscript now indicates the Cartesian component (e.g., $xz$) instead of which neighbor hopping it is (e.g., $1, 2, 3$).

The anisotropic exchange constants $J_{ij}$ between two magnetic sites $i$ and $j$ along directions $\alpha$ and $\beta$ can be obtained by combining energies from four specific spin arrangements:

$$J_{ij}^{\alpha\beta} = \frac{E_1 + E_4 - E_2 - E_3}{4S^2}. \tag{6.13}$$

Here, $i$ and $j$ index different lattice sites; $\alpha, \beta$ are two distinct Cartesian axes; and $E_1 \ldots E_4$ are the total energies of the following spin configurations: the moments $S_i$ and $S_j$ point along $\pm\alpha$ and

$\pm\beta$, while all other spins $S_{\text{other}\neq i,j}$ lie along the remaining axis.

For example, to isolate $J_{12}^{xz}$, one uses these four states (all other spins along $y$):

$$\begin{aligned}
&\text{State 1:} \quad \mathbf{S}_1 = (+S, 0, 0), \quad \mathbf{S}_2 = (0, 0, +S),\\
&\text{State 2:} \quad \mathbf{S}_1 = (+S, 0, 0), \quad \mathbf{S}_2 = (0, 0, -S),\\
&\text{State 3:} \quad \mathbf{S}_1 = (-S, 0, 0), \quad \mathbf{S}_2 = (0, 0, +S),\\
&\text{State 4:} \quad \mathbf{S}_1 = (-S, 0, 0), \quad \mathbf{S}_2 = (0, 0, -S),
\end{aligned}$$

and all others $\mathbf{S}_{k\neq 1,2} = (0, +S, 0)$ or $\mathbf{S}_{k\neq 1,2} = (0, -S, 0)$ depending on the low energy state. These give four energies:

$$\begin{aligned}
E_1 &= S\,J_{12}^{xz}\,S + \sum_{j\neq 2} S\,J_{1j}^{xy}\,S + \sum_{i\neq 1} S\,J_{i2}^{yz}\,S + \sum_{i\neq 1, j\neq 2} S\,J_{ij}^{yy}\,S + S\,A_{11}^{xx}\,S + S\,A_{22}^{zz}\,S + \sum_{i\neq 1,2} S\,A_{ii}^{yy}\,S,\\
E_2 &= -S\,J_{12}^{xz}\,S + \sum_{j\neq 2} S\,J_{1j}^{xy}\,S - \sum_{i\neq 1} S\,J_{i2}^{yz}\,S + \sum_{i\neq 1, j\neq 2} S\,J_{ij}^{yy}\,S + S\,A_{11}^{xx}\,S + S\,A_{22}^{zz}\,S + \sum_{i\neq 1,2} S\,A_{ii}^{yy}\,S,\\
E_3 &= -S\,J_{12}^{xz}\,S - \sum_{j\neq 2} S\,J_{1j}^{xy}\,S + \sum_{i\neq 1} S\,J_{i2}^{yz}\,S + \sum_{i\neq 1, j\neq 2} S\,J_{ij}^{yy}\,S + S\,A_{11}^{xx}\,S + S\,A_{22}^{zz}\,S + \sum_{i\neq 1,2} S\,A_{ii}^{yy}\,S,\\
E_4 &= S\,J_{12}^{xz}\,S - \sum_{j\neq 2} S\,J_{1j}^{xy}\,S - \sum_{i\neq 1} S\,J_{i2}^{yz}\,S + \sum_{i\neq 1, j\neq 2} S\,J_{ij}^{yy}\,S + S\,A_{11}^{xx}\,S + S\,A_{22}^{zz}\,S + \sum_{i\neq 1,2} S\,A_{ii}^{yy}\,S.
\end{aligned}$$

Combining these,

$$E_1 + E_4 - E_2 - E_3 = 4S^2\,J_{12}^{xz},$$

so indeed

$$J_{12}^{xz} = \frac{E_1 + E_4 - E_2 - E_3}{4S^2}. \tag{6.14}$$

The off-diagonal single-ion anisotropy components ($\alpha \neq \beta$) at site $i$ can be written as

$$A_{ii}^{\alpha\beta} = \frac{E_1 + E_4 - E_2 - E_3}{4S^2},$$

where $\alpha, \beta \in \{x, y, z\}$ are two distinct axes. Note that in this work, $A \equiv A_i \equiv A_{ii}$. Here $E_1 \ldots E_4$ are the total energies of the four spin orientations in which the moment $\mathbf{S}_i$ lies in the $\alpha\beta$ plane at angles of

$$(+\alpha, +\beta), \quad (-\alpha, +\beta), \quad (+\alpha, -\beta), \quad (-\alpha, -\beta),$$

each separated by 45°, while every other spin $\mathbf{S}_{\text{other}\neq i}$ is fixed along the remaining Cartesian axis.

For the diagonal anisotropy terms ($\alpha = \beta$) one forms the difference between the $\alpha\alpha$ and $xx$ components:

$$A_{ii}^{\alpha\alpha} - A_{ii}^{xx} = \frac{E_1 + E_2 - E_3 - E_4}{2S^2}, \quad \alpha \in \{y, z\}.$$

In this case $E_1 \ldots E_4$ are the energies with $\mathbf{S}_i$ pointing along $\pm\alpha$ and $\pm x$, and all other spins orthogonal to both $\alpha$ and $x$.

In a two-dimensional crystal that has three-, four-, or six-fold rotational symmetry, the sign of

$$A = A_{zz} - A_{xx},$$

which appears in Eq. (6.10), determines the easy-axis orientation: $A > 0$ for easy-plane anisotropy; $A < 0$ for out-of-plane anisotropy; and $A = A_0 = 0$ for the isotropic case, where $A_{xx} = A_{yy} = A_{zz} = A$. In the isotropic limit the single-ion term reduces to a constant $A_0\, S^2$ in the Heisenberg Hamiltonian and does not affect its spectrum.

The above exposition is derived from Ref. [150]. The formulae for almost all parameters (except $J_{\alpha\beta}, \alpha \neq \beta$) are explicitly listed in Ref. [175] (which should be followed with caution, following the subtleties discussed in Ref. [150]).

In our calculations, we used $S = 1/2$. We also used the trimer pairs indicated by arrows in Fig. 5.2. The magnetic parameters between different trimer pairs will differ by rotations of the exchange matrices Eq. (7.2); for instance, by 60° for adjacent NN trimer pairs. In the DFT calculations, Nb atom in a $Nb_3$ trimer is assigned the same magnetic moment, to correspond to the desired moment of a triangle vertex point. We caution the reader that since we used a $4 \times 4 \times 1$ supercell, we are not excluding interactions between periodic images when calculating magnetic anisotropy parameters between third-nearest-neighbors (i.e., $J_{ij}^3$). So, we deviate from the standard 4-state energy mapping technique in the 3NN case by accounting for this change in coordination number by dividing all computed $J_{ij}^3$ by 2 since each interaction occurs twice for this choice of supercell. A $5 \times 5 \times 1$ (or larger) supercell would have mitigated this issue. However, we could only converge our calculations for the collinear Heisenberg case with a $5 \times 5 \times 1$ supercell despite experimenting with a wide range

of *LAMBDA* and Wigner-Seitz radii. Despite this, we confirm that the isotropic Heisenberg $J^4$ from 4NN interactions is negligible using the collinear case. This justifies truncating interactions past 3NN interactions even using the 4-state mapping method. This is consistent with other works like Ref. [112] considering interactions only until 3NN, and our own spin-spiral calculations mapping to the spin-1/2 Heisenberg model for the case without SOC (which gave $J^4 = 0.01$ meV).

## *6.4 Curie-Weiss Law and Monte Carlo Simulations for Susceptibility*

### *6.4.1 Curie-Weiss Law*

The DFT-derived magnetic parameters were used to calculate the magnetic susceptibility using Monte Carlo simulations, and used with the Curie-Weiss law to classify the magnetic correlations. The Curie-Weiss law describes the magnetic susceptibility $\chi_d$ (in $d = x, y, z$ directions) of antiferromagnetic (AFM) and ferromagnetic (FM) materials above their respective critical temperatures (Néel temperature $T_N$ for antiferromagnets, and Curie temperature $T_C$ for ferromagnets):

$$\frac{1}{\chi_d} = \frac{T - \theta_d}{C}. \tag{6.15}$$

Above, we have the temperature $T$, Curie constant $C$ and Weiss temperature $\theta_d$. $\theta_d$ is typically negative for AFM correlations, 0 for paramagnetic (PM) correlations, and positive for FM correlations [123]. Although anisotropy, which is present in this work, may suppress long-range magnetic order, the sign and magnitude of $\theta_d$ still reflect the presence of local magnetic correlations.

### *6.4.2 Atomistic Monte Carlo Simulations*

We use classical Monte Carlo (MC) sampling of a spin Hamiltonian to predict magnetic ordering temperatures. The open-source package VAMPIRE 6.0 [33] implements this approach on an atomistic lattice. The spin Hamiltonian defined in VAMPIRE can be mapped to Eq. (6.9) up to sign.

In the Metropolis MC algorithm each spin is randomly perturbed and accepted with probability

$$P = \min\big(1, \exp[-\Delta E/(k_B T)]\big),$$

where $\Delta E$ is the energy change of the trial move, $k_B$ is Boltzmann's constant and $T$ the temperature. After equilibration, thermal averages of the magnetisation

$$\mathbf{M} = \sum_i \mathbf{S}_i$$

are collected over many MC sweeps. The magnetic susceptibility along the $z$-axis, for instance, is obtained from its fluctuations via

$$\chi_z(T) = \frac{\langle M_z^2 \rangle - \langle M_z \rangle^2}{k_B T\, V},$$

where $V$ is the sample volume. The Curie temperature $T_C$ is identified by the peak in $\chi_z(T)$.

Our first-principles calculations supply the tensors $J_{ij}^{\alpha\beta}$ and single-ion anisotropy $A$ together with the crystal structure to VAMPIRE. The code builds a periodic supercell, reads in these parameters, and carries out MC sampling across a temperature grid to map out $M(T)$ and $\chi(T)$.

We employed a 2D triangular lattice of size $100 \times 100$ nm, with periodicity in the x and y directions. This yields 25628 atoms for the unstrained structure, 27234 atoms for the $-3\%$ biaxial strained structure, and 27900 atoms for the $-4\%$ biaxial strained structure.

We modeled the triangular lattice in VAMPIRE using a 2D rectangular 'unit cell' of dimensions $a \times a\sqrt{3} \times 1000$ (for lattice vector $a$ and 'vacuum spacing' 1000), with two $Nb_3$ 'atoms' placed at $(0.25, 0.75, 0)$ and $(0.75, 0.25, 0)$ in fractional coordinates. When specifying anisotropic exchange matrices $J$ Eq. (7.2), we ensured that $J$ calculated for the bonds indicated in Fig. 5.2 are appropriately rotated in the 2D plane to account for the other bonds' orientations. For instance, the NN bond immediately clockwise to the NN bond indicated in Fig. 5.2 would have the same $J$, except rotated clockwise by $60°$.

We used temperature increments of $0.2\ K$, $2.5 \times 10^6$ equilibration time steps, and $2.5 \times 10^6$ loop time steps. We additionally assigned the initial spins to be in random directions.

### *6.4.3 Fitting Susceptibility to Curie-Weiss Law*

Due to the system's anisotropy, we do not expect $\chi_d$ to always be the same for different $d$. $\theta_d$ can be easily found by fitting the linear portion of $\chi_d^{-1}$ vs. $T$ data to a line, and calculating $T$ at which $\chi_d^{-1} = 0$. This is simply the negative of the vertical intercept $b$ divided by the gradient $m$: $\theta_d = -b/m$. The propagated uncertainty $\sigma_\theta$ of $\theta_d$ (without the small covariance term) is calculated using

$$\sigma_\theta \approx \sqrt{\left(\frac{\sigma_b}{m}\right)^2 + \left(\frac{b\sigma_m}{m^2}\right)^2},$$

where $\sigma_b$ is the standard error of $b$, and $\sigma_m$ is the standard error of the $m$. $C$ in Eq. (6.15) is the inverse of the gradient, and then the effective magnetic moment is $\mu_{\text{eff}} = \sqrt{8C}\mu_B$ (for the Bohr magneton $\mu_B$). For a spin-1/2 moment, we expect $\mu_{\text{eff}} \approx 1.73\mu_B$ [123].

When fitting our data to a line, we used the data only above 50 $K$, in order to ensure we are within the paramagnetic region for which the Curie-Weiss law is applicable, well above the kinks in susceptibility that arise at or below $\sim$20 $K$ in all our cases (see Fig. 7.1).

# Chapter 7

# RESULTS

## *7.1 Antiferromagnetic Correlations*

We use the methods in Chapter 6: DFT+U+SOC calculations were performed as outlined in Sec. 6.1. The spin Hamiltonian in Sec. 6.2 was used, along with the 4-state energy mapping technique in Sec. 6.3, to extract our magnetic parameters.

For the triangle vertex pairs illustrated in Fig. 5.2, we calculated the following (in units of meV):

$$J^1 = \begin{bmatrix} 1.49 & -0.15 & 0.89 \\ 0.15 & 1.59 & -0.01 \\ -0.89 & -0.01 & 1.47 \end{bmatrix}, J^2 = \begin{bmatrix} 0.96 & 0.00 & 0.04 \\ 0.00 & 0.97 & -0.02 \\ -0.04 & 0.02 & 0.95 \end{bmatrix}$$
$$J^3 = \begin{bmatrix} -0.73 & 0.00 & 0.00 \\ 0.00 & -0.74 & 0.00 \\ 0.00 & 0.00 & -0.73 \end{bmatrix} \tag{7.1}$$

where the anisotropic exchange $J^k$ is (using a Cartesian frame of reference, and ignoring the superscript $k = 1, 2, 3$ for brevity):

$$J = \begin{bmatrix} J_{xx} & J_{xy} & J_{xz} \\ J_{yx} & J_{yy} & J_{yz} \\ J_{zx} & J_{zy} & J_{zz} \end{bmatrix}. \tag{7.2}$$

The single-ion anisotropy constant was $A = 0.56$ meV. The DMI vector $\mathbf{D}^k = (D_x, D_y, D_z)$ was calculated to be $\mathbf{D}^1 = (0, -0.89, -0.15)$ meV, $\mathbf{D}^2 = (-0.02, -0.04, 0)$ meV, and $\mathbf{D}^3 = (0, 0, 0)$ meV. Our values are accurate up to 2 decimal places in meV. Using the convention dictated by Eq. (6.9), $J^k_{mn} > 0$ is an AFM interaction (and $J^k_{mn} < 0$ is FM), for $m, n$ being $x, y, z$. $A > 0$ implies easy-plane anisotropy.

Notice that most of the nonzero components of $J^1$ and $J^2$ are $> 0$, suggesting that they are antiferromagnetic. Indeed, using our classical Monte Carlo calculations outlined in Sec. 6.4, we found the Weiss temperatures

$$(\theta_x, \theta_y, \theta_z) = (-46.98 \pm 0.50, -46.87 \pm 0.50, -48.75 \pm 0.51)\ K.$$

The susceptibility data used to calculate $\theta_d$ is given in Fig. 7.1 and Fig. 7.2. In all cases, we obtained an effective moment $\mu_{\text{eff}} \approx 1.77\,\mu_B$, corresponding to a Landé $g$-factor of $\approx 2.04$, which is in good agreement with the expected value of $1.73\,\mu_B$ for a spin-1/2 system ($g \approx 2$). These $\theta_d$ compare well with reported values of isotropic $\theta$ from Curie-Weiss fittings of susceptibility from DFT and experimental single crystal and powder data. These $\theta$ fall within the range of $-70.1 < \theta < -13.1$ $K$ [48, 58, 59, 99, 112, 133, 154, 160, 201]. This is with the exception of the reported ferromagnetic Weiss temperatures of $+15$ $K$ (from single crystals) [76] and $+31$ $K$ (from DFT) [66].

Since all our $\theta_d < 0$, we have local AFM correlations. The system's clear antiferromagnetism suggests that it could be frustrated due to the triangular lattice structure, as an AFM configuration cannot be fully satisfied in such a geometry. We support this claim by calculating the frustration index $f$ [143]:

$$f = -\frac{\theta_d}{T_N}.$$

Using the $T_N$ values in Fig. 7.1 (i.e., $T_N \sim 20.2 \pm 0.5$ $K$), we have $(f_x, f_y, f_z) \sim (2.3, 2.3, 2.4) \pm 0.1$, which indicates frustration since $f > 1$. This frustration may be a stepping stone towards realizing exotic magnetic phenomena, such as quantum spin liquids.

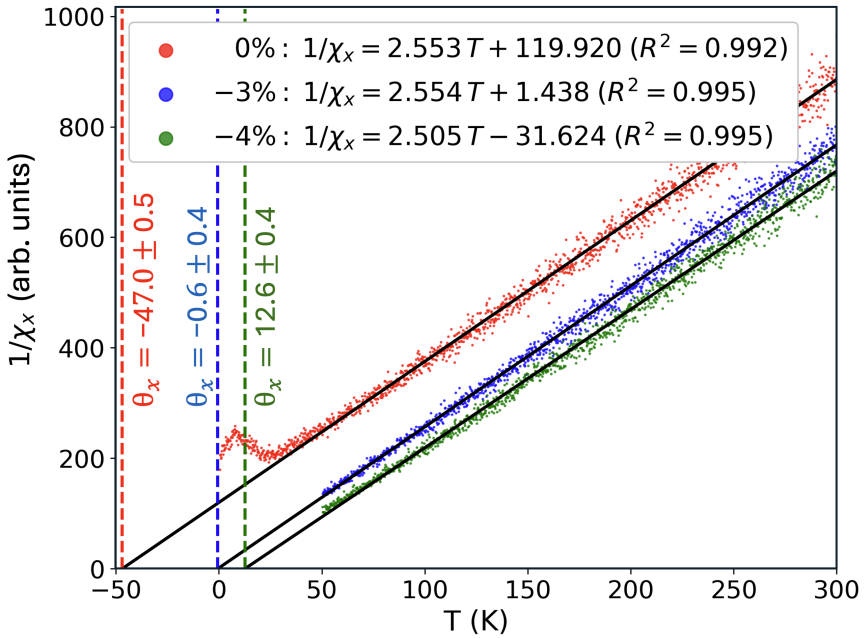


Figure 7.1: Inverse susceptibility $1/\chi_d$ (arb. units) vs. temperature $T(K)$ in the $d = x$-direction for 0% (unstrained), $-3\%$, and $-4\%$ biaxial strain. Data from Monte Carlo simulations are shown as dots, and the black lines are linear fit using data from $50 \leq T \leq 300$ $K$. We chose this range to ensure that we are within the paramagnetic region for which the Curie-Weiss law applies, well above any kinks in susceptibility. In all of our cases, these kinks occur at or below $\sim 20$ $K$. For 0%, they occur at $T_N \sim 20.2 \pm 0.5$ $K$ (same for $x, y, z$ within the range of error, as expected). For clarity in illustration, we show Monte Carlo data for only the range we use for fitting, with the exception of 0% strain in this figure, which exemplifies the aforementioned kinks. The equations of the linear fits are given in the inset in the top-left along with the coefficient of determination $R^2$. The $R^2$ values very close to 1 indicate that the fits explain the variance in data quite well. The Weiss temperature $\theta_d$ and uncertainty for each case is given alongside the vertical dashed line denoting the intersection of the linear fit with the $T$ axis.

### *7.1.1 Dzyaloshinskii–Moriya Interaction*

The DMI vectors extracted from Eq. (7.1) for the unstrained case are $\mathbf{D}^1 = (0, -0.89, -0.15)$ meV, $\mathbf{D}^2 = (-0.02, -0.04, 0)$ meV, and $\mathbf{D}^3 = (0, 0, 0)$ meV. $\mathbf{D}^1$ is visualized in Fig. 7.3.

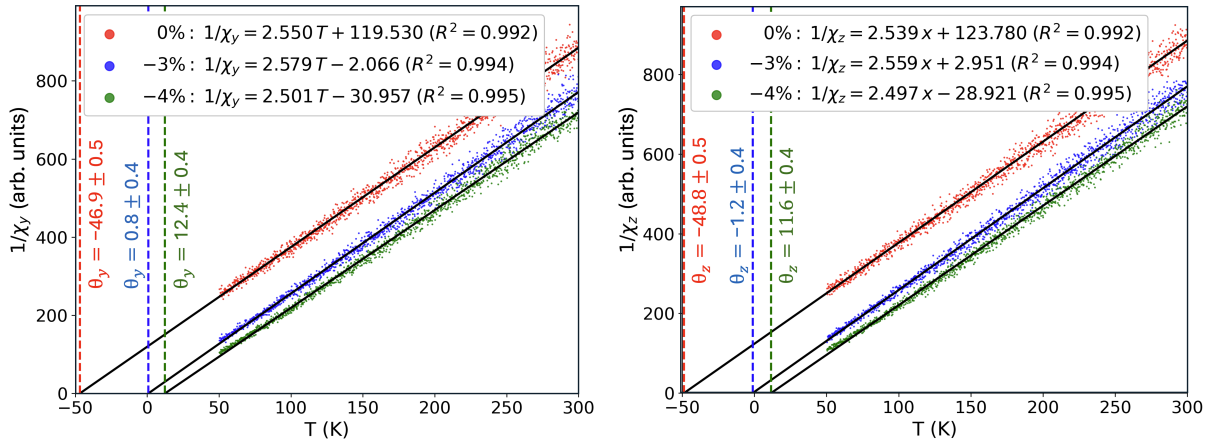


(a) $d = y$ (b) $d = z$

Figure 7.2: Inverse susceptibility $1/\chi_d$ (arb. units) vs. temperature $T(K)$ in the $d = y$ and $d = z$-directions for 0%, −3%, and −4% biaxial strain. Notation is as used in Fig. 7.1.

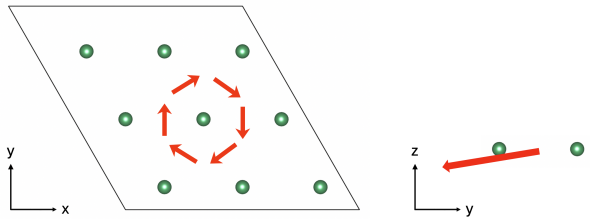


Figure 7.3: $\mathbf{D}^1$ for the unstrained case, visualized in the $xy$ (left) and $yz$ (right) planes. The $D_z$ component is −0.15 meV for all NN bonds.

We note that the calculated DMI vectors are consistent with the symmetry constraints imposed by the crystal (Moriya's rules) and, upon enforcing the full little group at the bond midpoint, reduce to $D_x^1 = 0$ for the NN bond in direction $(-1, 0, 0)$, $D_z^2 = 0$ for the 2NN bond in direction $(-1, 1, 0)$, and $D_x^3 = 0$ for the 3NN bond in direction $(-2, 0, 0)$, where the bond directions are expressed in the $(a, b, c)$ lattice basis (see Fig. 5.2).

The origin of these constraints can be understood by considering the site symmetry (little group) at each bond midpoint and applying Moriya's rules for the DMI. For the NN and 3NN bonds oriented along the $a$-axis, the relevant vertical mirror plane in P3m1 is perpendicular to the bond

and passes through its midpoint. This operation exchanges the two end sites, and the invariance of the antisymmetric exchange term $\mathbf{D}_{ij} \cdot (\mathbf{S}_i \times \mathbf{S}_j)$ requires the DMI vector to be invariant under this mirror. Because $\mathbf{D}$ transforms as an axial vector, the component along the bond direction changes sign under reflection and must vanish, hence $D_x^1 = D_x^3 = 0$. In contrast, for the 2NN bond along $(-1, 1, 0)$, the bond midpoint lies on both the perpendicular-bisector mirror (which exchanges the sites) and a mirror that contains the bond (which does not). The first again enforces $\mathbf{D} \perp$ bond; the second requires $\mathbf{D}$ to be odd under reflection, i.e. parallel to the in-plane normal of that mirror (perpendicular to the bond and within the plane), which eliminates the out-of-plane component: $D_z^2 = 0$.

Separately, we notice that the calculated DMI is comparable in magnitude to the components of the anisotropic exchange. The ratio between the Frobenius norm of $J^1$ ($|J^1| = 2.92$) and Euclidean norm of $\mathbf{D^1}$ ($|\mathbf{D^1}| = 0.90$) is $|\mathbf{D^1}|/|J^1| = 0.31$. This implies the strength of the DMI is relatively large, as the expected value of this ratio is on the order of 0.1 [121, 175]. We see that the role of the DMI may be significant, implying consequences such as the stabilization of non-collinear spin structures.

### *7.2 Strain Tuning between AFM, PM and FM correlations*

Given the potential for frustration in $Nb_3Cl_8$, we explore its magnetism further using biaxial strain tuning to better understand and manipulate its magnetic characteristics. We used the 4-state energy mapping technique to calculate magnetic anisotropy parameters as we applied compressive and tensile strain (Sec. 6.1.4).

For computational efficiency in generating exchange vs. strain diagrams, we used a slightly lower energy cutoff for the plane-wave basis set ($ENCUT = 350$ eV) compared to the cases that we explore using Monte Carlo calculations ($ENCUT = 400$ eV). For $ENCUT = 350$ eV, we got a single-ion anisotropy of 0.56 meV (same as with 400 eV), and the anisotropic exchange in Eq.

(7.3). These values are very close to the values for 400 eV given previously in Eq. (7.1):

$$J^1 = \begin{bmatrix} 1.44 & 0.16 & -0.88 \\ -0.16 & 1.52 & 0.00 \\ 0.88 & 0.00 & 1.40 \end{bmatrix}, J^2 = \begin{bmatrix} 0.96 & 0.00 & 0.04 \\ 0.00 & 0.96 & -0.04 \\ -0.04 & 0.04 & 0.96 \end{bmatrix}$$
$$J^3 = \begin{bmatrix} -0.72 & 0.00 & 0.00 \\ 0.00 & -0.72 & 0.00 \\ 0.00 & 0.00 & -0.72 \end{bmatrix} \tag{7.3}$$

The initial observation from these strain investigations is that the diagonal components of $J^1$ and $J^3$ Eq. (7.1) can change sign (and magnitude), indicating switching between antiferromagnetic and ferromagnetic correlations. This is illustrated in Fig. 7.4. NN interactions and single-ion anisotropy are presented in Fig. 7.5, and 2NN interactions in Fig. 7.6. Note that for all percentages of strain applied, the non-diagonal components of $J^3$ (and therefore DMI) are 0 up to our 2 decimal place accuracy.

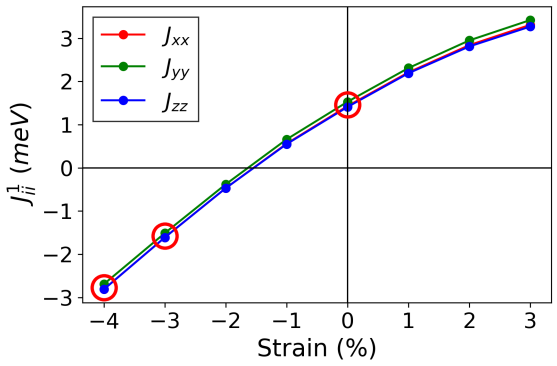


(a) Diagonal matrix elements of $J^1$ (meV) vs strain (%)

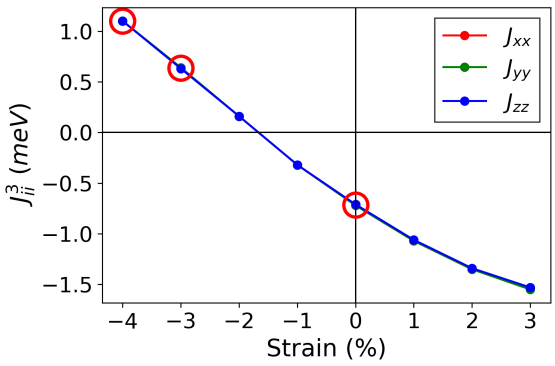


(b) Diagonal matrix elements of $J^3$ (meV) vs strain (%)

Figure 7.4: Diagonal matrix elements $J_{xx}, J_{yy}$ and $J_{zz}$ of $J^1$ and $J^3$, with respect to strain (horizontal axis). Note that some of the $J_{xx}, J_{yy}, J_{zz}$ curves in each case heavily overlap with each other. The red circles highlight the three test cases explored in our Monte Carlo calculations: 0%, −3% and −4%.

To verify that the magnetic correlations can change, we used magnetic susceptibility data to

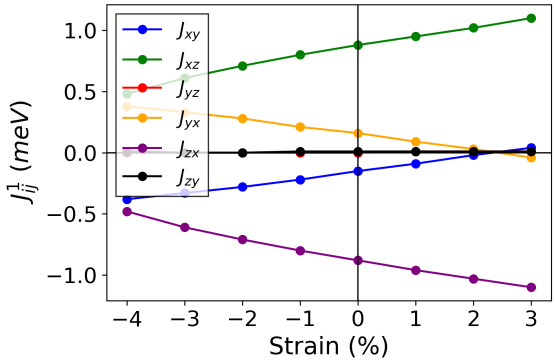


(a) Non-diagonal matrix elements of $J^1$ (meV) vs strain (%)

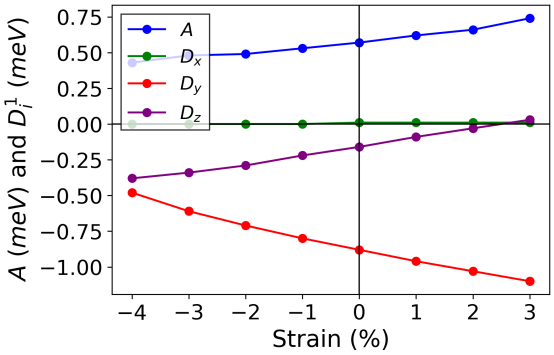


(b) Components of DMI vector $\mathbf{D}^1 = (D_x, D_y, D_z)$ (meV) and single-ion anisotropy $A$ (meV) vs strain (%)

Figure 7.5: Non-diagonal elements of $J^1$, DMI from NN interactions, and single-ion anisotropy, with respect to strain (horizontal axis).

explore three test cases: $0\%, -3\%$ and $-4\%$. For $0\%$ strain, we have the results in Eq. (7.1), and for $-3\%$, we got single-ion anisotropy $A = 0.46$ meV and, using the same convention in Eq. (7.2), the anisotropic exchange:

$$J^1 = \begin{bmatrix} -1.57 & -0.34 & 0.61 \\ 0.33 & -1.47 & 0.00 \\ -0.62 & 0.00 & -1.57 \end{bmatrix}, J^2 = \begin{bmatrix} 0.71 & 0.00 & 0.06 \\ 0.00 & 0.72 & -0.03 \\ -0.07 & 0.04 & 0.71 \end{bmatrix}$$
$$J^3 = \begin{bmatrix} 0.63 & 0.00 & 0.00 \\ 0.00 & 0.63 & 0.00 \\ 0.00 & 0.00 & 0.63 \end{bmatrix} \tag{7.4}$$

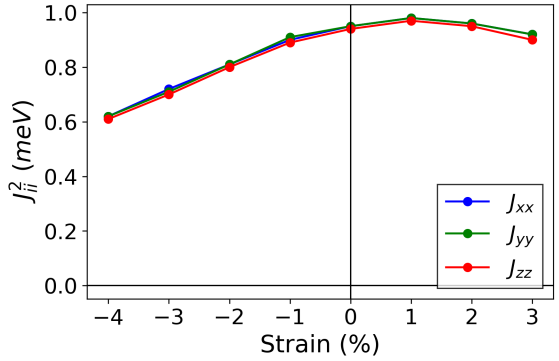


(a) Diagonal matrix elements of $J^2$ (meV) vs strain (%)

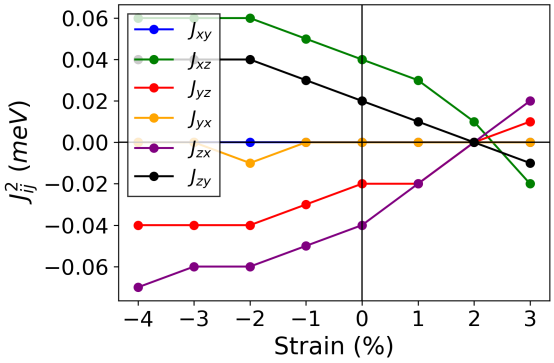


(b) Non-diagonal matrix elements of $J^2$ (meV) vs strain (%)

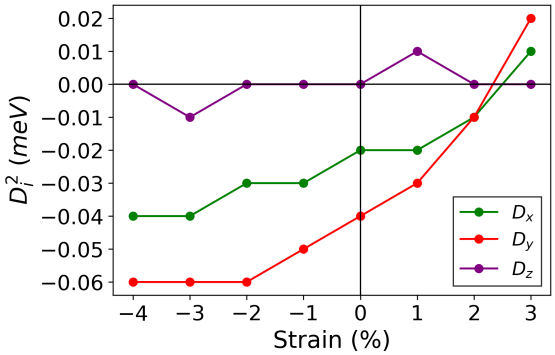


(c) Components of DMI vector $\mathbf{D}^2 = (D_x, D_y, D_z)$ (meV) vs strain (%)

Figure 7.6: Diagonal elements of $J^2$, non-diagonal elements of $J^2$, and DMI from 2NN interactions, with respect to strain (horizontal axis).

For $-4\%$ strain, we got single-ion anisotropy $A = 0.43$ meV and anisotropic exchange:

$$J^1 = \begin{bmatrix} -2.79 & -0.38 & 0.48 \\ 0.39 & -2.69 & 0.01 \\ -0.47 & 0.01 & -2.79 \end{bmatrix}, J^2 = \begin{bmatrix} 0.63 & 0.00 & 0.06 \\ 0.00 & 0.62 & -0.04 \\ -0.06 & 0.03 & 0.62 \end{bmatrix}$$
$$J^3 = \begin{bmatrix} 1.10 & 0.00 & 0.00 \\ 0.00 & 1.10 & 0.00 \\ 0.00 & 0.00 & 1.10 \end{bmatrix} \tag{7.5}$$

Using these parameters in Monte Carlo simulations, for $-3\%$ strain, we got

$$(\theta_x, \theta_y, \theta_z) = (-0.56 \pm 0.38, 0.80 \pm 0.41, -1.15 \pm 0.40),$$

and for $-4\%$ we got

$$(\theta_x, \theta_y, \theta_z) = (12.62 \pm 0.40, 12.38 \pm 0.39, 11.58 \pm 0.39).$$

See Fig. 7.1 and Fig. 7.2 for the Monte Carlo susceptibility and fitting data. Since $\theta_d$ for $-3\%$ strain are very close to 0, it is reasonable to infer that $\theta_d \sim 0$ and that we have PM correlations. For $-4\%$ strain, we clearly have FM correlations since $\theta_d > 0$.

### *7.2.1 Verifying Correlation Changes*

The above results on strain-dependent exchange interactions and short-range correlations do not themselves establish the presence or absence of long-range magnetic order in the ground state. To further assess the magnetic tendencies, we directly compared the total energies of representative magnetic configurations.

We perform *ab initio* supercell and spin-spiral calculations as consistency checks to show that the unstrained and $-4\%$ strained structures have energies close to the energies of standard commensurate 120° AFM and FM states, respectively. For the unstrained structure, this is consistent with recent works which suggest that monolayer $Nb_3Cl_8$ has a 120° AFM ground state [2, 55, 112]. However, due to the significant DMI we observe, it is reasonable to expect the true ground states to be incommensurate.

For the *ab initio* supercell calculations, we choose possible magnetic configurations that are commensurate with the supercell cell: FM, stripe (using a $2 \times 2$ supercell), and 120° order ($\sqrt{3} \times \sqrt{3}$ supercell). With SOC included, we tested several different spatial and orientational alignment of spins in each configuration (e.g., 120° with spins pointing inwards vs. outwards for a reference triangle; stripes along horizontal and vertical directions; and in-plane vs out-of-plane FM configurations). We found that for 0% strain, the 120° configurations yielded the lowest energy per unit cell, with stripe configurations being higher by about 0.39 meV per unit cell, and the FM con-

figurations being higher than 120° order by about 1.55 meV. In comparison, for −4% strain, the FM configurations have the lowest energy, with the 120° configurations being higher by about 2.05 meV per unit cell, and stripe configurations being higher than FM by about 2.45 meV. Thus, while genuinely incommensurate states are inaccessible in single-supercell calculations, the energetics of the accessible commensurate configurations point to ground-state order close to 120° AFM at 0% strain and FM at −4% strain.

Next, we perform additional calculations based on spin-spirals without SOC, following the approach of Ref. [112]. We performed spin-spiral calculations without SOC, because VASP's spin-spiral implementation uses the generalized Bloch theorem: Adding SOC couples spin and lattice degrees of freedom, and thereby breaks the spin-rotation invariance required for the spiral boundary conditions. Due to the lack of SOC, the results in this section are intended only as a qualitative reference and not as a replacement for the SOC-based results in the main text.

We computed the spin-spiral dispersion for the unstrained and −4% biaxial strained structures. The spiral energies were fitted to an isotropic spin-1/2 $J_1$–$J_2$–$J_3$–$J_4$ Heisenberg model of the following form (using notation consistent with Eq. (6.9)):

$$H = \sum_{i<j} J_{ij}^{k}\, \mathbf{S}_i \cdot \mathbf{S}_j,$$

from which excellent linear fits were obtained (see Fig. 7.7). For 0% strain the best fit parameters were

$$(J^1, J^2, J^3, J^4) = (0.99,\ 0.22,\ 0.35,\ 0.00)\ \text{meV},$$

and for −4% strain the parameters were

$$(J^1, J^2, J^3, J^4) = (-2.72,\ 0.27,\ 0.73,\ 0.00)\ \text{meV}.$$

The extracted exchange constants differ from those obtained from the 4-state mapping method because SOC is not included in the spin-spiral calculations and therefore the anisotropic contributions to the exchange constants are absent. However, in both cases, we still see dominant AFM $J^1$ for 0% strain, and dominant FM $J^1$ for −4% strain.

As seen in Fig. 7.7, for 0% strain, the minimum of the spin-spiral dispersion occurs at the $K$

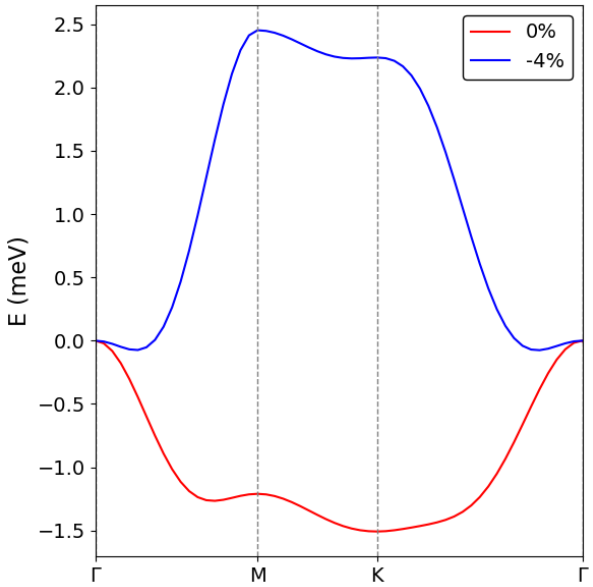


Figure 7.7: Spin-spiral energies as a function of ordering vector for 0% and −4% biaxial strain, with the energy at Γ set to 0.

point, which is consistent with 120° AFM order. For −4% strain, the minimum lies close to the Γ point (0.08 meV away from the energy at Γ, with the total energy variation between the maximum and minimum being 2.52 meV). This implies a tendency towards FM order. These trends agree qualitatively with the strain-tunable magnetic behavior demonstrated by the 4-state mapping and supercell calculations with SOC.

All these observations suggest that $Nb_3Cl_8$ exhibits a strain-tunable magnetic response, making it a promising material to explore short-range AFM, PM, and FM correlations for future applications.

### *7.2.2 Phonon Dispersions and Structural Stability*

We use phonon dispersions (Sec. 6.1.5) to show that our structures are stable for the $0, -3\%$ and $-4\%$ biaxial strained cases.

Indeed, we see from Fig. 7.8 that the phonon frequencies are positive and imply stable structures. Note that there is a small pocket of negative frequencies near Γ, with the minima of the negative frequencies being $\sim -0.27$ THz for 0%, $\sim -0.22$ THz for −3% and $\sim -0.21$ THz for −4%. These

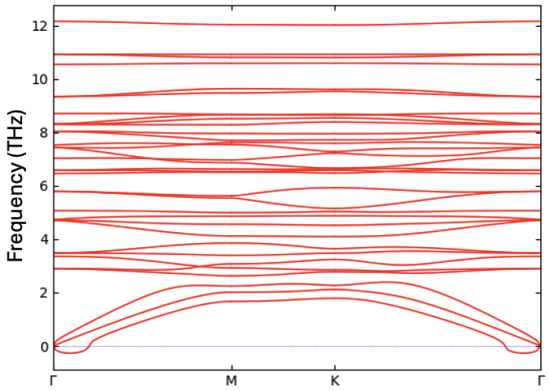


(a) Unstrained structure

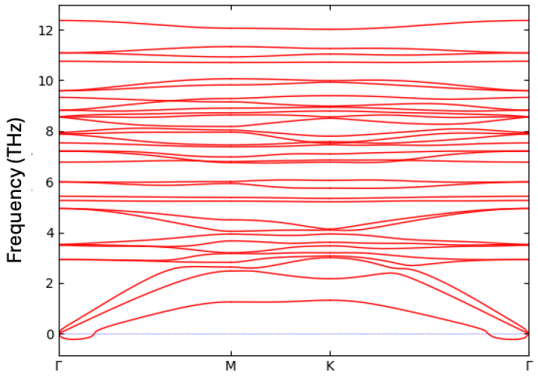


(b) −3% biaxial strained structure

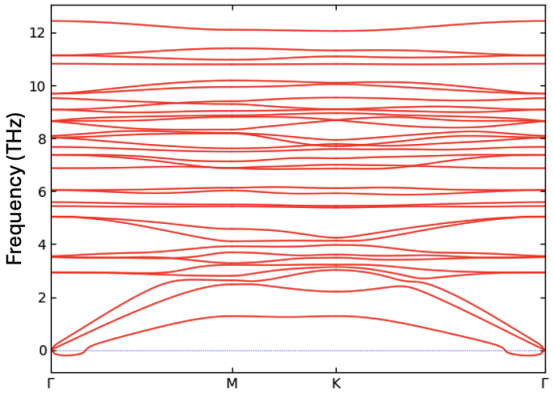


(c) −4% biaxial strained structure

Figure 7.8: Phonon dispersions.

small values lie within the $\sim -1$ THz threshold commonly attributed to numerical noise near the Γ point [97, 98], and is therefore not indicative of a true structural instability.

### *7.3 Discussion*

Our findings provide deeper insights into the magnetic behavior of $Nb_3Cl_8$. We showed that monolayer $Nb_3Cl_8$ may be magnetically frustrated. This result supports recent work that suggests exotic magnetic phenomena in $Nb_3Cl_8$. Even though our classical Monte Carlo calculations do not capture quantum fluctuations, the AFM interaction and frustration index $f > 1$ indicate the possi-

bility of $Nb_3Cl_8$ being a quantum spin liquid, due to the spin-1/2 nature of the system and the strong quantum fluctuations. These ground states are very exciting due to the wide array of potential applications in exploring fundamental quantum mechanics, quantum computing, spintronics, and the development of advanced materials with novel magnetic and electronic properties. We further showed that the short-range correlations may be tuned between AFM, PM and FM using strain, which is appealing due to the demand for controllable magnetic properties in quantum materials technologies. A potential next step would be to identify the role of the observed relatively-significant DMI, and confirm whether it can stabilize exotic non-collinear spin structures such as spin spirals or skyrmions. Further explorations could also involve establishing a comprehensive phase diagram for the system. By elucidating the role of magnetic anisotropy and extended interactions, our work paves the way for further theoretical and experimental studies aimed at harnessing the unique properties of $Nb_3Cl_8$ for applications in condensed matter research, device engineering, and beyond.

Thank you for your attention.

# BIBLIOGRAPHY


[1] Stefan Albrecht, Lucia Reining, Rodolfo Del Sole, and Giovanni Onida. Ab initio calculation of excitonic effects in the optical spectra of semiconductors. *Physical review letters*, 80(20):4510, 1998.

[2] Joost Aretz, Sergii Grytsiuk, Xiaojing Liu, Giovanna Feraco, Chrystalla Knekna, Muhammad Waseem, Zhiying Dan, Marco Bianchi, Philip Hofmann, Mazhar N Ali, et al. From strong to weak correlations in breathing-mode kagome van der waals materials: Nb _3(f, cl, br, i) _8 as a robust and versatile platform for many-body engineering. *arXiv preprint arXiv:2501.10320*, 2025.

[3] János K Asbóth, László Oroszlány, and András Pályi. A short course on topological insulators. *Lecture notes in physics*, 919:87, 2016.

[4] Leon Balents. Spin liquids in frustrated magnets. *nature*, 464(7286):199–208, 2010.

[5] Blake Barker, Jeffrey Humpherys, and Kevin Zumbrun. Stablab: A matlab-based numerical library for evans function computation, version 1.0. http://impact.byu.edu/stablab/, 2009. Online; accessed 20 November 2018.

[6] Lorin X Benedict, Eric L Shirley, and Robert B Bohn. Optical absorption of insulators and the electron-hole interaction: An ab initio calculation. *Physical review letters*, 80(20):4514, 1998.

[7] Michael Victor Berry. Quantal phase factors accompanying adiabatic changes. *Proceedings of the Royal Society of London. A. Mathematical and Physical Sciences*, 392(1802):45–57, 1984.

[8] Gennadiĭ Levikovich Bir, Grigoriĭ Ezekielevich Pikus, et al. *Symmetry and strain-induced effects in semiconductors*, volume 484. Wiley New York, 1974.

[9] RF Bishop and PHY Li. Spin-gap study of the spin-$\frac{1}{2}$ $j_1$–$j_2$ model on the triangular lattice. *arXiv preprint arXiv:1508.00414*, 2015.

[10] Peter E Blöchl. Projector augmented-wave method. *Physical review B*, 50(24):17953, 1994.

[11] Adrien Bolens and Naoto Nagaosa. Topological states on the breathing kagome lattice. *Physical Review B*, 99(16):165141, 2019.

[12] Max Born and W Heisenberg. Zur quantentheorie der molekeln. In *Original Scientific Papers Wissenschaftliche Originalarbeiten*, pages 216–246. Springer, 1985.

[13] A Bouhmouche, A Jabar, I Rhrissi, and R Moubah. Highly optical anisotropy, electronic and thermodynamic properties of the topological flat bands kagome nb3cl8. *Materials Science in Semiconductor Processing*, 175:108238, 2024.

[14] Robert W Boyd. *Nonlinear optics*. Academic press, 3rd edition, 2008.

[15] Barry Bradlyn, Luis Elcoro, Jennifer Cano, Maia G Vergniory, Zhijun Wang, Claudia Felser, Mois I Aroyo, and B Andrei Bernevig. Topological quantum chemistry. *Nature*, 547(7663):298–305, 2017.

[16] C Broholm, Robert J Cava, SA Kivelson, DG Nocera, MR Norman, and T Senthil. Quantum spin liquids. *Science*, 367(6475):eaay0668, 2020.

[17] Kenneth S Burch, David Mandrus, and Je-Geun Park. Magnetism in two-dimensional van der waals materials. *Nature*, 563(7729):47–52, 2018.

[18] Jiaqi Cai, Eric Anderson, Chong Wang, Xiaowei Zhang, Xiaoyu Liu, William Holtzmann, Yinong Zhang, Fengren Fan, Takashi Taniguchi, Kenji Watanabe, et al. Signatures of fractional quantum anomalous hall states in twisted mote$_2$. *Nature*, 622(7981):63–68, 2023.

[19] Dumitru Călugăru, Aaron Chew, Luis Elcoro, Yuanfeng Xu, Nicolas Regnault, Zhi-Da Song, and B Andrei Bernevig. General construction and topological classification of crystalline flat bands. *Nature Physics*, 18(2):185–189, 2022.

[20] Jinlyu Cao, HA Fertig, and Luis Brey. Quantum geometric exciton drift velocity. *Physical Review B*, 103(11):115422, 2021.

[21] Ting Cao, Meng Wu, and Steven G Louie. Unifying optical selection rules for excitons in two dimensions: Band topology and winding numbers. *Physical Review Letters*, 120(8):087402, 2018.

[22] David M Ceperley and Berni J Alder. Ground state of the electron gas by a stochastic method. *Physical review letters*, 45(7):566, 1980.

[23] Yu-Tzu Chang and Yang-Hao Chan. Diagrammatic approach to excitonic effects on nonlinear optical response. *Physical Review B*, 109(15):155437, 2024.

[24] Ran Cheng. Quantum geometric tensor (fubini-study metric) in simple quantum system: a pedagogical introduction. *arXiv preprint arXiv:1012.1337*, 2010.

[25] Junwei Chu, Yang Wang, Xuepeng Wang, Kai Hu, Gaofeng Rao, Chuanhui Gong, Chunchun Wu, Hao Hong, Xianfu Wang, Kaihui Liu, et al. 2d polarized materials: ferromagnetic, ferrovalley, ferroelectric materials, and related heterostructures. *Advanced Materials*, 33(5):2004469, 2021.

[26] Marvin L Cohen and Steven G Louie. *Fundamentals of condensed matter physics*. Cambridge University Press, 2016.

[27] Pierluigi Cudazzo, Lorenzo Sponza, Christine Giorgetti, Lucia Reining, Francesco Sottile, and Matteo Gatti. Exciton band structure in two-dimensional materials. *Phys. Rev. Lett.*, 116:066803, Feb 2016.

[28] Christian L Degen, Friedemann Reinhard, and Paola Cappellaro. Quantum sensing. *Reviews of modern physics*, 89(3):035002, 2017.

[29] Mildred S Dresselhaus, Gene Dresselhaus, and Ado Jorio. *Group theory: application to the physics of condensed matter*. Springer Science & Business Media, 2007.

[30] Jingyi Duan, Da-Shuai Ma, Run-Wu Zhang, Zeying Zhang, Chaoxi Cui, Wei Jiang, Zhi-Ming Yu, and Yugui Yao. Inventory of high-quality flat-band van der waals materials. *arXiv preprint arXiv:2204.00810*, 2022.

[31] Sergei L Dudarev, Gianluigi A Botton, Sergey Y Savrasov, CJ Humphreys, and Adrian P Sutton. Electron-energy-loss spectra and the structural stability of nickel oxide: An lsda+ u study. *Physical Review B*, 57(3):1505, 1998.

[32] Roger J Elliott. Intensity of optical absorption by excitons. *Physical Review*, 108(6):1384, 1957.

[33] Richard FL Evans, Weijia J Fan, Phanwadee Chureemart, Thomas A Ostler, Matthew OA Ellis, and Roy W Chantrell. Atomistic spin model simulations of magnetic nanomaterials. *Journal of Physics: Condensed Matter*, 26(10):103202, 2014.

[34] Motohiko Ezawa. Symmetry protected topological charge in symmetry broken phase: Spin-chern, spin-valley-chern and mirror-chern numbers. *Physics Letters A*, 378(16-17):1180–1184, 2014.

[35] Xiying Fan, Tianzhi Xia, Huahui Qiu, Qicheng Zhang, and Chunyin Qiu. Tracking valley topology with synthetic weyl paths. *Physical Review Letters*, 128(21):216403, 2022.

[36] Tharindu Fernando. Gauge-invariant optical selection rules for excitons. *Physica B: Condensed Matter*, 693:416402, 2024.

[37] Tharindu Fernando and Ting Cao. Strain-tunable magnetic correlations in spin liquid candidate $Nb_3Cl_8$. Under review.

[38] Tharindu Fernando and Ting Cao. Quantized interband topological index in two-dimensional systems. *Physical Review B*, 108(8):L081111, 2023.

[39] Tharindu Fernando et al. Phonon modes in $Nb_3Br_8$. Accepted by RSC Nanoscale.

[40] Tharindu Fernando et al. Phonon modes in $Nb_3TeCl_7$. In preparation.

[41] Eduardo Fradkin. *Field theories of condensed matter physics*. Cambridge University Press, 2013.

[42] Benjamin M Fregoso, Takahiro Morimoto, and Joel E Moore. Quantitative relationship between polarization differences and the zone-averaged shift photocurrent. *Physical Review B*, 96(7):075421, 2017.

[43] Michel Fruchart and David Carpentier. An introduction to topological insulators. *Comptes Rendus Physique*, 14(9-10):779–815, 2013.

[44] Liang Fu and Charles L Kane. Time reversal polarization and a z 2 adiabatic spin pump. *Physical Review B—Condensed Matter and Materials Physics*, 74(19):195312, 2006.

[45] Takahiro Fukui, Yasuhiro Hatsugai, and Hiroshi Suzuki. Chern numbers in discretized brillouin zone: Efficient method of computing (spin) hall conductances. *Journal of the Physical Society of Japan*, 74(6):1674–1677, 2005.

[46] Thomas Galvani, Fulvio Paleari, Henrique P. C. Miranda, Alejandro Molina-Sánchez, Ludger Wirtz, Sylvain Latil, Hakim Amara, and François Ducastelle. Excitons in boron nitride single layer. *Physical Review B*, 94(12):125303, 2016.

[47] Shiyuan Gao, Yufeng Liang, Catalin D Spataru, and Li Yang. Dynamical excitonic effects in doped two-dimensional semiconductors. *Nano letters*, 16(9):5568–5573, 2016.

[48] Shunye Gao, Shuai Zhang, Cuixiang Wang, Shaohua Yan, Xin Han, Xuecong Ji, Wei Tao, Jingtong Liu, Tiantian Wang, Shuaikang Yuan, et al. Discovery of a single-band mott insulator in a van der waals flat-band compound. *Physical Review X*, 13(4):041049, 2023.

[49] Paolo Giannozzi, Stefano Baroni, Nicola Bonini, Matteo Calandra, Roberto Car, Carlo Cavazzoni, Davide Ceresoli, Guido L Chiarotti, Matteo Cococcioni, Ismaila Dabo, et al. Quantum espresso: a modular and open-source software project for quantumsimulations of materials. *Journal of physics: Condensed matter*, 21(39):395502, 2009.

[50] Cecilie Glittum and Olav F Syljuåsen. Arc-shaped structure factor in the $j_1 - j_2 - j_3$ classical heisenberg model on the triangular lattice. *Physical Review B*, 104(18):184427, 2021.

[51] Shou-Shu Gong, Wei Zhu, J-X Zhu, Donna N Sheng, and Kun Yang. Global phase diagram and quantum spin liquids in a spin-1 2 triangular antiferromagnet. *Physical Review B*, 96(7):075116, 2017.

[52] RV Gorbachev, JCW Song, GL Yu, AV Kretinin, F Withers, Y Cao, A Mishchenko, IV Grigorieva, Konstantin S Novoselov, LS Levitov, et al. Detecting topological currents in graphene superlattices. *Science*, 346(6208):448–451, 2014.

[53] Christoph W Groth, Michael Wimmer, Anton R Akhmerov, and Xavier Waintal. Kwant: a software package for quantum transport. *New Journal of Physics*, 16(6):063065, 2014.

[54] Myrta Grüning and Claudio Attaccalite. Second harmonic generation in h-bn and $mos_2$ monolayers: Role of electron-hole interaction. *Physical Review B*, 89(8):081102, 2014.

[55] Sergii Grytsiuk, Mikhail I Katsnelson, Erik GCP van Loon, and Malte Rösner. Nb3cl8: a prototypical layered mott-hubbard insulator. *npj Quantum Materials*, 9(1):8, 2024.

[56] F Duncan M Haldane. Model for a quantum hall effect without landau levels: Condensed-matter realization of the" parity anomaly". *Physical Review Letters*, 61(18):2015, 1988.

[57] FDM Haldane. Berry curvature on the fermi surface: Anomalous hall effect as a topological fermi-liquid property. *Physical review letters*, 93(20):206602, 2004.

[58] Yuya Haraguchi, Chishiro Michioka, Manabu Ishikawa, Yoshiaki Nakano, Hideki Yamochi, Hiroaki Ueda, and Kazuyoshi Yoshimura. Magnetic–nonmagnetic phase transition with interlayer charge disproportionation of nb3 trimers in the cluster compound nb3cl8. *Inorganic Chemistry*, 56(6):3483–3488, 2017.

[59] Yuya Haraguchi and Kazuyoshi Yoshimura. Molecular orbital electronic instability in the van der waals kagome semiconductor nb _3 cl _8: Exploring future directions. *arXiv preprint arXiv:2407.19457*, 2024.

[60] M Zahid Hasan and Charles L Kane. Colloquium: topological insulators. *Reviews of Modern Physics*, 82(4):3045, 2010.

[61] Yasuhiro Hatsugai. Explicit gauge fixing for degenerate multiplets: A generic setup for topological orders. *Journal of the Physical Society of Japan*, 73(10):2604–2607, 2004.

[62] Pierre Hohenberg and Walter Kohn. Inhomogeneous electron gas. *Physical review*, 136(3B):B864, 1964.

[63] Tobias Holder, Daniel Kaplan, and Binghai Yan. Consequences of time-reversal-symmetry breaking in the light-matter interaction: Berry curvature, quantum metric, and diabatic motion. *Physical Review Research*, 2(3):033100, 2020.

[64] Jiayu Hu, Xuefeng Zhang, Cong Hu, Jian Sun, Xiaoqun Wang, Hai-Qing Lin, and Gang Li. Correlated flat bands and quantum spin liquid state in a cluster mott insulator. *Communications Physics*, 6(1):172, 2023.

[65] Dylan A Jeff, Favian Gonzalez, Kamal Harrison, Yuzhou Zhao, Tharindu Fernando, Sabin Regmi, Zhaoyu Liu, Humberto R Gutierrez, Madhab Neupane, Jihui Yang, et al. Raman study of layered breathing kagome lattice semiconductor nb3cl8. *2D Materials*, 10(4):045030, 2023.

[66] Junke Jiang, Qiuhua Liang, Ruishen Meng, Qun Yang, Chunjian Tan, Xiang Sun, and Xianping Chen. Exploration of new ferromagnetic, semiconducting and biocompatible nb 3 x 8 (x= cl, br or i) monolayers with considerable visible and infrared light absorption. *Nanoscale*, 9(9):2992–3001, 2017.

[67] Xue Jiang, Qinxi Liu, Jianpei Xing, Nanshu Liu, Yu Guo, Zhifeng Liu, and Jijun Zhao. Recent progress on 2d magnets: Fundamental mechanism, structural design and modification. *Applied Physics Reviews*, 8(3), 2021.

[68] Yi-Fan Jiang and Hong-Chen Jiang. Nature of quantum spin liquids of the s= 1 2 heisenberg antiferromagnet on the triangular lattice: A parallel dmrg study. *Physical Review B*, 107(14):L140411, 2023.

[69] Long Ju, Zhiwen Shi, Nityan Nair, Yinchuan Lv, Chenhao Jin, Jairo Velasco, Claudia Ojeda-Aristizabal, Hans A Bechtel, Michael C Martin, Alex Zettl, et al. Topological valley transport at bilayer graphene domain walls. *Nature*, 520(7549):650–655, 2015.

[70] Long Ju, Lei Wang, Ting Cao, Takashi Taniguchi, Kenji Watanabe, Steven G Louie, Farhan Rana, Jiwoong Park, James Hone, Feng Wang, et al. Tunable excitons in bilayer graphene. *Science*, 358(6365):907–910, 2017.

[71] Jeil Jung, Fan Zhang, Zhenhua Qiao, and Allan H MacDonald. Valley-hall kink and edge states in multilayer graphene. *Physical Review B*, 84(7):075418, 2011.

[72] Mingu Kang, Linda Ye, Shiang Fang, Jhih-Shih You, Abe Levitan, Minyong Han, Jorge I Facio, Chris Jozwiak, Aaron Bostwick, Eli Rotenberg, et al. Dirac fermions and flat bands in the ideal kagome metal fesn. *Nature materials*, 19(2):163–169, 2020.

[73] Tosio Kato. On the adiabatic theorem of quantum mechanics. *Journal of the Physical Society of Japan*, 5(6):435–439, 1950.

[74] Mahtab Khan, Naseem Ud Din, Dirk R Englund, and Michael N Leuenberger. Multiferroic dark excitonic mott insulator in the breathing-kagome lattice material nb _3 cl _8. *arXiv preprint arXiv:2412.13456*, 2024.

[75] Bum Jun Kim, Byung Joo Jeong, Seungbae Oh, Sudong Chae, Kyung Hwan Choi, Sitansu Sekhar Nanda, Tuqeer Nasir, Sang Hoon Lee, Kwan-Woo Kim, Hyung Kyu Lim, et al. Structural and electrical properties of nb3i8 layered crystal. *physica status solidi (RRL)–Rapid Research Letters*, 13(3):1800448, 2019.

[76] Jangwon Kim, Youjin Lee, Young Woo Choi, Taek Sun Jung, Suhan Son, Jonghyeon Kim, Hyoung Joon Choi, Je-Geun Park, and Jae Hoon Kim. Terahertz spectroscopy and dft analysis of phonon dynamics of the layered van der waals semiconductor nb3 x 8 (x= cl, i). *ACS omega*, 8(15):14190–14196, 2023.

[77] Sota Kitamura, Naoto Nagaosa, and Takahiro Morimoto. Nonreciprocal landau–zener tunneling. *Communications Physics*, 3(1):1–8, 2020.

[78] Stephan W Koch, Mackillo Kira, Galina Khitrova, and Hyatt M Gibbs. Semiconductor excitons in new light. *Nature materials*, 5(7):523–531, 2006.

[79] Walter Kohn and Lu Jeu Sham. Self-consistent equations including exchange and correlation effects. *Physical review*, 140(4A):A1133, 1965.

[80] Mikito Koshino and Edward McCann. Trigonal warping and berry's phase n $\pi$ in abc-stacked multilayer graphene. *Physical Review B*, 80(16):165409, 2009.

[81] Jaakko Koskelo, Giorgia Fugallo, Mikko Hakala, Matteo Gatti, Francesco Sottile, and Pierluigi Cudazzo. Excitons in van der waals materials: From monolayer to bulk hexagonal boron nitride. *Phys. Rev. B*, 95:035125, Jan 2017.

[82] G Kresse. Hafner, j1: Cas: 528: Dyak2cxkvfkrtl4% 3d: Ab initio molecular-dynamics simulation of the liquid-metal-amorphous-semiconductor transition in germanium. vol. 49. *Phys Rev B*, pages 14251–14269, 1994.

[83] Georg Kresse and J Furthmüller. Software vasp, vienna (1999). *Phys. Rev. B*, 54(11):169, 1996.

[84] Georg Kresse and Jürgen Furthmüller. Efficiency of ab-initio total energy calculations for metals and semiconductors using a plane-wave basis set. *Computational materials science*, 6(1):15–50, 1996.

[85] Georg Kresse and Jürgen Furthmüller. Efficient iterative schemes for ab initio total-energy calculations using a plane-wave basis set. *Physical review B*, 54(16):11169, 1996.

[86] Georg Kresse and Jürgen Hafner. Ab initio molecular dynamics for liquid metals. *Physical review B*, 47(1):558, 1993.

[87] Georg Kresse and Jürgen Hafner. Ab initio molecular-dynamics simulation of the liquid-metal–amorphous-semiconductor transition in germanium. *Physical Review B*, 49(20):14251, 1994.

[88] Georg Kresse and Daniel Joubert. From ultrasoft pseudopotentials to the projector augmented-wave method. *Physical review b*, 59(3):1758, 1999.

[89] Simone Latini, Enrico Ronca, Umberto De Giovannini, Hannes Hübener, and Angel Rubio. Cavity control of excitons in two-dimensional materials. *Nano letters*, 19(6):3473–3479, 2019.

[90] Bom Lee, Xiaojie Zhang, Jinsu Kang, Byung Joo Jeong, Sooheon Cho, Kyung Hwan Choi, Jiho Jeon, Sang Hoon Lee, Dahoon Kim, Yeong Hyeop Kim, et al. A negative photoconductivity photodetector based on two-dimensional nb 3 cl 8. *Nanoscale*, 16(43):20312–20318, 2024.

[91] Kevin Leung and K Birgitta Whaley. Electron-hole interactions in silicon nanocrystals. *Physical Review B*, 56(12):7455, 1997.

[92] Dongzhe Li, Shuo Li, Chengyong Zhong, and Junjie He. Tuning magnetism at the two-dimensional limit: A theoretical perspective. *Nanoscale*, 13(47):19812–19827, 2021.

[93] Jian Li, Ivar Martin, Markus Büttiker, and Alberto F Morpurgo. Topological origin of subgap conductance in insulating bilayer graphene. *Nature Physics*, 7(1):38–42, 2011.

[94] Jian Li, Alberto F Morpurgo, Markus Büttiker, and Ivar Martin. Marginality of bulk-edge correspondence for single-valley hamiltonians. *Physical Review B*, 82(24):245404, 2010.

[95] Jing Li, Ke Wang, Kenton J McFaul, Zachary Zern, Yafei Ren, Kenji Watanabe, Takashi Taniguchi, Zhenhua Qiao, and Jun Zhu. Gate-controlled topological conducting channels in bilayer graphene. *Nature Nanotechnology*, 11(12):1060–1065, 2016.

[96] Yongchang Li, Chang Liu, Guo-Dong Zhao, Tao Hu, and Wei Ren. Two-dimensional multiferroics in a breathing kagome lattice. *Physical Review B*, 104(6):L060405, 2021.

[97] Francesco Libbi, Nicola Bonini, and Nicola Marzari. Thermomechanical properties of honeycomb lattices from internal-coordinates potentials: the case of graphene and hexagonal boron nitride. *2D Materials*, 8(1):015026, 2020.

[98] Changpeng Lin, Samuel Poncé, and Nicola Marzari. General invariance and equilibrium conditions for lattice dynamics in 1d, 2d, and 3d materials. *npj Computational Materials*, 8(1):236, 2022.

[99] Bo Liu, Yongchao Zhang, Xin Han, Jianping Sun, Honglin Zhou, Chunhong Li, Jinguang Cheng, Shaohua Yan, Hechang Lei, Youguo Shi, et al. Possible quantum-spin-liquid state in van der waals cluster magnet nb3cl8. *Journal of Physics: Condensed Matter*, 36(15):155602, 2024.

[100] Gui-Bin Liu, Wen-Yu Shan, Yugui Yao, Wang Yao, and Di Xiao. Three-band tight-binding model for monolayers of group-vib transition metal dichalcogenides. *Physical Review B*, 88(8):085433, 2013.

[101] Hang Liu, Sheng Meng, and Feng Liu. Screening two-dimensional materials with topological flat bands. *Physical Review Materials*, 5(8):084203, 2021.

[102] Wanli Liu, Zhi Lin, ZD Wang, and Yan Chen. Generalized haldane models on laser-coupling optical lattices. *Scientific Reports*, 8(1):1–7, 2018.

[103] Zhonghao Liu, Man Li, Qi Wang, Guangwei Wang, Chenhaoping Wen, Kun Jiang, Xiangle Lu, Shichao Yan, Yaobo Huang, Dawei Shen, et al. Orbital-selective dirac fermions and extremely flat bands in frustrated kagome-lattice metal cosn. *Nature communications*, 11(1):4002, 2020.

[104] Per-Olov Löwdin. A note on the quantum-mechanical perturbation theory. *The Journal of Chemical Physics*, 19(11):1396–1401, 1951.

[105] Yan Lu, Haonan Wang, Xilong Xu, Li Wang, and Li Yang. Intrinsic magnetoelectric coupling induced by the flat bands in kagome van der waals multiferroic heterostructures. *Physical Review B*, 111(16):165410, 2025.

[106] Yixiang Lu, Kai Zhao, Tongyao Zhang, and Baojuan Dong. Bipolar nb3cl8 field effect transistors. *Magnetochemistry*, 10(6):43, 2024.

[107] Joaquin M Luttinger and Walter Kohn. Motion of electrons and holes in perturbed periodic fields. *Physical Review*, 97(4):869, 1955.

[108] Yu-Quan Ma. Euler characteristic number of the energy band and the reason for its non-integer values. *arXiv preprint arXiv:2001.05946*, 2020.

[109] SN Magonov, P Zoennchen, H Rotter, HJ Cantow, G Thiele, J Ren, and MH Whangbo. Scanning tunneling and atomic force microscopy study of layered transition metal halides nb3x8 (x= cl, br, i). *Journal of the American Chemical Society*, 115(6):2495–2503, 1993.

[110] Kin Fai Mak, Kathryn L McGill, Jiwoong Park, and Paul L McEuen. The valley hall effect in mos2 transistors. *Science*, 344(6191):1489–1492, 2014.

[111] Kin Fai Mak, Di Xiao, and Jie Shan. Light–valley interactions in 2d semiconductors. *Nature Photonics*, 12(8):451–460, 2018.

[112] John Mangeri, Varun R Pavizhakumari, and Thomas Olsen. Magnetoelectric behavior of breathing kagomé monolayers of $nb_3(cl,br,i)_8$ from first-principles calculations. *arXiv preprint arXiv:2411.04839*, 2024.

[113] Nicola Manini and Fabio Pistolesi. Off-diagonal geometric phases. *Physical Review Letters*, 85(15):3067, 2000.

[114] Ivar Martin, Ya M Blanter, and AF Morpurgo. Topological confinement in bilayer graphene. *Physical Review Letters*, 100(3):036804, 2008.

[115] MFC Martins Quintela, JCG Henriques, LGM Tenório, and NMR Peres. Theoretical methods for excitonic physics in 2d materials. *Physica Status Solidi (b)*, 259(10):2200097, 2022.

[116] II Mazin, Harald O Jeschke, Frank Lechermann, Hunpyo Lee, Mario Fink, Ronny Thomale, and Roser Valentí. Theoretical prediction of a strongly correlated dirac metal. *Nature communications*, 5(1):4261, 2014.

[117] Edward McCann and Vladimir I. Fal'ko. Landau-level degeneracy and quantum hall effect in a graphite bilayer. *Physical Review Letters*, 96(8):086805, 2006.

[118] P Mendels and AS Wills. Introduction to frustrated magnetism. *Springer Series in Solid-State Sciences*, 164, 2011.

[119] Albert Messiah. *Quantum mechanics: volume II*, volume 1. North-Holland Publishing Company Amsterdam, 1962.

[120] Koichi Momma and Fujio Izumi. Vesta: a three-dimensional visualization system for electronic and structural analysis. *Applied Crystallography*, 41(3):653–658, 2008.

[121] Tôru Moriya. Anisotropic superexchange interaction and weak ferromagnetism. *Physical review*, 120(1):91, 1960.

[122] Bohayra Mortazavi, Xiaoying Zhuang, and Timon Rabczuk. A first-principles study on the physical properties of two-dimensional nb3cl8, nb3br8 and nb3i8. *Applied Physics A*, 128(10):934, 2022.

[123] Sam Mugiraneza and Alannah M Hallas. Tutorial: a beginner's guide to interpreting magnetic susceptibility data with the curie-weiss law. *Communications Physics*, 5(1):95, 2022.

[124] N Mukunda, S Chaturvedi, R Simon, et al. Bargmann invariants and off-diagonal geometric phases for multilevel quantum systems: A unitary-group approach. *Physical Review A*, 65(1):012102, 2001.

[125] N Mukunda and R Simon. Quantum kinematic approach to the geometric phase. i. general formalism. *Annals of Physics*, 228(2):205–268, 1993.

[126] R Nakamura, D Takegami, K Fujinuma, M Nakamura, M Ferreira-Carvalho, A Melendez-Sans, M Yoshimura, K-D Tsuei, Y Haraguchi, H Aruga Katori, et al. Charge fluctuations in a cluster mott state: Hard x-ray photoemission study on a breathing kagome magnet nb 3 cl 8. *Physical Review B*, 110(8):L081109, 2024.

[127] AH Castro Neto, Francisco Guinea, Nuno MR Peres, Kostya S Novoselov, and Andre K Geim. The electronic properties of graphene. *Reviews of modern physics*, 81(1):109, 2009.

[128] Thomas Olsen, Simone Latini, Filip Rasmussen, and Kristian S Thygesen. Simple screened hydrogen model of excitons in two-dimensional materials. *Physical review letters*, 116(5):056401, 2016.

[129] Giovanni Onida, Lucia Reining, and Angel Rubio. Electronic excitations: density-functional versus many-body green's-function approaches. *Reviews of Modern Physics*, 74(2):601, 2002.

[130] Brenden R Ortiz, Samuel ML Teicher, Yong Hu, Julia L Zuo, Paul M Sarte, Emily C Schueller, AM Milinda Abeykoon, Matthew J Krogstad, Stephan Rosenkranz, Raymond Osborn, et al. Cs v 3 sb 5: Az 2 topological kagome metal with a superconducting ground state. *Physical Review Letters*, 125(24):247002, 2020.

[131] Hui Pan, Zhenshan Li, Cheng-Cheng Liu, Guobao Zhu, Zhenhua Qiao, and Yugui Yao. Valley-polarized quantum anomalous hall effect in silicene. *Physical review letters*, 112(10):106802, 2014.

[132] Cheol-Hwan Park and Steven G Louie. Tunable excitons in biased bilayer graphene. *Nano letters*, 10(2):426–431, 2010.

[133] Christopher M Pasco, Ismail El Baggari, Elisabeth Bianco, Lena F Kourkoutis, and Tyrel M McQueen. Tunable magnetic transition to a singlet ground state in a 2d van der waals layered trimerized kagomé magnet. *ACS nano*, 13(8):9457–9463, 2019.

[134] Thomas G Pedersen, Antti-Pekka Jauho, and Kjeld Pedersen. Optical response and excitons in gapped graphene. *Physical Review B*, 79(11):113406, 2009.

[135] Thomas Garm Pedersen. Intraband effects in excitonic second-harmonic generation. *Physical Review B*, 92(23):235432, 2015.

[136] John P Perdew, Kieron Burke, and Matthias Ernzerhof. Generalized gradient approximation made simple. *Physical review letters*, 77(18):3865, 1996.

[137] John P Perdew and Yue Wang. Accurate and simple analytic representation of the electron-gas correlation energy. *Physical review B*, 45(23):13244, 1992.

[138] John P Perdew and Alex Zunger. Self-interaction correction to density-functional approximations for many-electron systems. *Physical review B*, 23(10):5048, 1981.

[139] Zhenhua Qiao, Jeil Jung, Qian Niu, and Allan H MacDonald. Electronic highways in bilayer graphene. *Nano Letters*, 11(8):3453–3459, 2011.

[140] Zhenhua Qiao, Xiao Li, Wang-Kong Tse, Hua Jiang, Yugui Yao, and Qian Niu. Topological phases in gated bilayer graphene: Effects of rashba spin-orbit coupling and exchange field. *Physical Review B*, 87(12):125405, 2013.

[141] Diana Y Qiu, Felipe H da Jornada, and Steven G Louie. Screening and many-body effects in two-dimensional crystals: Monolayer $mos_2$. *Physical Review B*, 93(23):235435, 2016.

[142] MFC Martins Quintela and Thomas Garm Pedersen. Anisotropic linear and nonlinear excitonic optical properties of buckled monolayer semiconductors. *Physical Review B*, 107(23):235416, 2023.

[143] AP Ramirez. Strongly geometrically frustrated magnets. *Annual Review of Materials Science*, 24(1):453–480, 1994.

[144] Sabin Regmi, Tharindu Fernando, Yuzhou Zhao, Anup Pradhan Sakhya, Gyanendra Dhakal, Iftakhar Bin Elius, Hector Vazquez, Jonathan D Denlinger, Jihui Yang, Jiun-Haw Chu, et al. Spectroscopic evidence of flat bands in breathing kagome semiconductor nb3i8. *Communications Materials*, 3(1):100, 2022.

[145] Sabin Regmi, Anup Pradhan Sakhya, Tharindu Fernando, Yuzhou Zhao, Dylan Jeff, Milo Sprague, Favian Gonzalez, Iftakhar Bin Elius, Mazharul Islam Mondal, Nathan Valadez, et al. Observation of flat and weakly dispersing bands in the van der waals semiconductor nb3br8 with breathing kagome lattice. *Physical Review B*, 108(12):L121404, 2023.

[146] Nicolas Regnault, Yuanfeng Xu, Ming-Rui Li, Da-Shuai Ma, Milena Jovanovic, Ali Yazdani, Stuart SP Parkin, Claudia Felser, Leslie M Schoop, N Phuan Ong, et al. Catalogue of flat-band stoichiometric materials. *Nature*, 603(7903):824–828, 2022.

[147] Michael Rohlfing and Steven G Louie. Electron-hole excitations and optical spectra from first principles. *Physical Review B*, 62(8):4927, 2000.

[148] A Rycerz, J Tworzydło, and CWJ Beenakker. Valley filter and valley valve in graphene. *Nature Physics*, 3(3):172–175, 2007.

[149] SN Saadatmand, BJ Powell, and IP McCulloch. Phase diagram of the spin-1 2 triangular $j_1 - j_2$ heisenberg model on a three-leg cylinder. *Physical Review B*, 91(24):245119, 2015.

[150] D Šabani, Cihan Bacaksiz, and MV Milošević. Ab initio methodology for magnetic exchange parameters: Generic four-state energy mapping onto a heisenberg spin hamiltonian. *Physical Review B*, 102(1):014457, 2020.

[151] Kento Sasaki, Yuki Nakamura, Tokuyuki Teraji, Takashi Oka, and Kensuke Kobayashi. Demonstration of geometric diabatic control of quantum states. *Physical Review A*, 107(5):053113, 2023.

[152] Malte Selig, Gunnar Berghäuser, Marten Richter, Rudolf Bratschitsch, Andreas Knorr, and Ermin Malic. Dark and bright exciton formation, thermalization, and photoluminescence in monolayer transition metal dichalcogenides. *2D Materials*, 5(3):035017, 2018.

[153] Gordon W Semenoff, V Semenoff, and Fei Zhou. Domain walls in gapped graphene. *Physical Review Letters*, 101(8):087204, 2008.

[154] John P Sheckelton, Kemp W Plumb, Benjamin A Trump, Collin L Broholm, and Tyrel M McQueen. Rearrangement of van der waals stacking and formation of a singlet state at t= 90 k in a cluster magnet. *Inorganic Chemistry Frontiers*, 4(3):481–490, 2017.

[155] John Patrick Sheckelton. *Strongly correlated molecular magnetism in triangular-lattice cluster materials*. PhD thesis, Johns Hopkins University, 2015.

[156] Theodore Shifrin. Differential geometry: a first course in curves and surfaces. *University of Georgia*, 2015.

[157] NA Sinitsyn, Qian Niu, and Allan H MacDonald. Coordinate shift in the semiclassical boltzmann equation and the anomalous hall effect. *Physical Review B*, 73(7):075318, 2006.

[158] Evgeny A Stepanov. Signatures of a charge ice state in the doped mott insulator nb _3 cl _8. *arXiv preprint arXiv:2405.19114*, 2024.

[159] Doru Sticlet, Frederic Piéchon, Jean-Noël Fuchs, Pavel Kalugin, and Pascal Simon. Geometrical engineering of a two-band chern insulator in two dimensions with arbitrary topological index. *Physical Review B*, 85(16):165456, 2012.

[160] Zhenyu Sun, Hui Zhou, Cuixiang Wang, Shiv Kumar, Daiyu Geng, Shaosheng Yue, Xin Han, Yuya Haraguchi, Kenya Shimada, Peng Cheng, et al. Observation of topological flat bands in the kagome semiconductor nb3cl8. *Nano Letters*, 22(11):4596–4602, 2022.

[161] Shintaro Takayoshi, Jianda Wu, and Takashi Oka. New aspects of nonadiabatic geometric effects–application to twisted schwinger effect in dirac and weyl fermions. *arXiv preprint arXiv:2005.01755*, 2020.

[162] Shintaro Takayoshi, Jianda Wu, and Takashi Oka. Nonadiabatic nonlinear optics and quantum geometry—application to the twisted schwinger effect. *SciPost Physics*, 11(4):075, 2021.

[163] Ibuki Terada, Sota Kitamura, Hiroshi Watanabe, and Hiroaki Ikeda. Multitunneling effect of nonreciprocal landau-zener tunneling: Insights from dc field responses. *Physical Review B*, 111(6):064315, 2025.

[164] David J Thouless, Mahito Kohmoto, M Peter Nightingale, and Marcel den Nijs. Quantized hall conductance in a two-dimensional periodic potential. *Physical Review Letters*, 49(6):405, 1982.

[165] DJ Thouless. Quantization of particle transport. *Physical Review B*, 27(10):6083, 1983.

[166] Mads L Trolle, Yao-Chung Tsao, Kjeld Pedersen, and Thomas G Pedersen. Observation of excitonic resonances in the second harmonic spectrum of $mos_2$. *Physical Review B*, 92(16):161409, 2015.

[167] Abolhassan Vaezi, Yufeng Liang, Darryl H Ngai, Li Yang, and Eun-Ah Kim. Topological edge states at a tilt boundary in gated multilayer graphene. *Physical Review X*, 3(2):021018, 2013.

[168] Nguyen Van Hinh and Pham Thi Thanh Nga. Magnetic properties of the spin-1 j 1- j 3 heisenberg model on a triangular lattice. In *Journal of Physics: Conference Series*, volume 2744, page 012003. IOP Publishing, 2024.

[169] Marc Vila, Jose H Garcia, and Stephan Roche. Valley-polarized quantum anomalous hall phase in bilayer graphene with layer-dependent proximity effects. *Physical Review B*, 104(16):L161113, 2021.

[170] Hua Wang and Kai Chang. Geodesic nature and quantization of shift vector. *arXiv preprint arXiv:2405.13355*, 2024.

[171] Xiao Wang, Xiaodong He, and Jianda Wu. Many-body quantum geometry in time-dependent quantum systems with emergent quantum field theory instantaneously. *arXiv preprint arXiv:2503.18396*, 2025.

[172] Gregory H Wannier. The structure of electronic excitation levels in insulating crystals. *Physical Review*, 52(3):191, 1937.

[173] Jian-da Wu, Mei-sheng Zhao, Jian-lan Chen, and Yong-de Zhang. Adiabatic condition and quantum geometric potential. *Physical Review A—Atomic, Molecular, and Optical Physics*, 77(6):062114, 2008.

[174] HJ Xiang, EJ Kan, Su-Huai Wei, M-H Whangbo, and XG Gong. Predicting the spin-lattice order of frustrated systems from first principles. *Physical Review B—Condensed Matter and Materials Physics*, 84(22):224429, 2011.

[175] Hongjun Xiang, Changhoon Lee, Hyun-Joo Koo, Xingao Gong, and Myung-Hwan Whangbo. Magnetic properties and energy-mapping analysis. *Dalton Transactions*, 42(4):823–853, 2013.

[176] Di Xiao, Ming-Che Chang, and Qian Niu. Berry phase effects on electronic properties. *Reviews of Modern Physics*, 82(3):1959, 2010.

[177] Di Xiao, Wang Yao, and Qian Niu. Valley-contrasting physics in graphene: magnetic moment and topological transport. *Physical Review Letters*, 99(23):236809, 2007.

[178] Jun Xiao, Mervin Zhao, Yuan Wang, and Xiang Zhang. Excitons in atomically thin 2d semiconductors and their applications. *Nanophotonics*, 6(6):1309–1328, 2017.

[179] Jia-Xin Xiong, Xiuwen Zhang, and Alex Zunger. Role of magnetic and structural symmetry breaking in forming the mott insulating gap in nb 3 cl 8. *Physical Review B*, 111(15):155122, 2025.

[180] Chao Xu, Jianda Wu, and Congjun Wu. Quantized interlevel character in quantum systems. *Physical Review A*, 97(3):032124, 2018.

[181] Xiaodong Xu, Wang Yao, Di Xiao, and Tony F Heinz. Spin and pseudospins in layered transition metal dichalcogenides. *Nature Physics*, 10(5):343–350, 2014.

[182] Yang Xu, Kaifei Kang, Kenji Watanabe, Takashi Taniguchi, Kin Fai Mak, and Jie Shan. A tunable bilayer hubbard model in twisted $wse_2$. *Nature Nanotechnology*, 17(9):934–939, 2022.

[183] Qiu Yang, Min Wu, Jingyi Duan, Zhijie Ma, Lingxiao Li, Zihao Huo, Zaizhe Zhang, Kenji Watanabe, Takashi Taniguchi, Xiaoxu Zhao, et al. Gate tunable room-temperature mott insulator in kagome compound nb3cl8. *arXiv preprint arXiv:2506.08730*, 2025.

[184] Xiulin Yang, Ying Zeng, Min Pan, Man Jiang, Chunfeng Hu, and Qingguo Feng. Electronic and optical properties of cri3/nb3cl8 heterojunction: a first principles investigation. *Journal of Physics: Condensed Matter*, 37(23):235501, 2025.

[185] Wang Yao, Shengyuan A Yang, and Qian Niu. Edge states in graphene: From gapped flat-band to gapless chiral modes. *Physical Review Letters*, 102(9):096801, 2009.

[186] Jiho Yoon, Edouard Lesne, Kornelia Sklarek, John Sheckelton, Chris Pasco, Stuart SP Parkin, Tyrel M McQueen, and Mazhar N Ali. Anomalous thickness-dependent electrical conductivity in van der waals layered transition metal halide, nb3cl8. *Journal of Physics: Condensed Matter*, 32(30):304004, 2020.

[187] Hongyi Yu, Xiaodong Cui, Xiaodong Xu, and Wang Yao. Valley excitons in two-dimensional semiconductors. *National Science Review*, 2(1):57–70, 2015.

[188] Peter Y Yu and Manuel Cardona. *Fundamentals of semiconductors: physics and materials properties*. Springer Science & Business Media, 2010.

[189] Sheng Yu, Junyu Tang, Yu Wang, Feixiang Xu, Xiaoguang Li, and Xinzhong Wang. Recent advances in two-dimensional ferromagnetism: strain-, doping-, structural-and electric field-engineering toward spintronic applications. *Science and technology of advanced materials*, 23(1):140–160, 2022.

[190] Bingyu Zhang, Pengcheng Lu, Roozbeh Tabrizian, Philip X-L Feng, and Yingying Wu. 2d magnetic heterostructures: Spintronics and quantum future. *npj Spintronics*, 2(1):6, 2024.

[191] Fan Zhang, Jeil Jung, Gregory A Fiete, Qian Niu, and Allan H MacDonald. Spontaneous quantum hall states in chirally stacked few-layer graphene systems. *Physical Review Letters*, 106(15):156801, 2011.

[192] Fan Zhang, Allan H MacDonald, and Eugene J Mele. Valley chern numbers and boundary modes in gapped bilayer graphene. *Proceedings of the National Academy of Sciences*, 110(26):10546–10551, 2013.

[193] Hongrun Zhang, Zhijian Shi, Zhicheng Jiang, Ming Yang, Jingwei Zhang, Ziyuan Meng, Tonghua Hu, Fucai Liu, Long Cheng, Yong Xie, et al. Topological flat bands in 2d breathing-kagome lattice nb3tecl7. *Advanced Materials*, 35(41):2301790, 2023.

[194] Shuqing Zhang, Runzhang Xu, Nannan Luo, and Xiaolong Zou. Two-dimensional magnetic materials: structures, properties and external controls. *Nanoscale*, 13(3):1398–1424, 2021.

[195] Xiaoou Zhang. *Topological Effects in Two-Dimensional Systems*. PhD thesis, Carnegie Mellon University, 2019.

[196] Xiaoou Zhang, Wen-Yu Shan, and Di Xiao. Optical selection rule of excitons in gapped chiral fermion systems. *Physical Review Letters*, 120(7):077401, 2018.

[197] Yi Zhang, Yuhao Gu, Hongming Weng, Kun Jiang, and Jiangping Hu. Mottness in two-dimensional van der waals nb 3 x 8 monolayers (x= cl, br, and i). *Physical Review B*, 107(3):035126, 2023.

[198] Mei-sheng Zhao, Jian-lan Chen, et al. Adiabatic condition and quantum geometric potential. *Physical Review A*, 77(6):062114, 2008.

[199] Jian Zhou, Qiang Sun, and Puru Jena. Valley-polarized quantum anomalous hall effect in ferrimagnetic honeycomb lattices. *Physical Review Letters*, 119(4):046403, 2017.

[200] Tong Zhou, Shuguang Cheng, Michael Schleenvoigt, Peter Schüffelgen, Hua Jiang, Zhongqin Yang, and Igor Žutić. Quantum spin-valley hall kink states: From concept to materials design. *Physical Review Letters*, 127(11):116402, 2021.

[201] YZ Zhou, X Han, J Luo, DT Wu, AF Fang, B Shen, BJ Feng, YG Shi, J Yang, and R Zhou. Antiferromagnetic spin fluctuations and structural transition in cluster mott insulator candidate nb3cl8 revealed by 93nb-and 35cl-nmr. *Chinese Physics Letters*, 2025.

[202] Igor Žutić, Jaroslav Fabian, and S Das Sarma. Spintronics: Fundamentals and applications. *Reviews of modern physics*, 76(2):323, 2004.